MEASURING SPATIO-TEMPORAL DISTORTIONS IN FEMTOSECOND LASERS

THE CHARACTERIZATION OF PULSE FRONT TILT AND SPATIAL DISPERSION IN 800 NM FEMTOSECOND LASERS

By

BENJAMIN A. L. DOYLE, B.Sc.

A Thesis
Submitted to the School of Graduate Studies
in Partial Fulfillment of the Requirements
for the Degree
Master of Science

McMaster University

MASTER OF SCIENCE (2005) McMaster University
(Physics) Hamilton, Ontario

TITLE: The characterization of pulse front tilt and spatial dispersion in 800 nm femtosecond lasers

AUTHOR: Benjamin A. L. Doyle, B.Sc. (University of Guelph)

SUPERVISOR: Dr. Harold K. Haugen

NUMBER OF PAGES: x, 166

Abstract

This thesis presents a study of diagnostics of pulsed laser systems. Two simple and cost effective devices are constructed that measure common spatio-temporal distortions. The first is a spectrally-resolved knife-edge (SRKE) for spatially and spectrally resolving a laser beam, which enables spatio-temporal distortions to be measured. The second is an interferometric autocorrelation taken with a 2-photon diode. A lens is used to focus light from the entire cross section of the beam onto the diode. By scanning the diode through the focus, the effects of pulse-front-tilt on focused beam pulse durations can be measured. These techniques are compared with current theoretical models, and with each other, to establish their reliability and practicality, as well as the reliability of the commercial techniques. SRKE is found to be highly sensitive to spatial and angular dispersion, and also able to measure the frequency gradient, although not as precisely. Interferometric autocorrelation is only able to resolve effects on duration. It can detect the presence of significant spatio-temporal distortion, but several scans must be taken as a function of distance from the lens, through the focus.

A commercially built GRENOUILLE was also tested on pulses compressed with a hollow-capillary-prism pulse compressor. Compression of 800 nm, 50 fs pulses to less than 19 fs was achieved with an overall transmission efficiency of 33%. With further work, efficiency could be increased, and pulse duration decreased.

Acknowledgements

I would like to take this opportunity to thank Dr. Harold Haugen for his attention to detail and his patience, some of which (I hope!) has rubbed off on me. Most of all I would like to thank him for his infectious enthusiasm. His personality drew me to McMaster, and I don't regret the decision.

I would also like to thank Dr. Henry Tiedje, Travis Crawford and Dr. Andrzej Borowiec. They have helped me with countless problems (small and not so small) over the last two years. They have always been willing to listen to my (sometimes crazy) ideas and helped to keep me sane.

I would like to thank Matt, Mom and Dad, who have always been ready to tell me how proud they are of me in my moments of doubt. I would like to thank Adria for her inexhaustible patience and love, for her unique perspectives and tireless optimism. I don't know what I'd do without her! Lastly I would like to thank all of my friends, who remind me that the world is more than numbers, and keep me honest. "It's been a long time getting here".

The past two years have certainly taught me to appreciate the truth to the statement I heard somewhere once. In theory: theory = practice. In practice: theory $\neq$ practice! The devil is, as always, in the details.

Table of Contents

List of Figures

Chapter 1

Introduction

1.1 The Ultrafast Laser Pulse

The term ultrafast laser has different meanings depending on where it is used. In this thesis ultrafast laser is used synonymously with femtosecond laser. In other words, a pulsed laser with a pulse duration of several femtoseconds. One femtosecond (fs) is 10^{-15} seconds. To paint an intuitive picture of how short this is, note that light travels just 300 nanometers each femtosecond, which is less than one wavelength for visible light. One femtosecond is as small compared to a single second as 5 minutes is to 10 billion years (the estimated age of the universe). Using chirped pulse amplification (CPA), high intensity ultrafast sources are now widely available. By operating at a low repetition rate, tabletop lasers can produce pulses with peak optical power of gigawatts, or on the order of the atomic field. For example, the peak power of these pulses can equal the total electrical power generated in all of Ontario.

Ultrafast high intensity laser pulses are of interest for many scientific applications such as atomic and molecular dynamics experiments. This is due to that fact that the dynamics of atomic and molecular systems often unfold on the time scale of a few femtoseconds. In order to exert the control required for these sophisticated experiments, the electric field of the laser

pulse must be measured. The usual assumption is that the temporal profile is the same at all points spatially, or that time is not coupled to the transverse spatial dimensions. Working under this assumption, a number of techniques have recently been developed to measure the electric field amplitude and phase as either a function of time or frequency, though their acceptance is not yet universal.

The assumption that the temporal profile of a femtosecond pulse is uniform spatially turns out to be false in many cases. Many optical systems, if not aligned perfectly, will induce spatio-temporal distortions, or couplings between spatial and temporal profiles. In fact the ubiquitous CPA system used to generate the pulses in the first place is a common culprit behind spatio-temporal distortions. These distortions will lead to sub-optimal laser performance, especially when the pulses are focused. The fact that these spatio-temporal distortions will have little or no effect on many measurements outside of the focus makes them easy to overlook.

Two common manifestations of spatio-temporal pulse distortion are pulse-front-tilt (PFT), and spatial dispersion (SD). Pulses exhibiting PFT have an intensity front that is not perpendicular to their propagation direction; pulses exhibiting SD have a non-spatially-uniform spectrum. Both of these phenomena arise as a result of common experimental conditions and are difficult to measure with standard diagnostic techniques. Techniques that abandon the assumption of a spatially uniform temporal pulse profile and tackle the full problem are a subject of current research.

1.2 Thesis Outline

Presented here is a summary of work completed at McMaster University between September 2003 and 2005, under the supervision of Dr. Harold K. Haugen. This thesis is divided into four main sections. Chapter 2 provides the

theoretical background for ultrafast lasers, and chapter 3 provides a background for experimental techniques and common pitfalls.

Work on this thesis began with setting up the pulse compression apparatus, and developing software for modeling pulse propagation, and for experimental data acquisition and analysis. Initial lack of much success with compression led to developing diagnostics, especially diagnostics for detecting spatio-temporal distortions. Work on diagnostics included the implementation of two custom devices, the interferometric autocorrelator, and the spectrally-resolved knife-edge. Two commercial techniques were also studied: the Swamp Optics GRENOUILLE and the Light Conversion TFPA. The diagnostic studies are outlined in chapter 4. With proper diagnostics in place, compression of 800 nm 50 fs laser pulses to less than 19 fs was successfully achieved. A summary can be found in chapter 5. Chapter 6 includes the final discussion of the results presented in this thesis, and outlook for work beyond this thesis.

Chapter 2

Theoretical Background

2.1 Optics Overview

A full theoretical description of the interaction of light and matter requires application of the theory of quantum electrodynamics (QED). In most practical cases however it is sufficient to use approximate theories, since the application of QED is labour intensive. An understanding of the various levels of approximation available, therefore, is a good starting point for any investigation of optical phenomena. This way, only the theoretical elements necessary to describe a phenomena of interest need be applied.

A common theoretical approximation of QED is classical electromagnetism. Light is modeled as a vector field obeying a vector wave equation derived from Maxwell's equations of electromagnetism. This theory can be augmented by results either derived from quantum mechanics or empirically measured, such as a material's polarizability.

Further approximations can be made when we demand less of our theory. For instance, if we pick a particular polarization of light and are only modeling materials that will maintain this polarization, we can use a scalar theory of electromagnetism. This level of theory is sufficient for most of the material in this thesis.

A further theoretical simplification that is often useful is that of ray

or geometric optics. When the wavelength of light is small compared to the geometry of its surroundings, it can be considered to travel in rays, drastically simplifying analysis.

A comprehensive review of optics and electromagnetism can be found in references [ST91], [Hec90], [Jac75] and [ME88]. Theory describing ultrafast laser pulses can be found in references [DR96] and [Agr89]. Material in this chapter is adapted largely from these sources, and presented here for convenience.

2.2 Ray Optics

Ray optics is the simplest physical theory of light. It is sufficient to assume light is transmitted by individual rays when we are not concerned with length scales on the order of the wavelength of light or smaller. Ray optics is an intuitive way to think about light. This is particularly true for laser light, which is usually highly collimated.

The ray picture of light contains three postulates. Firstly that light travels in rays. Secondly, that every transparent material can be characterized by its index of refraction n, which defines the speed of light in that material $v = c/n$. The third postulate is that light rays will travel between two points on a path that minimizes the transit time.

These three postulates are sufficient to derive simple laws of reflection and refraction, and can describe lenses and mirrors. This theory does not predict diffraction, interference or any polarization effects. It is powerful enough when used with matrix methods, to determine the stability of an oscillating optical cavity.

2.3 Wave Optics

Wave optics models light as consisting of waves. It is the next most simple theory of light and surprisingly rich and descriptive. Wave optics is a scalar approximation of the full classical electromagnetic theory and as such does not incorporate the polarization of light. It is therefore useful for light traveling in isotropic media where its polarization will be unimportant. Wave optics describes phenomena such as interference and diffraction.

The starting point for wave optics is the wave equation

$$\nabla^2 U(\boldsymbol{r},t) - \frac{1}{c^2}\frac{\partial^2 U(\boldsymbol{r},t)}{\partial t^2} = 0 \tag{2.1}$$

A given solution U to this equation will have a specific wavelength, and be called a monochromatic wave. This wave can be broken into components.

$$U(\boldsymbol{r},t) = a(\boldsymbol{r},t)\cos\left[2\pi f t + \phi(\boldsymbol{r})\right] \tag{2.2}$$

also,

$$f = \frac{\omega}{2\pi} = \frac{1}{\Gamma} = \frac{kc}{2\pi} = \frac{c}{\lambda} \tag{2.3}$$

where $\boldsymbol{r}$ is position, a is amplitude, ϕ is phase, f is linear frequency, ω is the angular frequency, Γ is the oscillation period, k is the wave number and λ is the wavelength of the wave.

There are many ways of expressing the same information contained in equation 2.2, for instance it can be constructed as complex with cos becoming exp, and the amplitude can become complex by absorbing the phase term, resulting in

$$U(\boldsymbol{r},t) = \tilde{a}(\boldsymbol{r})\exp(\omega t) \tag{2.4}$$

and

$$\tilde{a}(\boldsymbol{r}) = a(\boldsymbol{r}) \exp\left[\imath\phi(\boldsymbol{r})\right] \tag{2.5}$$

In this case equation 2.1 reduces to the Helmholtz equation, given by

$$\left(\nabla^2 + k^2\right) U(\boldsymbol{r}, \omega) = 0 \tag{2.6}$$

Any amplitude function $a(\boldsymbol{r})$ can be expanded into a series of plane waves or spherical waves, depending upon the situation. Equation 2.6 is a linear equation, so any linear combination of solutions to this equation will itself be a solution. This is described physically as the superposition principle. The result is that the field at a given point will be the simple arithmetic sum of the fields of all waves at that point.

Additionally, monochromatic waves of different frequencies can be superimposed to produce polychromatic light. This means that polychromatic light can be treated with this theory through the use of Fourier decomposition, which separates a polychromatic wave into its monochromatic components. The addition of multiple frequencies leads to beating effects and leads to a technique for the generation of ultrafast laser pulses known as mode-locking.

It must be noted that as the frequency of light is increased it becomes first impractical and then impossible to directly measure the electric field. The only information an experimentalist working at frequencies in the infrared or greater has direct access to is the intensity of a field, given by

$$I = < U^2(\boldsymbol{r}, t) > \tag{2.7}$$

and correspondingly

$$P = \int_A I(\boldsymbol{r}, t)\, d\boldsymbol{A} \tag{2.8}$$

where P and I are optical power and intensity respectively, and A the area integrated over. The"<>"symbol is meant to indicate some experimental time average.

Simple observations of intensity are insensitive to phase and integrate over a finite time scale. This is the reason sophisticated diagnostic techniques are required to measure the field of very short laser pulses, as discussed in later sections.

2.4 The Fourier Transform

Its frequent appearance in this work makes an understanding of functions of reciprocal variables and the Fourier transform essential, so it is reviewed here. Any function f of a given variable x can be transformed into a function of $X = x^{-1}$ using the relation

$$F(X) = \int f(x) \exp(\imath x X)\, dx \tag{2.9}$$

Likewise, functions of X can be transformed back using the relation

$$f(x) = \frac{1}{2\pi} \int F(X) \exp(-\imath x X)\, dX \tag{2.10}$$

There are many important reasons to transform a function of a variable into a function of its conjugate variable. If for instance, that variable is time and the function is the electric field, the reciprocal variable will be frequency and the transformed function will be the frequency spectrum. Often dynamics involving the function will be vastly simpler in the transformed domain.

Often functions of interest will have a limited range inside which it will have non-zero value, and beyond which its value falls below some threshold of interest, or becomes smaller than experimental noise. It is useful to define

a measure of their width that does not depend on their analytic form. Full-width-at-half-maximum (FWHM) is defined as the width of the function when it has decreased to half its maximal value. Complicated signals may have an ambiguous FWHM.

The most frequent use of Fourier arguments made in this thesis are in the context of laser pulses. This will usually mean that the direct variable x is time, and the reciprocal variable X is frequency. The time-space function is then called the temporal amplitude and the frequency space function is called the spectral amplitude. The measurable quantities in these domains are the temporal and spectral intensities, which are the temporal and spectral amplitudes squared. It is also possible to talk about Fourier transforms with respect to the spatial dimensions, which result in spatial frequencies.

A time-bandwidth product (TBP) can be defined for suitably behaved functions of time. It is the product of the time space FWHM and the frequency space FWHM. Temporal functions with a constant phase will have the minimum TBP for that family of functions. This minimum TBP is given by

$$\Delta\omega T_0 = 2\pi\Delta f T_0 \geq 2\pi c_B \tag{2.11}$$

where $\Delta\omega$ is the FWHM of the spectral intensity, T_0 is the FWHM of the temporal intensity, and c_B is a constant. Minimum TBP's are given in table 2.1 [DR96].

For transform limited Gaussian pulses, intensity FWHM bandwidth and duration are related by

$$\Delta\lambda T_0 = \frac{2\ln 2}{\pi}\frac{\lambda^2}{c} \tag{2.12}$$

The product on the left hand side is equal to 941 fs·nm for 800 nm light.

It is also possible to define a TBP for a real laser pulse. In this case the

Function	Temporal Intensity	T_0	Spectral Intensity	$\Delta\omega$	c_B
Gaussin	$\exp\left(-2\frac{T^2}{T_G^2}\right)$	$1.177T_G$	$e^{-(\omega T_G)^2/2}$	$2.355/T_G$	0.441
sech^2	$\text{sech}^2\left(\frac{T}{T_S}\right)$	$1.763T_S$	$\text{sech}^2\left(\frac{\pi\omega T_S}{2}\right)$	$1.122/T_S$	0.315
Lorentz	$\left[1+\left(\frac{T}{T_L}\right)^2\right]^{-2}$	$1.287T_L$	$e^{-2\lvert\omega\rvert T_L^2}$	$0.693/T_L$	0.142
rectang.	1 if $\lvert T/T_R\rvert \leq 1$	T_R	$\text{sinc}^2(\omega T_R)$	$2.78/T_R$	0.443

Table 2.1: Important statistics for common functions and their Fourier transforms. T parameterizes time, ω parameterizes frequency. The subscripts G, S, L and R refer to characteristic values for Gaussian, hyperbolic secant squared, Lorentzian and rectangular functions, respectively. T_0 and $\Delta\omega$ are FWHM temporal and frequency widths respectively.

complex envelope of the pulse will not in general have constant phase. As the phase of the pulse becomes more nearly constant, its TBP will decrease. Pulses with more complicated spectral intensities will in general have larger TBP's. The limit on TBP means that there is a minimum pulse duration for a given spectral FWHM. When the pulse has reached this duration it is Fourier transform limited. The temporal amplitude of laser pulses will usually be modeled as a Gaussian, though other functional forms can be used. Real pulses will not in general have an analytic form.

2.5 Beam Optics

Plane waves and spherical waves are two extreme cases of spatial profile solutions to the wave equation. Near their origin, spherical waves have maximal localization, but also total divergence into all angles. Plane waves on the other hand have no divergence, but cannot be localized. Zero divergence and high localization cannot be simultaneously realized, but one can reach a compromise.

Light beams can be formed that localize the intensity of a light source to an extent, while maintaining a small, but non-zero divergence. Consider a surface S enclosing a fixed fraction of the total beam power. One can define the divergence angle ψ of the beam as the angle that the centre of the beam makes with S sufficiently far from the beam source. The width in a given dimension of the beam at its minimal value is denoted w_0. The location where this minimum occurs is called the waist. In general, the product of the divergence of a beam and its width will be proportional to the beam's wavelength λ. This means that in general, shorter wavelengths can be focused into a smaller area without changing their divergence.

The optimal tradeoff between divergence and localization are beams with a Gaussian transverse spatial profile. These beams have a divergence-width-product equal to [Sel83]

$$w_{0G}\psi_G = \frac{\lambda}{\pi} \tag{2.13}$$

where w_{0G} is the radius at which the intensity drops by a factor of $1/e^2$ at the waist and ψ_G is the divergence angle from the centre of the Gaussian beam to the $1/e^2$ radius. One can define the Rayleigh range of the beam as the longitudinal distance over which the radius of the beam increases by a factor of $\sqrt{2}$

$$z_{RG} = \frac{\pi w_{0G}^2}{\lambda} \tag{2.14}$$

The width and the radius of curvature of a Gaussian beam are given by

$$w(z) = w_{0G}\left[1 + \left(\frac{z}{z_{RG}}\right)^2\right]^{1/2} \tag{2.15}$$

$$R(z) = z\left[1 + \left(\frac{z_{RG}}{z}\right)^2\right] \tag{2.16}$$

where z is the distance from the beam waist. Equations 2.15 and 2.16 are solutions to the paraxial Helmholtz equation.

To understand the influence focussing optics have on Gaussian beams, it is necessary to extend the classical thin lens equation of geometric or ray optics to Gaussian beams, as is done by Self [Sel83]. The thin lens equation can be manipulated to yield the magnification of a lens

$$m = \frac{w'_{0G}}{w_{0G}} = f\left[(f-s)^2 + z_{RG}^2\right]^{-1/2} \tag{2.17}$$

where f is the focal length of the optic, s is the distance from the lens to the waist of the input beam, w_{0G} is the $1/e^2$ intensity width of the incident beam and w'_{0G} is the $1/e^2$ intensity width of the output beam. If the Rayleigh range is large compared to the difference between the focal length of the lens and the position of the input waist ($z_{RG} \gg f - s$), equation 2.17 reduces to

$$w'_{0G} = \frac{f\lambda}{\pi w_{0G}} \tag{2.18}$$

Ideal lasers are usually modeled as producing a Gaussian spatial profile, making it important to understand the behaviour of Gaussian beams. To model real lasers it is necessary to consider deviations from the above analysis. The following is a summary of Haiyin Sun's results for real beams and thin lenses [Sun98]. A non-ideal laser will have a non-Gaussian spatial profile, which will lead to a divergence-width-product different than equation 2.13. These real beams are modeled by assuming a numerical constant M^2 modifier to their divergence-width-product

$$w_0\psi = M^2\frac{\lambda}{\pi} \tag{2.19}$$

where w_0 and ψ are the real beam width and divergence respectively. Equations 2.14 through 2.17 must be rewritten as

$$z_R = \frac{\pi w_0^2}{\lambda} \tag{2.20}$$

$$w(z) = w_0 \left[1 + \left(\frac{M^2 z}{z_R}\right)^2\right]^{1/2} \tag{2.21}$$

$$R(z) = z\left[1 + \left(\frac{z_R}{M^2 z}\right)^2\right] \tag{2.22}$$

$$m = \frac{w_0'}{w_0} = f\left[(f-s)^2 + \left(\frac{z_R}{M^2}\right)^2\right]^{-1/2} \tag{2.23}$$

$$w_0' = M^2 \frac{f\lambda}{\pi w_0} \tag{2.24}$$

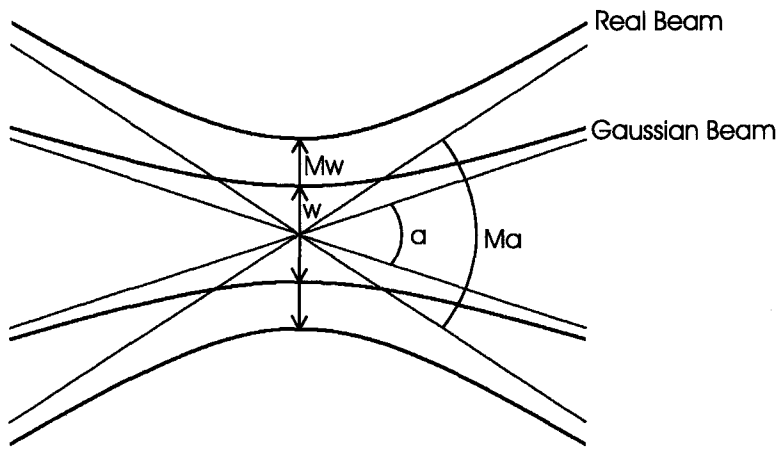

Figure 2.1: Gaussian beam (waist radius w and divergence angle a) and real laser beam (waist radius Mw and divergence angle Ma).

Figure 2.1 compares a real beam with its imbedded Gaussian beam. The divergence angle of the real beam is M times greater than the imbedded Gaussian beam, as is its waist radius.

2.6 Electromagnetic Optics

From electromagnetism comes Maxwell's equations which are used to derive the wave equation solved in the previous section. When the vector nature of this equation is retained however, the polarization of light must enter our model. This allows us to consider a dielectric medium for which we can define a polarization vector.

The vector wave equation reads

$$\left(\nabla - \frac{1}{c^2}\frac{\partial^2}{\partial t^2}\right)\boldsymbol{E}(\boldsymbol{r},t) = \mu_0 \frac{\partial^2}{\partial t^2}\boldsymbol{P}(\boldsymbol{r},t) \tag{2.25}$$

where $\boldsymbol{P}$ is the polarization and μ_0 is the permeability of free space. The solutions to the vector equation are still either spherical or plane waves (or hybrids, like beams).

Electromagnetic optics is necessary when polarization is a factor in a system, and cannot be separately treated. This is the case for waveguides and at dielectric boundaries, or in a tight focus (for example, see [DQL03]).

In order for equation 2.25 to be useful, we must have an expression for $\boldsymbol{P}$ as a function of $\boldsymbol{E}$, and this is where our theory requires either quantum mechanical or empirical results. It is the introduction of the polarizability tensor that allows for the theoretical description of all manner of subtle physical phenomena.

$\boldsymbol{P}$ is typically expanded in powers of $\boldsymbol{E}$,

$$P_i = \varepsilon_0\left[\chi^{(1)}_{ij}E_j + \chi^{(2)}_{ijk}E_jE_k + \chi^{(3)}_{ijkl}E_jE_kE_l + ...\right] \tag{2.26}$$

where ε_0 is the permittivity of free space, $\chi^{(n)}$ is a $(n+1)\,th$ rank tensor and the Einstein summation convention is used.

For everyday light, and even for laser light in most situations, it is sufficient to neglect all but the linear term $\chi^{(1)}$ in equation 2.26. To understand

the intense optical fields generated by pulsed lasers however, one needs to consider more terms in the expansion. For instance, the inclusion of $\chi^{(2)}$ is sufficient to describe second order nonlinear phenomena (second order in the electric field amplitude). These phenomena couple three waves and include effects such as frequency doubling and optical parametric interaction. The third order nonlinear term $\chi^{(3)}$, describes four wave mixing processes, such as self phase modulation (SPM).

Even order nonlinear terms will be zero for media with an inversion symmetry, except at their boundaries. This means that in order to exploit or investigate second order nonlinear effects, crystals or other material with internal anisotropy must be used. This also means that for isotropic materials that have an inversion symmetry, the lowest order nonlinearity will be third order.

2.7 Pulsed Laser Solutions

An approximate solution to the electromagnetic wave equation employs the separation of variables

$$\boldsymbol{E}(\boldsymbol{r},t) = \hat{x}\frac{1}{2}\left\{F(x,y)A(z,t)\exp\left[\imath\left(\beta_0 z - \omega_0 t\right)\right] + c.c.\right\} \tag{2.27}$$

where F is the transverse spatial profile, A is the slowly varying pulse envelope, ω_0 is the carrier frequency, z is the axis parallel to beam propagation, x and y are axes perpendicular to beam propagation axis and *c.c.* stands for the complex conjugate. The zeroth propagation constant β_0 is derived from the expansion of the propagation constant [Agr89]

$$\beta(\omega) = n(\omega)\frac{\omega}{c} = \beta_0 + \beta_1(\omega - \omega_0) + \frac{1}{2}\beta_2(\omega - \omega_0)^2 + \ldots \tag{2.28}$$

Similarly,

$$\beta_1 = \frac{1}{c}\left(n + \omega\frac{dn}{d\omega}\right) = \frac{1}{v_g} \tag{2.29}$$

$$\beta_2 = \frac{1}{c}\left(2\frac{dn}{d\omega} + \omega\frac{d^2n}{d\omega^2}\right) \simeq \frac{\omega}{c}\frac{d^2n}{d\omega^2} = \frac{\lambda^3}{2\pi c^2}\frac{d^2n}{d\lambda^2} \tag{2.30}$$

where v_g is the group velocity [Agr89].

This solution is based on the slowly varying envelope approximation, which allows the envelope function $A(z,t)$ to be separated from the carrier wave at frequency ω_0. This approximation is valid for $\Delta\omega \ll \omega_0$, or for pulses longer than a few tens of femtoseconds. If this simplifying approximation is not employed, the only way to proceed theoretically is to numerically integrate Maxwell's equations directly. This solution also assumes a fixed polarization and carrier wave frequency. If the spatial profile of the beam is treated separately, the only piece of the solution to worry about is the complex envelope function $A(z,t)$. Substituting equation 2.27 back into the wave equation, it is possible to derive a nonlinear partial differential equation that governs the dynamics of the pulse envelope as it proceeds through media. It is called the nonlinear propagation equation and is given by

$$\frac{\partial A}{\partial z} + \frac{\alpha}{2}A + \frac{\imath}{2}\beta_2\frac{\partial^2 A}{\partial T^2} - \frac{1}{6}\beta_3\frac{\partial^3 A}{\partial T^3} = \imath\rho\left[|A|^2A + \frac{\imath}{\omega_0}\frac{\partial}{\partial T}\left(|A|^2A\right) - T_R A\frac{\partial|A|^2}{\partial T}\right] \tag{2.31}$$

where

$$\rho = \frac{n_2\omega_0}{cA_{eff}} = \frac{2\pi n_2}{\lambda_0 A_{eff}} \tag{2.32}$$

$T = t - z/v_g = t - \beta_1 z$, α is the absorption coefficient, β_2 is the second order propagation constant, β_3 is the third order propagation constant, ρ is the nonlinear coefficient, n_2 is the nonlinear index of refraction, A_{eff} is the

effective area of the beam and T_R is the Raman response time of the medium. A derivation of equation 2.31 can be found in [Agr89].

It is important to remember that this equation is meant to be applied to isotropic media (optical fibers, specifically). This means that the second order polarizability will be zero. This equation therefore only includes third order nonlinearity.

The propagation equation can be transformed into a dimensionless form by making the substitutions $A = \sqrt{P_0}u$, and $T = T_G\tau$, where P_0 is the initial power and T_0 is the initial pulse width (for a Gaussian pulse, $T_0 = 2\sqrt{\ln 2}T_G$). The result is

$$\frac{\partial u}{\partial z} + \frac{1}{L_L}u + \frac{\imath}{2L_D}\frac{\partial^2 u}{\partial \tau^2} - \frac{1}{6L'_D}\frac{\partial^3 u}{\partial \tau^3} = \frac{\imath}{L_{NL}}\left[|u|^2 u + \imath C_S \frac{\partial\left(|u|^2 u\right)}{\partial \tau} + C_R u \frac{\partial |u|^2}{\partial \tau}\right] \quad (2.33)$$

The characteristic lengths L_L, L_D, L'_D, L_{NL} are the lengths over which loss, group delay dispersion, cubic dispersion, and nonlinear effects take place. The constants C_S and C_R are the self steepening and Raman delay factors. They are given by

$$L_L = \frac{2}{\alpha} \quad (2.34)$$

$$L_D = \frac{T_G^2}{\beta_2} \quad (2.35)$$

$$L'_D = \frac{T_G^3}{\beta_3} \quad (2.36)$$

$$L_{NL} = \frac{1}{P_0 \rho} \quad (2.37)$$

$$C_S = \frac{1}{\omega_0 T_G} \tag{2.38}$$

$$C_R = \frac{\tau_R}{T_G} \tag{2.39}$$

2.8 Dispersion

Group delay dispersion (GDD) can be defined as the second derivative of the spectral phase Φ with respect to frequency ω. It will also be equal to the second order term in the propagation vector β with respect to frequency, multiplied by propagation distance.

$$GDD = \Phi_2 = \frac{d^2\Phi}{d\omega^2} = \beta_2 z = \frac{d^2\beta}{d\omega^2} z \tag{2.40}$$

GDD occurs whenever the phase of a pulse or its propagation constant is made to vary as a function of frequency. The most familiar example of GDD is the propagation of a pulse through a dispersive slab. The index of refraction of any material will be dependent on the frequency of light passing through it. This also means that the velocity of different frequencies will be different. Upon propagation, there will be a delay between given frequencies or a GDD in a polychromatic light source. This is due to group velocity dispersion (GVD).

The leading edge of the pulse with positive GDD will be lower frequency, or more red, than the tailing edge of the pulse. GDD will also lead to a broadening of the pulse, as the spectral components disperse in time.

If an initially transform limited pulse is transmitted through a region inducing GDD, its resulting pulse duration will be given by

$$\frac{T_0'}{T_0} = \sqrt{1 + \left(\frac{4 \ln 2 \beta_2 z}{T_0^2}\right)^2} \tag{2.41}$$

This pulse can be returned to its original duration by propagating the pulse through a region inducing the opposite sign of GDD.

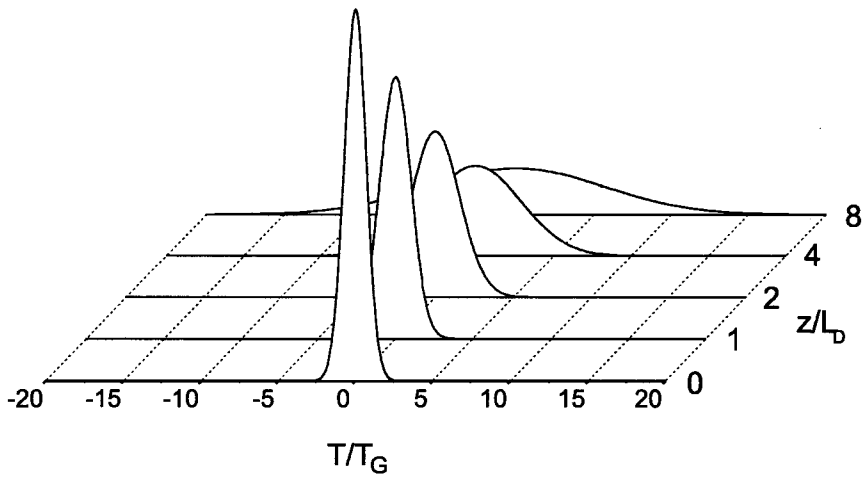

Figure 2.2: Initially transform limited laser pulse traveling through region of group delay dispersion.

Figure 2.2 shows the evolution of an initially un-dispersed pulse through a region with constant GDD. The product $\Phi_2 = \beta_2 z$ can be thought of as a measure of the induced GDD, and is called the second order phase shift. The effect of different values of Φ_2 on different initial, un-dispersed pulse durations is sketched in figure 2.3. Second order phase shift Φ_2 is the preferred experimental quantification of GDD, and is usually given in units of fs^2.

Chromatic dispersion is occasionally parameterized by "chirp factor" C. A "chirped" pulse is described by the equation [Agr89]

$$u(0,T) = \exp\left(-\frac{1 + \imath C}{2}\frac{T^2}{T_G^2}\right) \tag{2.42}$$

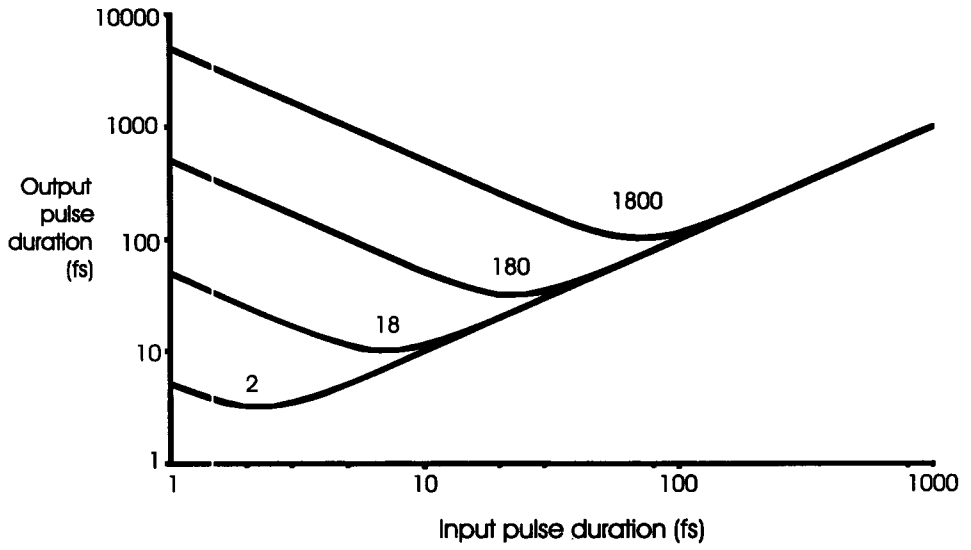

Figure 2.3: The effect of dispersion on the pulse length of an initially transform limited pulse. Different curves represent different values of second order phase shift Φ_2 (fs^2).

Chirp in this sense refers to a second order temporal phase shift. Higher order dispersion will result in an asymmetric spectrum and temporal pulse shape. The characteristic length over which cubic dispersion takes place is given by

$$L'_D = \frac{T_G^3}{|\beta_3|} \tag{2.43}$$

Figure 2.4 shows the evolution of an initially transform limited pulse through a region with constant cubic dispersion. Higher order dispersion is more difficult to remove from a laser pulse. For instance, to remove dispersion to third order, two dispersive elements, each with a different ratio between their second and third order dispersion are required.

A systematic summary of dispersion in ultrafast optical systems can be found in [WWD01]. An interferometric device for the accurate measurement of temporal dispersion in ultrafast optics is discussed in [KOK+05].

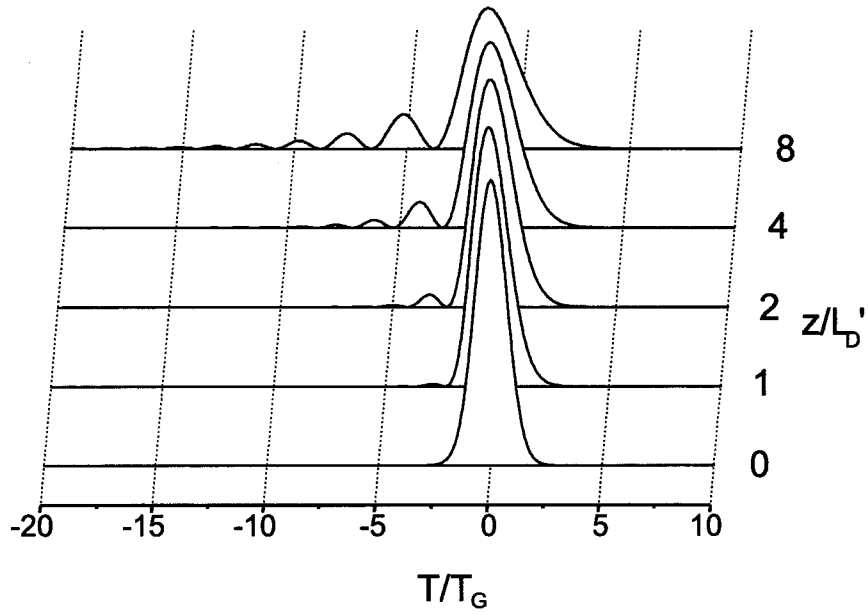

Figure 2.4: The effect of cubic dispersion on an initially transform limited pulse.

2.9 Nonlinear Interactions

2.9.1 Frequency Doubling

A particularly useful second order nonlinear process is frequency doubling. The strength of this process is proportional to the second order polarizability of a material, and it will generate light at twice the frequency of incident light. This process is essentially mixing three waves; two photons from the incident light are used to create one induced photon with twice the energy. These waves must all combine in phase, or they will cancel each other through destructive interference. The intensity of the frequency doubled light is proportional to the degree to which the incident and induced waves can be phase matched, and is given by [Tre00]

$$I(L,t) = \frac{c\mu_0\omega_0^2}{4}|\boldsymbol{P}|^2 L^2 sinc^2(\Delta kL/2) \tag{2.44}$$

where $\boldsymbol{P}$ is the polarization, L is the thickness of the nonlinear material and Δk is the difference in wavenumber between the incident light and the induced polarization. Equation 2.44 assumes a collimated input beam. For collinear generation, equation 2.44 can be maximized by ensuring $n(\omega) = n(2\omega)$. This can usually be accomplished by selecting the correct angle of incidence on the nonlinear crystal.

The above discussion describes phase matching for a single frequency. It is not possible to perfectly phase match more than one frequency at a time. A continuum of frequencies can be approximately phase matched however. Since ultrafast laser pulses have an appreciable bandwidth, it is important to consider the bandwidth of crystals used to frequency double them. The phase matching bandwidth is given by [Tre00]

$$\delta\lambda_{FWHM} = \frac{0.44\lambda_0/L}{|n'(\lambda_0) - \frac{1}{2}n'(\lambda_0/2)|} \tag{2.45}$$

where $n' = \frac{dn}{d\lambda}$

Equation 2.45 implies that as an ultrashort pulse becomes shorter, since its bandwidth increases, the thickness of any nonlinear crystal used to frequency double it must decrease. Crystals with less phase matching bandwidth than pulses they are being used to frequency double will act as a frequency filter. If the crystal is being used in autocorrelation, this will lead to an incorrect trace. The incorrect trace will often be shorter than a trace taken with a sufficiently thin crystal. This type of problem will become apparent if the crystal is being used in FROG, as the frequency marginal (the sum of a frog trace with respect to delay, see section 3.7 for more on FROG) will not match the expected second harmonic spectrum. How fast problems arise will depend on details of the pulse being studied, but will be especially

problematic for complex pulses [Tre00].

Equation 2.44 states that the intensity of the generated light is proportional to the length of the crystal squared. Since a crystal that is too thick will not properly frequency double the full bandwidth of an ultrafast pulse, and since a crystal that is too thin will result in very small induced signal, it is important to select a nonlinear crystal with a thickness appropriate to the application.

2.9.2 Self Phase Modulation

One of the standard ways to broaden the frequency spectrum of a laser pulse external to the laser cavity is through self phase modulation (SPM). This is a third order, four photon effect. The origin of this effect is the nonlinear index of refraction of the optical medium.

Ignoring all terms in equation 2.33 except the first nonlinear term, we are left with [Agr89]

$$\frac{\partial u}{\partial z} = \frac{\imath}{L_{NL}}|u|^2 u \tag{2.46}$$

with the solution

$$u(z,\tau) = u(0,\tau)\exp\left[\imath\phi_{NL}(z,\tau)\right] \tag{2.47}$$

where

$$\phi_{NL}(z,\tau) = |u(0,\tau)|^2\frac{z}{L_{NL}} \tag{2.48}$$

and

$$\phi_{max} = \frac{z}{L_{NL}} \tag{2.49}$$

Equation 2.48 is an intensity dependent phase shift. This results in a

frequency shift across the pulse given by

$$\delta\omega(\tau) = -\frac{\partial\phi_{NL}}{\partial\tau} = -\frac{\partial}{\partial\tau}\left(|u(0,\tau)|^2\right)\frac{z}{L_{NL}} \tag{2.50}$$

When the temporal profile is assumed to be Gaussian in shape, this results in a frequency shift across the pulse $\delta\omega$ given by

$$\delta\omega(\tau) = \frac{2}{T_0 L_{NL}}\tau z \exp\left(-\tau^2\right) \tag{2.51}$$

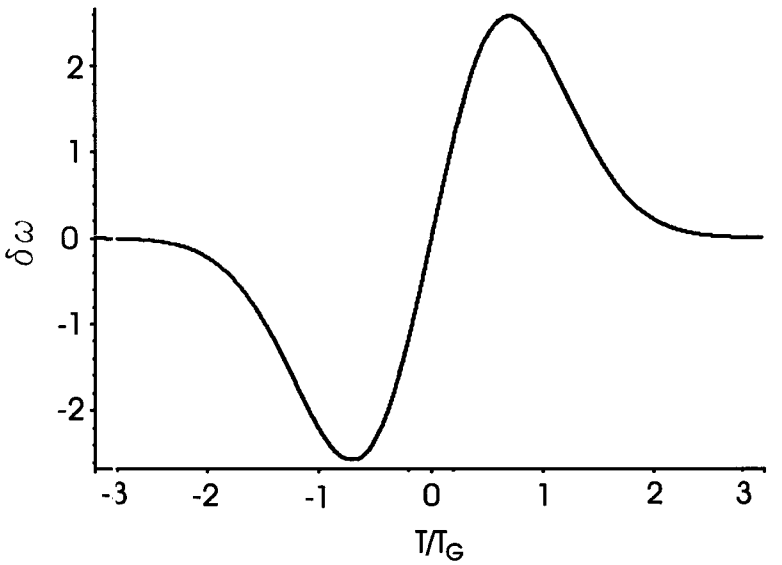

Figure 2.5: The frequency shift of a normalized Gaussian pulse undergoing SPM. Note that near the centre of this plot (where most of the pulse energy is located), the frequency shift is approximately linear. Note $\tau = T/T_G$.

This SPM leads to the creation of smaller frequencies (more red) at the leading edge of the pulse, and larger frequencies (more blue) at the trailing edge of the pulse. In addition, the frequency dispersion is almost linear in the center of the pulse, where most of the energy is concentrated (see figure 2.5). The spectral broadening factor for an initially transform limited Gaussian pulse is given by [Agr89]

$$\frac{\delta\omega_{max}}{\Delta\omega} = 0.86\phi_{max} \tag{2.52}$$

Figures 2.6 and 2.7 show the effects a pulse undergoing SPM. Notice that the presence of GDD affects the development of the pulse spectra. In the case of positive temporal dispersion the spectral width of the pulse can even be reduced [OH93].

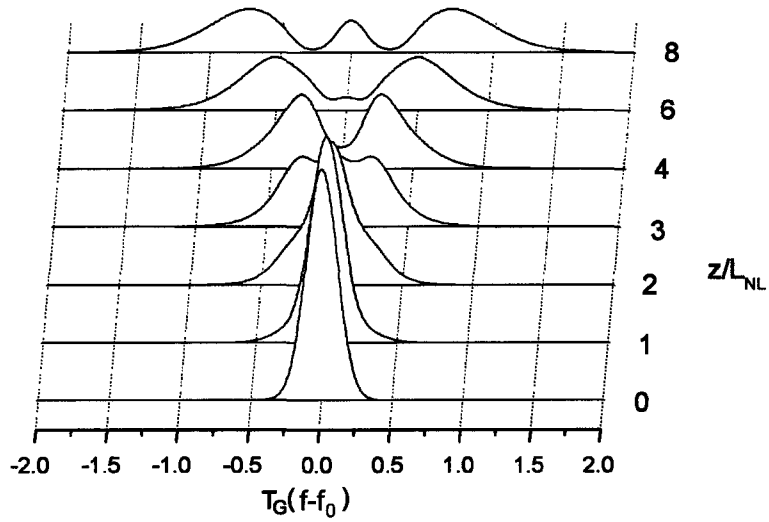

Figure 2.6: Transform limited laser pulse undergoing SPM.

A specific case of nonlinear phase shift worthy of further consideration is that of a beam traversing a window into a chamber, or through some other optical glass in an experiment. As an estimate of the magnitude of the nonlinear effect of a window placed near the focus of an intense ultrafast beam, one can consider the B integral

$$B = \frac{2\pi}{\lambda}\int n_2 I dL \sim \frac{2\pi}{\lambda} n_2 I L \tag{2.53}$$

which is just an integral over the length of interaction between the nonlinear index of refraction of the window and the intensity of the laser, where n_2

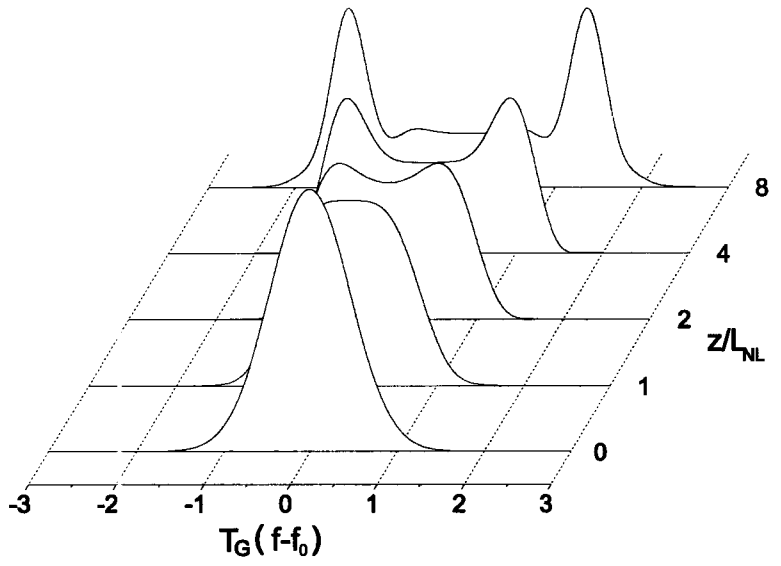

Figure 2.7: Negative GDD laser pulse undergoing SPM.

is the nonlinear refractive index, L is the thickness of the window, and I is the peak intensity of the beam. Good beam quality is maintained as long as $B < 1$. I is given by the equation

$$I = \frac{2E}{\pi w_0^2 T_0} \tag{2.54}$$

where E is the pulse energy, w_0 is the spot size and T_0 is the pulse duration.

As an example, consider the situation described in chapter 5. For fused silica glass, $n_2 = 3 \times 10^{-20}$ m^2/W [Agr89]. The typical output energy of the Spitfire is 500 μJ. A BK7 glass window is placed about 20 cm from the focus of an $f = 75$ cm lens. The beam has an initial width w_i of about 3 mm, leading to a spot size w at the window approximated by $w = w_i(1 - z/f) = 0.08$ cm. This leads to an intensity of 10^{12} W/cm^2. When these numbers are entered into equation 2.53, the result is $B = 1.24$, which is high enough to induce nonlinear effects. A typical experimental pulse energy in chapter 5 of 150 μW leads to B values closer to 0.4, however.

2.9.3 Multi Photon Ionization and Self Focussing

When focussing high intensity laser pulses into a hollow fiber capillary containing pressurized noble gas, important effects to consider are self-focussing, multi-photon ionization (MPI), and the onset of higher order nonlinearities. All of these effects will reduce the temporal quality of the resultant beam, making it more difficult to compress.

Perry et al. define the "threshold" for MPI theoretically as the point at which ionization probability rises above 10^{-4} [PLC88]. This is in good agreement with their experimental results. They determine the threshold for argon is $\sim 4 \times 10^{13}$ W/cm^2 and $\sim 2 \times 10^{13}$ W/cm^2 for krypton [PLC88]. It is because of these high thresholds that these gasses are often chosen for providing the nonlinear interaction in post cavity compression schemes, despite their modest nonlinear indices [Ole99]. The MPI threshold for these gasses will be higher for ultrafast pulses than for the 100 ps pulses used by Perry et al., since neutral atoms have less time to respond and will experience higher laser intensities before ionizing [ZPM+96]. MPI is clearly undesirable, as it will modify the state of the gas, creating a plasma.

Self focussing is an interesting spatio-temporal phenomena arising from the nonlinear refractive index. Since light near the centre of the pulse is more intense than at the edges, it will respond to a different refractive index, which will have the effect of focussing the pulse. Since both the natural diffraction of the pulse and the self focussing parameter are inversely proportional to the beam diameter, the threshold for self-focussing is given in terms of laser beam power, not intensity. This threshold power p_T is given by a complicated expression, derived numerically [LMNW94]

$$g = \frac{z_R}{2L_D} = \frac{\left[\sqrt{3.38 + 5.2\left(p_T^2 - 1\right)^2} - 1.84\right]\left[\left(\sqrt{p_T} - 0.852\right)^2 - 0.0219\right]}{2p_T} \tag{2.55}$$

where z_R is the Rayleigh range, L_D is the characteristic dispersive length define in section 2.8, $p = P/P_{CR}$, and P_{CR} is the critical power (which is the threshold power for self-focussing in a non-dispersive medium) given by

$$P_{CR} = 0.0479\frac{\pi\lambda_0^2}{n_0 n_2} \tag{2.56}$$

Powers above p_T will lead to self focussing.

Take for example the capillary used in section 5.2. The second order propagation constant β_2 is $\sim 12 \times p_a$ fs^2/m where p_a is pressure in bar [PF64]. For 50 fs FWHM pulses, and 1 bar of pressure, this leads to a characteristic dispersive length of about 75 m. The Rayleigh range for a 75 cm lens with a 3 mm radius input beam is 16 cm, which makes $g = 0.001$. The threshold power is approximately equal to the critical power. The index of refraction for argon is approximately 1.0 and the nonlinear index of refraction is 1×10^{-23} m^2/W [LLP85, NSS96], which makes the threshold power P_T for self focussing about 10^{10} W. Processes of higher order in intensity, such as continuum generation, will also cause problems, but their onset will be at higher intensities than MPI or self-focussing. [CRSR86].

2.9.4 Other Nonlinearities

Self steepening arises for very short pulses propagating through nonlinear media. Pulses undergoing self steepening have an intensity dependent group velocity, which results in a shift of the peak of the pulse with respect to its wings. This effect is depicted in figure 2.8. This effect will also lead to an asymmetrical spectrum [Agr89].

The last effect considered is that resulting from the Raman delay term. When the response time of the nonlinear medium is large compared with the pulse duration, the resulting spectral broadening will become slightly asymmetrical as a result of the Raman delay term [Agr89]. This effect is

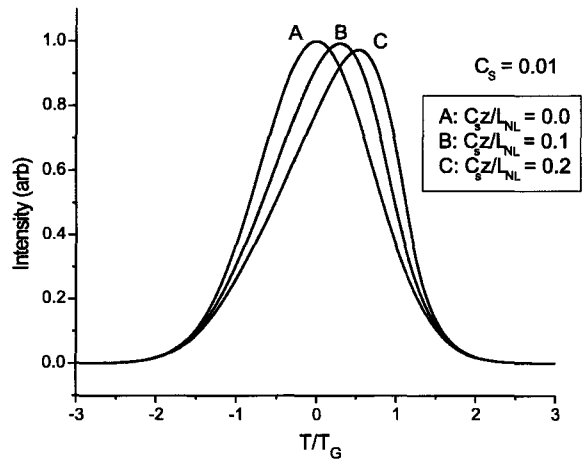

Figure 2.8: The effects of self steepening on an initially transform limited pulse.

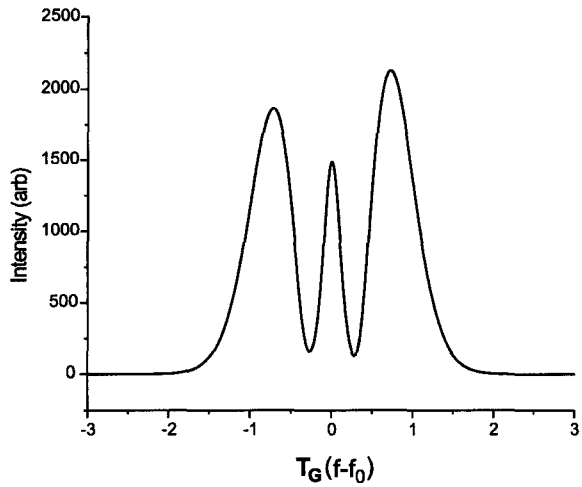

Figure 2.9: The effect of Raman delay on the spectrum of an initially transform limited pulse.

depicted in figure 2.9.

2.10 Spatio-Temporal Distortions

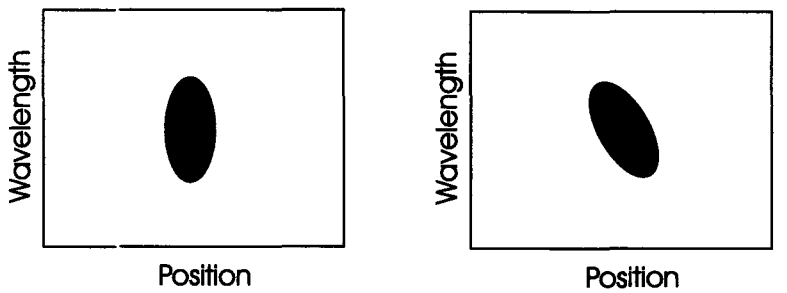

Figure 2.10: Spatial chirp on an imaging spectrometer. Left: pulse without spatial chirp. Right: pulse with spatial chirp. Nonuniform spectra as a function of position is called "shear".

The frequency spectrum of a pulsed laser beam can be made to vary as a function of a transverse coordinate. In other words, the left side of the pulse might for instance be more blue than the right side of the pulse. This effect is sometimes called "spatial chirp", though this term is somewhat ambiguous.

Spatial chirp can be visualized in the following way. If a beam with a Gaussian wavelength distribution and beam profile is measured with an imaging spectrometer so that its spectrum is resolved in the transverse direction, the resulting image will be a two dimensional Gaussian function. If spatial chirp is present in this same beam, the image will pick up a shift in one axis as a function of the other. This shift is called shear and an example is depicted in figure 2.10. As Gu et al. point out [GAT04], there is more than one way to measure this result. One can define the point of maximum spectral intensity for each transverse position $\omega_0(x)$, or define the point of maximum spectral intensity for each wavelength $x_0(\omega)$. Gu et al. suggests that spatial dispersion then be defined as [GAT04]

$$\zeta = \frac{dx_0}{d\omega} \tag{2.57}$$

and frequency gradient be defined as

$$\nu = \frac{d\omega_0}{dx} \tag{2.58}$$

and develops their relationship

$$\nu = \frac{\zeta}{\zeta^2 + (\Delta x/\Delta\omega)^2} \tag{2.59}$$

which it should be noted is not a simple reciprocal.

Spatial dispersion can arise due to angular dispersion introduced deliberately, or due to misalignment of prisms or gratings. In fact, very small misalignments of gratings in typical compressor setups will cause significant quantities of angular dispersion [OKH+04, OKK+05]. Spatial dispersion will also be introduced by transmitting a beam through glass at an angle other than normal to the surface. Spatial dispersion will lead to a reduction of the effective spectrum at each point in the beam, and is usually undesirable.

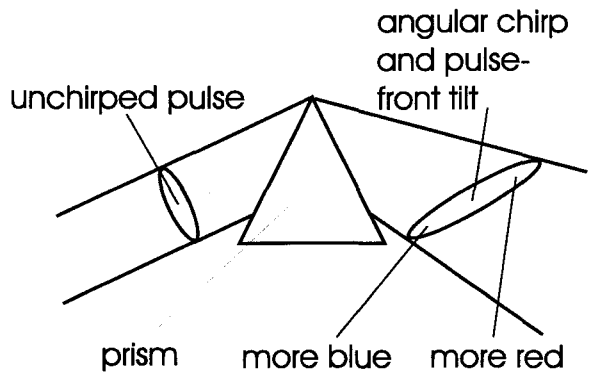

Figure 2.11: An undispersed pulse gains angular dispersion and pulse-front tilt when it passes through a prism.

Angular dispersion occurs whenever the laser beam passes through a

region where different transverse sections of the beam have different optical path lengths. In practice, this is usually realized in wedged optics, with the prism as the ideal example. When a polychromatic laser beam passes through a prism (or wedged optic) in general different frequencies refract at different angles (see figure 2.11). For a prism in particular, the relation is [BRS+93]

$$\frac{d\Theta}{d\lambda} = \frac{a}{b}\frac{dn}{d\lambda} \tag{2.60}$$

$\frac{a}{b}$ will be a geometrical factor on the order of one (see section 3.2 for more details), and Θ is the prism output angle.

Like "spatial chirp", there is some ambiguity around the definition of angular dispersion. Angular dispersion is the change in angle of the beam with respect to wavelength. One can speak of the angle between the propagation directions, or the angle between the phase fronts, which will be different for a beam with a Gaussian spatial profile. Varjú et al. [VKOK02] suggest that the angle between the phase fronts of the beam is the more relevant quantity. They derive an equation relating the angles

$$\Delta\Theta' = \Delta\Theta\frac{d\,(d + \alpha^2 s) + z_R^2}{(d + \alpha^2 s)^2 + z_R^2} \tag{2.61}$$

where $\Delta\Theta'$ is the spread of phase front angles, and $\Delta\Theta$ is the spread of propagation direction angles, d is the distance between the beam waist and the angularly dispersive optic, s is the distance from the angularly dispersive optic and the point of measurement, z_R is the Rayleigh length, $\alpha = \frac{\partial\Theta}{\partial\theta}$ and θ is the incident angle on the dispersive optic. It is the angle between the phase fronts that Varjú et al. [VKOK02] claim will lead to pulse front tilt in the laser pulse.

Different frequencies will experience different optical path lengths as they traverse the prism, leading to different delays. Since these different

frequencies are also propagating at different angles, a delay of the peak intensity front with respect to the phase front as a function of transverse position will be induced. The phase front will stay perpendicular to the propagation direction, but the peak intensity front will be tilted by an angle γ, given by [BRS+93]

$$tan(\gamma) = -\lambda \frac{d\Theta}{d\lambda} \tag{2.62}$$

Equations 2.60 and 2.62 are derived in [BRS+93] and references therein. The pulse front tilt is often quoted in units of fs/mm. These units can be achieved by dividing the tilt angle by the speed of light: $PFT_{AD} = \gamma/c$.

Pulse front tilt can also be generated by a combination of spatial dispersion and temporal dispersion. Akturk et al. [AGZT04] point out that there is a second term that contributes to the pulse-front tilt that is equal to the product of the frequency gradient and the group delay dispersion.

$$PFT_{TD+SD} = \Phi_2 \nu \tag{2.63}$$

then the total pulse front tilt is given by [AGZT04]

$$PFT_{tot} = PFT_{TD+SD} + PFT_{AD} \tag{2.64}$$

Angular dispersion and pulse front tilt will lead to temporal broadening if a pulse is focused. Pretzler et al. [PKW00] define a ξ factor linking angular dispersion to pulse broadening in a focus

$$\xi = \frac{T_0'}{T_0} = \sqrt{1 + \left(\frac{d\Theta}{d\lambda}\frac{\pi}{2ln2}\frac{\Delta\lambda}{\lambda_0}d_{FWHM}\right)^2} \tag{2.65}$$

They predict that the spatial electric field will also be broadened, with a profile proportional to

$$E(x) \propto \exp\left(-2\left[\frac{x}{\omega_0 \xi}\right]^2\right) \tag{2.66}$$

These effects combine to cause the effective intensity of the focal volume to be reduced by a factor of ξ^2. Derivations of equations 2.65 and 2.66 can be found in reference [PKW00].

If a pulse is assumed to have a Gaussian spatial profile and temporal profile with FWHM widths of w and T_0 respectively, and a pulse front tilt of PFT, an estimate of the focal temporal broadening can be calculated by integrating with respect to the transverse position x.

$$\int_{-\infty}^{\infty} \left\{\exp\left[\frac{-(x-x_0)^2}{w^2}\right]\right\} \left\{\exp\left[\frac{-(t-PFT(x-x_0))^2}{w^2}\right]\right\} dx \propto \exp\left(\frac{-t^2}{T_0^2 + w^2 PFT^2}\right) \tag{2.67}$$

This models the effect of a beam focused to a spot size smaller than a detector used to measure it and leads to a broadened temporal Gaussian width given by

$$\xi = \frac{T_0'}{T_0} = \sqrt{1 + \left(\frac{PFTw}{T_0}\right)^2} \tag{2.68}$$

which can be shown to be equivalent to equation 2.65 for Fourier transform limited pulses with Gaussian spatial and temporal profiles. It is also required that equation 2.62 hold, as it will for pulses without significant spatial and temporal dispersion.

For a numerical example, consider the effect a residual angular dispersion of just 2 μrad/nm. This amount of angular dispersion is difficult to measure, and easily overlooked. Angular dispersion will have the largest effect on pulse duration in a focus. Assume a pulse with a duration of 50 fs, beam width of 2 mm at 800 nm. An angular dispersion of 2 μrad/nm corresponds to a tilt angle of 1.6 mrad for a pulse centred at 800 nm. This in turn

corresponds to a pulse front tilt of 5.3 fs/mm. In the focus of an $f = 50$ mm focussing mirror, the duration of this nominally 50 fs pulse becomes 60.6 fs, a 20% increase in duration. Since the spatial axis that contains the tilt will also broaden by the same factor, the overall reduction in intensity in the focus is 30%, a significant fraction.

A final spatio-temporal effect can increase the pulse duration of a laser pulse. With sufficient spatial dispersion, the effective bandwidth at a point will be reduced. Assuming that the time-bandwidth-product of the pulse remains constant, this results in a broadening of the pulse duration, given by Akturk et al. [AGZT04] as

$$T = T_0 \sqrt{1 + 2\ln 2 \left(\frac{2\zeta}{wT_0}\right)^2} \tag{2.69}$$

This is however a small effect. For example, 1 meter away, after a 3 mm wide 50 fs long pulse traverses a SF10 prism, the pulse will broaden to 51 fs.

Spatial dispersion, angular dispersion and pulse front tilt are in general difficult to measure directly. Transverse separation of frequency components far less than the radius of the beam and tilt angles of mrads can adverse effects on pulsed experiments. These effects lead to problems with focused pulses and coupling into nonlinear devices like optical parametric amplifiers (OPA) [SSK98]. In order to achieve their specified OPA performance, Light Conversion Ltd. for example quotes their OPA's have a tolerance to PFT of less than 10% of the pump pulse duration. For a 50 fs duration, 1 mm diameter beam, this translates to a PFT of just 5 fs/mm. This is a small amount of PFT; it would be very difficult to detect with standard diagnostic techniques. Diagnosis, control or reduction of these effects are important in many high precision laser applications, so several diagnostic methods have been developed to measure spatio temporal distortions.

Chapter 3

Experimental Background

3.1 Generating Ultrafast Laser Pulses

The fundamentals of laser operation can be found in numerous sources and will not be covered in detail here. The reader is directed to books such as Milonni and Eberly [ME88] for a rigorous treatment.

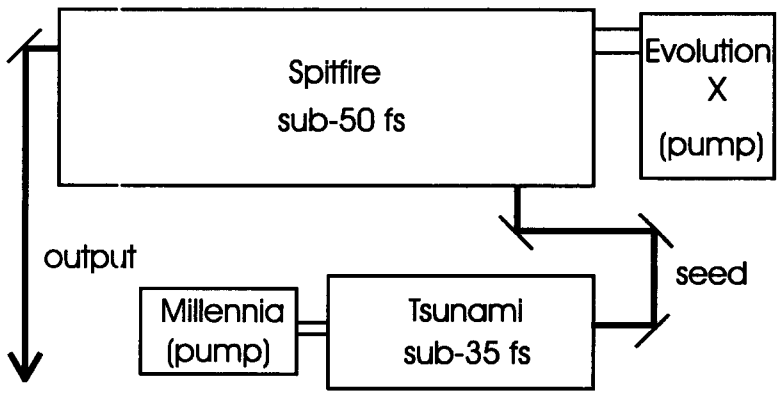

Figure 3.1: The oscillator amplifier laser setup. The Tsunami oscillator is pumped by the Millenia, producing an ultrafast seed pulse. This seed pulse is amplified in the Spitfire, which is pumped by the Evolution X.

The laser system used throughout this thesis is a Tsunami/Spitfire combination from Spectra-Physics (see figure 3.1). Laser light in the Tsunami is generated from excited Ti^{3+} ions which are dopants in a sapphire crystal.

The Tsunami is pumped collinearly with continuous-wave (cw) 532 nm light produced in a Millennia Vs. The Millennia Vs is a TEM_{00} laser, with Nd^{3+} ions in Nd:YVO_4 which is in turn pumped by laser diodes. The Millennia Vs produces 1063 nm light, which is frequency doubled in a temperature tuned LBO crystal to 532 nm.

Laser	Repetition Rate	Typical Average Power	Pulse Duration	Wavelength
Millennia Vs	cw	4.25 W	cw	532 nm
Tsunami	75 MHz	300 mW	<35 fs	800 nm
Evolution X	1 kHz	5.8 W	150 ns	527 nm
Spitfire	1 kHz	600 mW	<50 fs	800 nm

Table 3.1: Laser system properties.

Mode locking causes the longitudinal modes of the laser cavity to come into phase, creating a short pulse. Active mode locking causes the phases of the longitudinal modes to lock to an external signal, and passive mode locking causes the modes to lock in phase with respect to each other through some passive means. An example of active mode locking is acousto-optic modulation, which creates a time dependent loss in the cavity, creating pulses. Examples of passive mode locking are saturable absorption, which acts to steepen the leading edge of a pulse, and gain saturation, which ends to steepen the trailing edge of the pulse [DR96, ME88]. Kerr lens mode locking is another type of passive mode locking.

Kerr lens mode locking relies on self focussing in a Kerr nonlinear medium. An aperture placed in the cavity can selectively transmit self focused modes, leading to an intensity dependent loss in the laser cavity. This configuration will prefer high power, and thus pulsed operation. Because the Kerr nonlinearities are almost instantaneous, one can imagine the Kerr lens material acting as an ultrafast saturable absorber to produce ultrafast pulses [BSCK92].

The Tsunami pulses are created through Kerr lens mode locking, where the Kerr nonlinear medium is the Ti:Sapphire crystal itself. The intensity dependent loss is created by having a higher overlap between the pump mode and the cavity modes in the crystal when the cavity modes are self focused than when they are not. The Tsunami uses an acousto-optic modulator to initiate Kerr lens mode locking.

The Ti:Sapphire crystal of the Tsunami has a gain bandwidth of approximately 690-1080 nm, meaning the crystal can be tuned within this range. In operation the spectrum of the Tsunami pulses are determined by the mirror set used. The Tsunami used in this thesis usually has an output bandwidth of 35 nm, centred on 800 nm, and is tunable over a small range around 800 nm.

The output of the Tsunami is then sent into the Spitfire regenerative amplifier, where it undergoes chirped pulse amplification [MSB+88] (see figure 3.2). It passes through a grating based stretcher, then into a cavity with a Ti:Sapphire crystal pumped with an Evolution-X laser (527 nm, 150 ns pump beam), where it is amplified. It is then dumped from the cavity by Pockels cells controlled by a synchronization delay generator (SDG) box. Afterward, it is re-compressed with a grating based compressor. An ultrafast, high peak intensity pulse is the result.

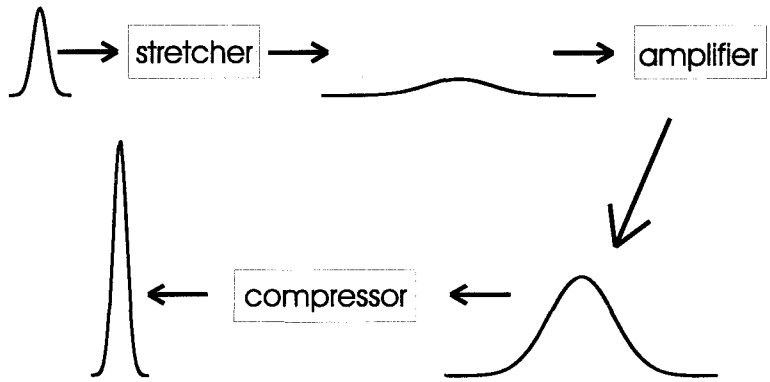

Figure 3.2: Schematic of chirped pulse amplification. A low intensity ultrafast pulse is stretched in time through dispersion, amplified and then recompressed to generate a high power ultrafast pulse.

3.2 Inducing Angular, Spatial and Group-Delay Dispersion

Dispersive prisms and gratings are useful in a number of applications. Since they will have the same effect on a laser pulse, only prisms will be considered explicitly, but similar formulae apply for gratings. Gratings will in general be capable of providing larger amounts of angular dispersion, but they are also lossier. Combinations of prisms can be used to introduce arbitrary amounts of spatial and angular dispersion, as well as group velocity dispersion [FMG84].

A single prism will introduce negative group delay dispersion (GDD) to a laser beam, as a result of it passing through the prism material. It will also introduce angular dispersion, as different frequencies of light are refracted through different angles. The general form for the angular dispersion introduced by a single prism is

$$\begin{aligned} \frac{\partial\Theta}{\partial\lambda} &=: \frac{\sin(J)+\cos(J)\sin(\theta)\left(n^2-\sin^2(\theta)\right)^{-1/2}}{\sqrt{1-n^2\sin^2(J)}}\left(\frac{\partial n}{\partial\lambda}\right) \\ J &=: \phi-\sin^{-1}\left(\frac{\sin\theta}{n}\right) \end{aligned} \tag{3.1}$$

where Θ, θ and ϕ are the output, input and apex angle of the prism respectively, and n is the ratio of the index of refraction of the prism with the index of refraction of air. This equation is derived assuming plane waves, or in the ray optics picture, and agrees with Kostenbauder's result [Kos90]. Gaussian beams will behave differently, but as their Rayleigh range increases, they will approach this solution (see [VKOK02] or [AKOT03a] for more details). When the angle of incidence equals the angle of output (angle of minimum deviation), and the apex angle of the prism is cut for Brewster angle incidence (minimum reflection losses), equation 3.1 reduces to [DR96]

$$\frac{\partial\Theta}{\partial\lambda} = -2\frac{\partial n}{\partial\lambda} \tag{3.2}$$

An interesting and useful feature of a pair of prisms is that they can be aligned in such a way as to cancel each other's angular dispersion, and be used to generate negative GDD (see figure 3.3) without angular dispersion. A simple way to think of this is that geometrically, higher frequency light travels a shorter distance than lower frequency light. Fork [FMG84] derives equations for the GDD of this prism geometry, simplified by Diels [DR96]

$$GDD = \frac{\partial^2\Phi}{\partial\omega^2} = -4l\frac{\lambda_0^3}{2\pi c^2}\left(\frac{dn}{d\lambda}\right)^2 \tag{3.3}$$

where Φ is the spectral phase and λ_0 is the central wavelength of the laser pulse.

This configuration still leaves spatial dispersion. To subject a pulse to

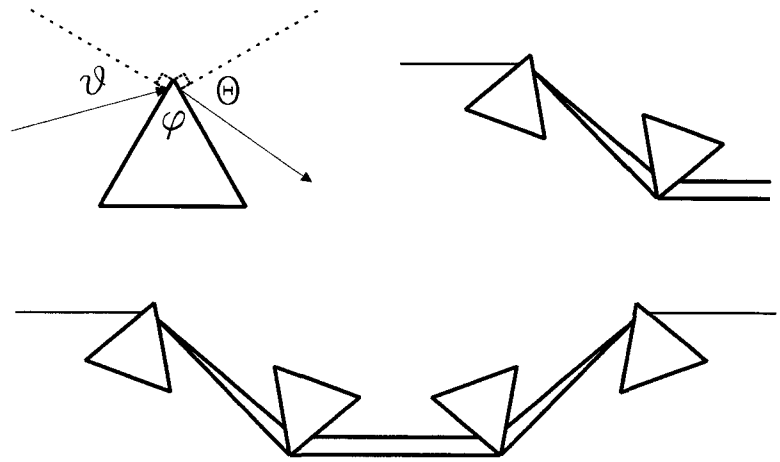

Figure 3.3: Clockwise from top left: The geometry of a laser intersecting a prism can be defined by the parameters ϑ, ϕ and Θ for the incident angle, apex angle and output angle respectively. A single prism will induce angular dispersion. The angular dispersion from a single prism can be compensated by a second prism with identical but opposite geometry. Four identical prisms compensate spatial dispersion.

negative GDD without spatial dispersion, a retro-reflecting mirror is placed at the output of the above configuration, causing the beam to retrace its path. Two more prisms can be used to achieve the same effect. This doubles the total GDD of the system, and results in a beam without spatial dispersion. When passing through a prism, an ultrafast pulse will also undergo a small amount of material GDD. This is usually minimized by propagating the beam through the prism at its tip. The GDD induced by material dispersion in a prism is given by

$$GDD = \frac{\lambda_0^3}{2\pi c^2} L \frac{d^2 n}{d\lambda^2} \tag{3.4}$$

where L is the length of prism material traversed by the pulse. For very short pulses, the third order dispersion induced by the prism must also be considered. It is given by [DR96]

$$TOD = \frac{d^3\Phi}{d\omega^3} = \frac{12L\lambda_0^4}{(2\pi)^2c^3}\left\{\left(\frac{dn}{d\lambda}\right)^2\left[1-\lambda_0\frac{dn}{d\lambda}\left(n^{-3}-2n\right)\right]+\lambda_0\left(\frac{dn}{d\lambda}\frac{d^2n}{d\lambda^2}\right)\right\} \quad (3.5)$$

If the intensity of a laser pulse is great enough, the nonlinear effects discussed in section 2.9.2 will also need to be considered.

3.3 Transmission and Reflection Optics

When dealing with broadband femtosecond laser pulses, new factors emerge that were not problems with longer laser pulses. To ensure that the pulses delivered to an experiment are as short and intense as needed it is important to understand how each optical component in an apparatus will affect the pulse.

If a particular experiment demands close to the maximum power output from the available laser system, it is important to have highly reflective mirrors. In addition, since ultrafast lasers necessarily have large bandwidths, mirrors with high reflectivity over a broad bandwidth are needed. A common way to construct a mirror that satisfies the broadband and high reflectivity requirements simultaneously is to build it out of a stack of dielectric layers, each highly reflective to a particular frequency range.

The problem with this solution is that in general mirrors will induce a spectral phase shift that will lead to GDD, and other temporal distortions, even if they are 100% reflective. This is because of a non-constant spectral phase response. In other words, different frequencies will travel different distances, leading to a temporal dispersion induced in the laser pulse, which will reduce its peak power. An example of the effect of non-ideal mirrors can be seen in figure 3.4.

In order to produce mirrors that maintain the spectral phase of femtosecond pulses, the many layers must be phase matched in a very precise way, flattening the phase response, and substantially increasing their cost. If reflectivity is not of primary concern, it is also sufficient to use metallic mirrors, which have a very small skin depth.

The dispersive effect of mirrors can also be exploited by creating mirrors that have a very specific phase response and induce a very specific temporal chirp in the pulse (see figure 3.5 for a schematic). This is a way for example of

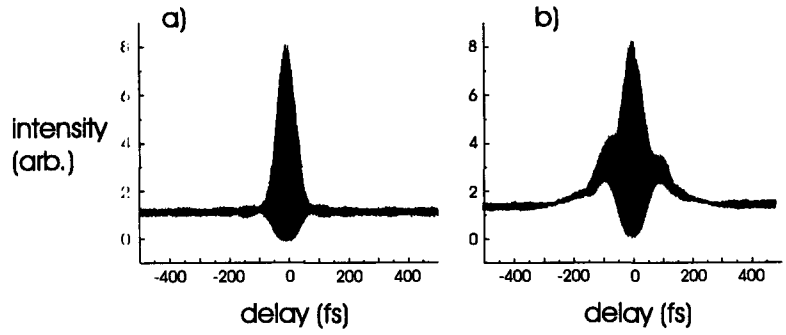

Figure 3.4: Interferometric autocorrelation of (a) amplified laser output pulses, and (b) pulses reflected off four non-ideal dielectric mirrors.

applying an effective negative GDD to a laser pulse that has undergone SPM, and recompressing the pulse. It is a good method because of its extremely high power throughput.

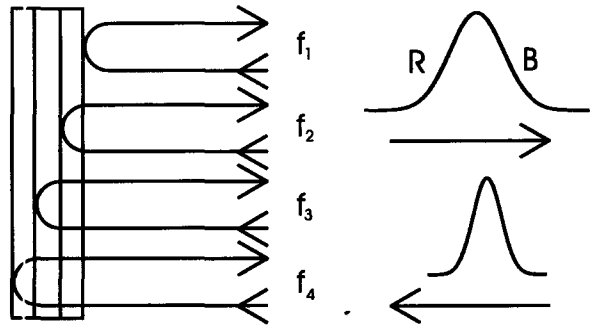

Figure 3.5: Schematic of chirped mirror. In this figure, f_4 must travel a greater distance than f_1 inducing a delay between these frequencies. This manifests as temporal chromatic dispersion in an ultrafast pulse.

The effects of lenses on ultrafast pulses must also be considered. Often, ultrafast lasers are used in applications that attempt to generate maximal optical intensity. This requires both excellent temporal focussing and excellent spatial focussing. When it is desirable to approach the diffraction limit for a given wavelength, some new phenomena must be understood.

There are many limits on the ability of a lens to focus light. The most fundamental of these is the diffraction limit. The diffraction limit on spot size for a circular lens is

$$w \propto \frac{\lambda f}{d} \tag{3.6}$$

where w is the radius of the focused spot, λ is the wavelength of the light, f is the focal length of the lens and d is the lens diameter.

Other geometrical limits on spot sizes come from lens aberrations. These can be analyzed using the ray or geometric theory of optics (see section 2.2). There are many other ways that an image can be distorted. In order to control distortion, it is divided into several categories or aberration types (see for example [JW57] for a treatment of lens aberrations).

A perfect lens would have a parabolic surface, but these are difficult in practice to produce, so spherical lenses are used instead. This introduces spherical aberration. One can also think of spherical aberration as due to the breakdown of the paraxial approximation $sin(\theta) \rightarrow \theta$. The effect of spherical aberration is to cause collinear incident rays of light to have a focal length that varies with transverse displacement from the center of the lens. This will lead to a focus for large diameter beams that is "smeared out". Spherical aberration can be corrected using multiple or compound lenses.

A spherical singlet lens will also delay the pulse front with respect to the phase front of the pulse differently across the width of the lens (see figure 3.6). The following three equations are developed in Diels' text [DR96] following and adding to the work of Bor [Bor89]. They are first approximations to the effects of lens distortions, derived under the ray picture of light.

The increase in the duration of the pulse is given by

$$\Delta T = -\frac{w_i^2}{2cf(n-1)}\left(\lambda_0 \frac{\partial n}{\partial \lambda}\right) \tag{3.7}$$

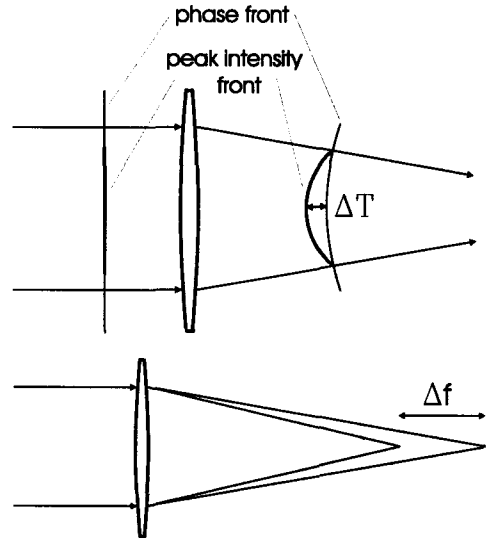

Figure 3.6: Top: distortion in peak intensity and phase fronts cause by a spherical singlet lens. ΔT is the induced delay between the centre and outside of the pulse given by equation 3.7, and due to spherical abberation. Bottom: distortion in focal point caused by chromatic aberration. Δf is the degree to which the focal length is "smeared out", given by equation 3.8.

where w_i is the radius of the beam incident on the lens, f is the focal length of the lens, n is the index of refraction of the lens.

The extent to which the index of refraction of the lens changes with wavelength will determine the extent to which the focal length of the lens is "smeared out" Δf, given by

$$\Delta f = -\frac{f\lambda^2}{c\,(n-1)}\frac{0.441}{T_0}\frac{\partial n}{\partial \lambda} \tag{3.8}$$

The width of the beam at the waist will also increase by a factor of

$$\frac{w}{w_0} = -\frac{0.441\pi}{2T_0}\frac{w_i^2}{cf\,(n-1)}\left(\lambda\frac{\partial n}{\partial \lambda}\right) \tag{3.9}$$

where T_0 is the FWHM duration of the pulse.

As an example of these effects, consider a 3 mm radius beam, with a

wavelength of 800 nm and a pulse duration of 50 fs, focused by a 75 cm focal length BK7 singlet lens ($n = 1.5106$, $dn/d\lambda = -2.0 \times 10^{-2}$ μm^{-1}), as is used in section 5.3 to couple laser light into a hollow capillary. The temporal broadening caused by the singlet lens will be 0.6 fs, the smearing of the waist location will be 560 μm (as compared to a Rayleigh range of 16 cm), and the beam width at the waist will increase by a factor of 0.02. These are negligible distortions.

It is worth the effort to estimate the magnitude of these effects however, as they are not always negligible. The distortions become large for larger input beams, smaller focal spots and shorter wavelengths. Consider for instance Diels' example of an excimer laser, producing a 4 mm radius beam, at a wavelength of 248 nm and a pulse duration of 50 fs, focused by a 3 cm focal length fused silica singlet lens ($n = 1.5121$, $dn/d\lambda = -72 \times 10^{-2}$ μm^{-1}) [DR96]. Under these conditions the pulse duration will broaden by 300 fs, the focal length be smeared by 80 μm (as compared to a Rayleigh range of 4.4 μm), and the waist width will increase by a factor of 9. These are definitely not negligible effects.

Planchon et al. demonstrate these distortion effects experimentally in a singlet beam expander [PFH+04]. They calculate the propagation time difference between different parts of a singlet lens. Their measurement of the total effect using second order intensity autocorrelation confirms their theoretical model and demonstrates an elongation of pulse length. Fuchs et al. have combined ray-tracing and wave-optical techniques to accurately model the propagation of ultrafast pulses through optical systems [FZT05]. They have demonstrated numerically the behaviour of ultrafast pulses in a tight focus.

Of course normal material dispersion will also act to broaden the pulse, as the above aberrations continue to affect the focal volume. Achromatic doublet lenses can correct to a degree problems with chromatic dispersion

leading to smearing out of the focus and radially varying group delay. Higher order dispersion effects will remain, which is a problem especially for very short pulses. Curved mirrors can be used, and will get around most problems. These however are difficult to align and are costly. Jasapara et al. have shown however that dispersion pre-compensation of pulses focused through lenses can reduce the effect of distortion [JR99]. Angular dispersion will also lead to a reduction in the intensity of a focused pulse and broadening of its temporal profile; see sections 2.10 and 4.2.

3.4 Numerical Modeling

The dimensionless propagation equation (equation 2.33) can be used to simulate the propagation of a laser pulse through a medium with some dispersion and some third order nonlinearity. The following discussion is adapted from Agrawal's text [Agr89]. Symbols used in this section are defined in section 2.7.

This propagation equation is valid as long as the slowly varying envelope approximation holds ($\delta\omega \ll \omega_0$). Depending upon the implementation and carrier frequency, this can mean 20-50 fs. When this approximation is no longer sufficient, to get very accurate solutions Maxwell's equations must be integrated directly.

The propagation equation is a nonlinear partial differential equation, and cannot be solved analytically in general. It must be integrated numerically. Numerical solutions are mainly of two types: finite difference methods, and pseudo spectral methods. The method used in this work is the split step Fourier method, which falls into the second category. It is faster than finite difference methods for the same accuracy by up to a factor of 100 [Agr89].

To develop the split step Fourier method, the first step is to write the propagation equation in the following way

$$\frac{\partial u}{\partial z} = \left(\hat{D} + \hat{N}\right) \tag{3.10}$$

where $\hat{D}$ and $\hat{N}$ are dispersive and nonlinear differential operators given by

$$\hat{D} = -\frac{1}{L_L} - \frac{\imath}{2L_D}\frac{\partial^2}{\partial\tau^2} + \frac{1}{6L'_D}\frac{\partial^3}{\partial\tau^3} \tag{3.11}$$

and

$$\hat{N} = \frac{\imath}{L_{NL}}\left[|u|^2 + \imath C_S\frac{\partial\left(|u|^2u\right)}{\partial\tau} + C_R\frac{\partial|u|^2}{\partial\tau}\right] \tag{3.12}$$

The formal solution to equation 3.10 is then given by

$$u(z,\tau) = \exp\left[\left(\hat{D}+\hat{N}\right)z\right]u(0,\tau) \tag{3.13}$$

which cannot of course be evaluated analytically. It is possible to get around the noncommutivity of $\hat{D}$ and $\hat{N}$ by dividing the z into tiny steps. In each of these steps, the two operators will approximately commute,

$$u(z+\Delta z,\tau) = \exp\left(\hat{D}\Delta z\right)\exp\left(\hat{N}\Delta z\right)u(z,\tau) \tag{3.14}$$

The dispersive piece is easily solved in the Fourier domain, where all derivatives in the dispersive operator can be replaced with $\imath\omega$. ($\frac{\partial}{\partial\tau} \rightarrow \imath\tilde{\omega}$, where $\tilde{\omega} = \omega T_G$ is the reduced frequency).

In the end the procedure for numerically integrating equation 3.10 is this:

1. Fourier transform the signal $U(\tau)$ into the frequency domain $U(\omega)$.

2. Apply the Fourier transformed dispersive operator $\hat{D}$ (just a phase factor).

3. Inverse Fourier transform $U(\omega)$ back into $U(\tau)$.

4. Apply the nonlinear operator $\hat{N}$ (also a phase factor, but slightly more complicated).

This takes the signal from z to $z + \Delta z$. In order to propagate through a nonlinear and dispersive region of distance d, simply divide d into $N = d/\Delta z$ steps and apply the above procedure N times. The error in this method increases as $(\Delta z)^2$, so by choosing small Δz one can achieve negligible error.

A computer program was written in Microsoft Visual C++ to simulate the propagation of pulsed laser solutions, using the split step Fourier technique, as described above. Figures 2.2, 2.4 and 2.6 through 2.9 were generated using this program.

3.5 Beam Profiling

The spatial profile of a laser beam $F(x, y)$ can be determined directly with a camera, or computed from data taken by scanning a spatial filter across the beam. The advantage of a direct beam profile measurement using a CCD camera is that the results are instantaneous, and presented in two dimensions. Unfortunately, a direct measurement with a camera alone cannot spectrally resolve the beam profile, and perhaps more importantly will only work for beams of a small range of sizes. This is because a large beam will overfill the CCD, and a small beam will be poorly resolved (perhaps filling only a few pixels). This problem can be rectified somewhat by placing lens combinations before the CCD in order to shrink or expand the beam, but the measurement in this case is no longer direct. To get a profile in a focus especially, it is necessary to use other techniques.

If some kind of spatial filter is scanned across the beam, and transmitted light recorded on a photodiode, the result is a plot of intensity versus position. This plot will be the convolution of the beam profile with the spatial filter profile.

$$I(x) = F * r = \int_{-\infty}^{\infty} F(x')\, r(x - x')\, dx' \tag{3.15}$$

where $I(x)$ is the retrieved signal, $F(x)$ is the beam profile integrated in the y-axis, and $r(x)$ is the response function of the spatial filter. The beam profile can then be obtained using deconvolution by the relation

$$F(x) = IFT\left(\frac{FT(I(x))}{FT(r(x))}\right) \tag{3.16}$$

where FT is the Fourier transform, and IFT is the inverse Fourier transform.

If the spatial filter is the straight edge of a blade, the spatial filter function becomes a step function, and equation 3.16 becomes simply

$$F(x) \propto \frac{dI(x)}{dx} \tag{3.17}$$

or the beam profile is given by the derivative of the raw signal. This is a very simple technique, and is applicable to beams of any size (though for very small beam widths, one must consider diffraction effects). It is slower than direct measurement with a CCD, but more versatile, and it also allows the simultaneous measurement of a spectrum, by collecting the light with a spectrometer instead of a photodiode. An example knife-edge scan is depicted in figure 3.7

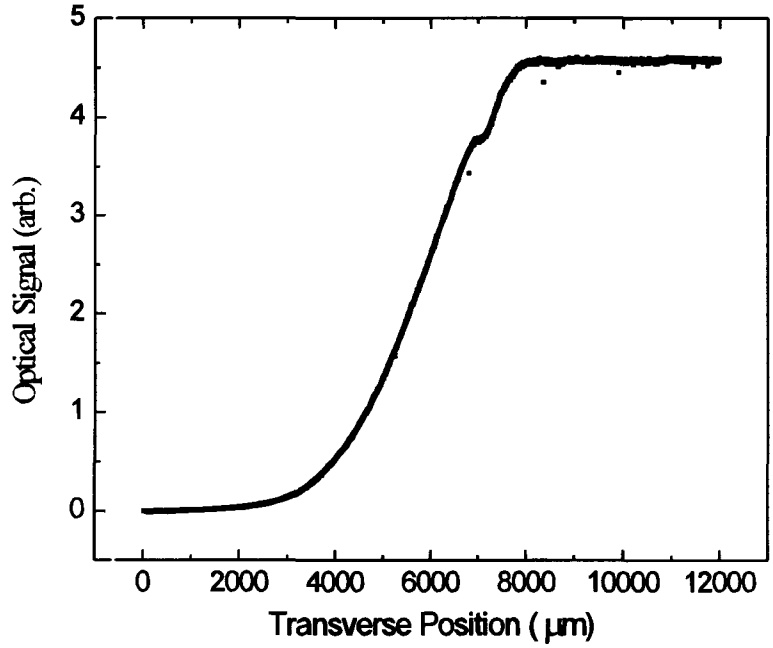

Figure 3.7: A knife-edge scan of the amplified laser beam. An erf function fit results in a $1/e^2$ radius of 2.7 mm. The "notch" that can be observed near 7000 μm is due to a reflection from a neutral density filter. It has a small effect on the retrieved beam radius.

3.6 Autocorrelation

Since it is usually the case that ultrafast laser pulses are the shortest easily manipulated events an experimenter has access to, measuring their temporal profile is difficult. A good first step in the diagnosis of short laser pulses is the autocorrelation [Arm67]. Conceptually, the autocorrelation works by splitting the pulse into two copies. It uses the first copy as a gate which is scanned across the second copy, using a variable time delay. The resulting signal is an autocorrelation of the pulse. There are two types of simple autocorrelation commonly used: the second order intensity autocorrelation and the second order interferometric autocorrelation.

3.6.1 Interferometric Autocorrelation

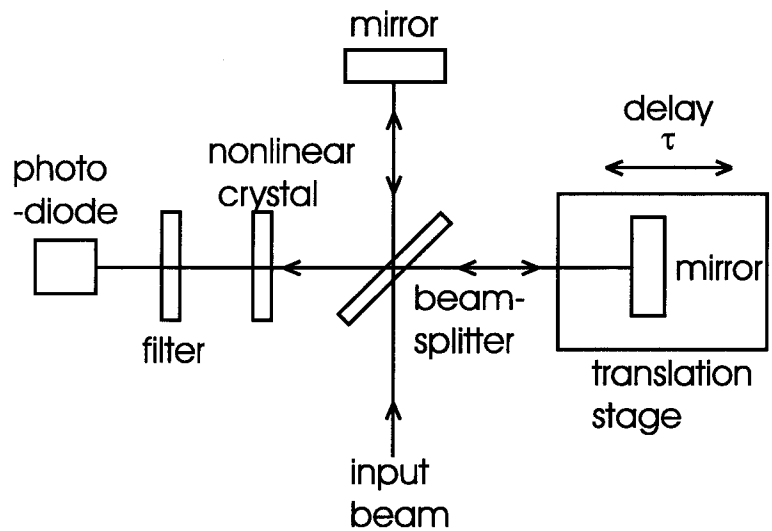

Figure 3.8: Schematic of an interferometric autocorrelator.

The second order interferometric autocorrelation uses the setup depicted in figure 3.8. Two collinear copies of the beam are overlapped with a variable

time delay in a nonlinear crystal. The second harmonic light generated in the nonlinear crystal is recorded as a function of delay. The signal is described analytically by [DR96]

$$A(\tau) = \int_{-\infty}^{\infty} \{[E_1(t-\tau) + E_2(t)]^2\}^2 dt \tag{3.18}$$

where E_1 and E_2 are the electric fields of the two copies of the pulse, and τ is the temporal delay.

If the pulse is assumed to have only linear temporal dispersion, equation 3.18 can be expanded to read [DR96]

$$\begin{aligned} A(\tau) \quad &= 1 + 2\exp\left[-(\tau/\tau_G)^2\right] + 4\exp\left[-\tfrac{C^2+3}{4}(\tau/\tau_G)^2\right]\cos\left[\tfrac{C}{2}(\tau/\tau_G)^2\right]\cos(\omega\tau) \\ &\quad +2\exp\left[-(1+C^2)(\tau/\tau_G)^2\right]\cos(2\omega\tau) \end{aligned} \tag{3.19}$$

where τ_G is the Gaussian width of the autocorrelation pulse, C is a dimensionless parameterization of the temporal dispersion or "chirp" and ω is the carrier frequency of the pulse. Since this equation is sensitive to the temporal dispersion in the pulse, the interferometric autocorrelation can be used to diagnose and minimize temporal dispersion in the pulse (see figure 3.9). Full phase information is still not available though, and the pulse amplitude still cannot be unambiguously determined. See figure 3.10 for an experimental example of an interferometric AC.

3.6.2 Intensity Autocorrelation

The second order intensity autocorrelation works by overlapping two copies of the pulse into a nonlinear crystal, with a non-zero angle between them (see figure 3.11). Where they overlap, the pulse is frequency doubled. Since momentum must be conserved, a third beam is created between the first

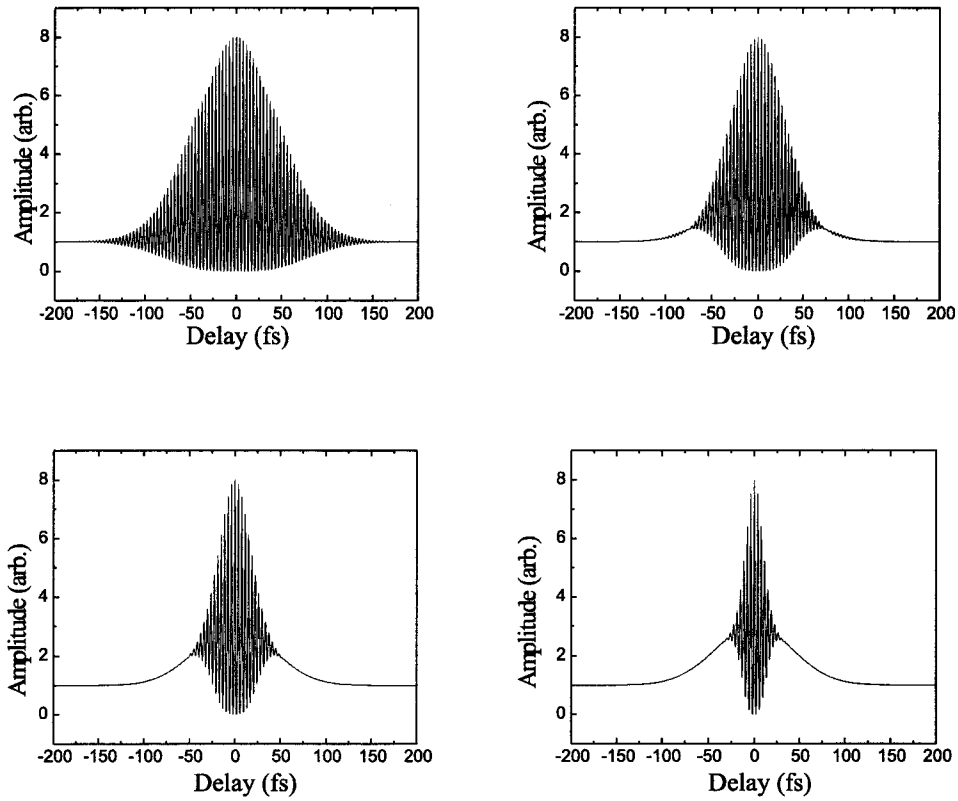

Figure 3.9: Theoretical autocorrelation traces of equal duration with second order temporal phase shifts given by (from left to right, top to bottom) C=0, C=2, C=4 and C=8.

two. The third beam is the signal beam which is recorded.

The intensity autocorrelation is given mathematically by

$$A(\tau) = \int_{-\infty}^{\infty} I(t)\, I(t-\tau)\, dt \tag{3.20}$$

where I is the intensity of the pulse. The intensity autocorrelation is insensitive to temporal dispersion (and any other phase distortion). See figure 3.12 for an example of experimental intensity AC.

Different pulses, each with the same duration, but different amounts of temporal dispersion, will each have the same intensity autocorrelation.

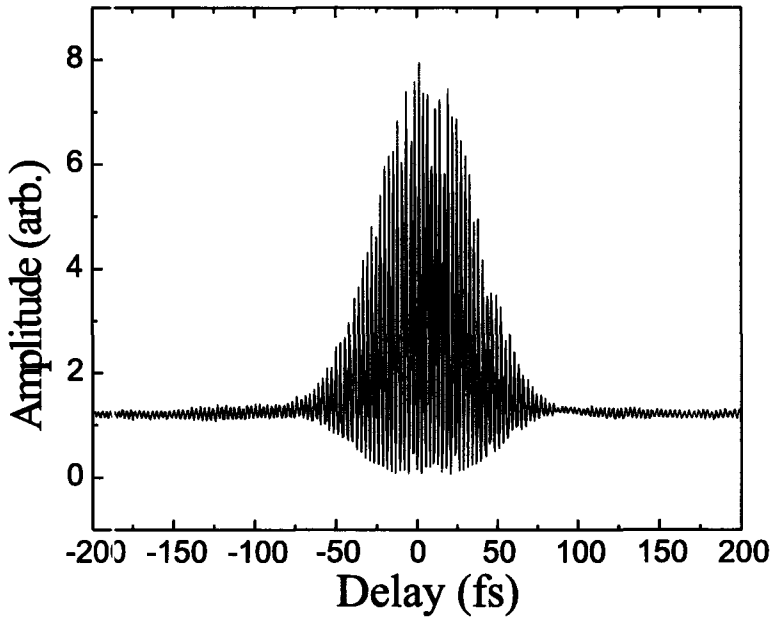

Figure 3.10: Experimental interferometric autocorrelation trace of amplified laser output. Duration is measured to be ~50 fs.

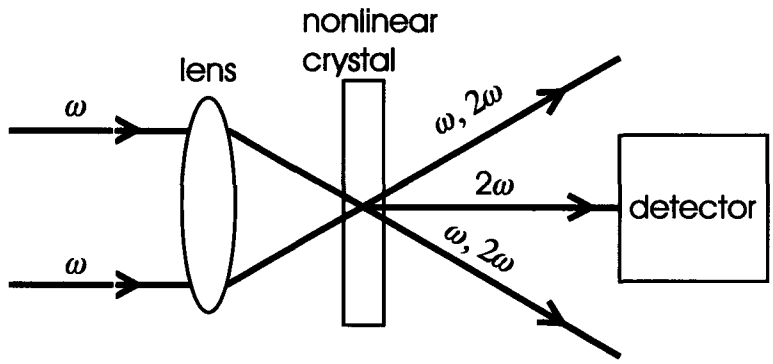

Figure 3.11: Two copies of a pulse are focused into a nonlinear crystal. Each beam will generate a collinear second harmonic beam. When overlapped in space and time, the two initial beams produce a third second harmonic beam, which is measured. Angles are exaggerated for clarity.

A pulse with a Gaussian temporal profile will have a Gaussian intensity autocorrelation trace.

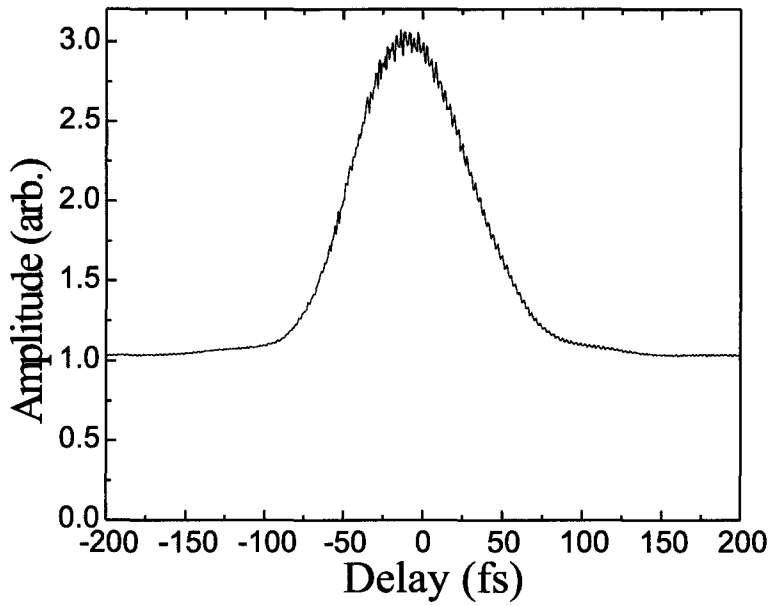

Figure 3.12: An example of experimental intensity autocorrelation for amplified laser output (~50 fs).

3.6.3 Convolution

Autocorrelations of all types are a kind of self-convolution integral of the electric field amplitude, or its intensity. The convolution operator $f \otimes g$ is defined as

$$(f \otimes g)(x') = \int f(x)g(x - x')dx \tag{3.21}$$

When f and g are the same function, this is called the autoconvolution function. When the autoconvolution is performed on the intensity, the result is the intensity autocorrelation function.

Autocorrelations at best return the autocorrelation function of the intensity of the electric field, not the field itself. The typical procedure used to extract the intensity FWHM from the autocorrelation FWHM is to deconvolve the autocorrelation using a deconvolution factor. So for instance,

the FWHM of the autoconvolution integral of the Gaussian function is a factor of $\sqrt{2}$ times larger than the FWHM of the Gaussian intensity distribution [DR96, Tre00].

Function	Deconvolution factor
Rectangular	1.000
Gaussian	1.414
$Sech^2$	1.543
Lorentzian	1.654

Table 3.2: Deconvolution factors for four pulse shapes. Divide the intensity autocorrelation FWHM by the above numbers to get an estimate on the FWHM of the temporal intensity distribution.

To make an educated guess as the intensity FWHM duration of a pulse, the retrieved autocorrelation function is divided by the deconvolution factor of the function that is assumed to be the best fit to the experimental intensity distribution. Table 3.2 summarizes convolution factors for four pulse shapes. It should be noted that depending on the best fit function selected, the estimated pulse duration will differ significantly. Work comparing FROG with autocorrelation presented in [Tre00] suggests that for real pulses, the deconvolution factor is often close to 1.4, and rarely exceeds 1.5. For this reason, a Gaussian function is assumed in all autocorrelation deconvolutions in this thesis. The slowly varying component (the first three terms of equation 3.19) of the interferometric autocorrelation is equivalent to the intensity autocorrelation, and it is this piece that is used to estimate the autocorrelation FWHM in interferometric autocorrelation traces.

3.6.4 Single-Shot Autocorrelation

An intensity autocorrelator can be made to operate in single shot mode by replacing the photodiode with a CCD camera. In this mode, temporal

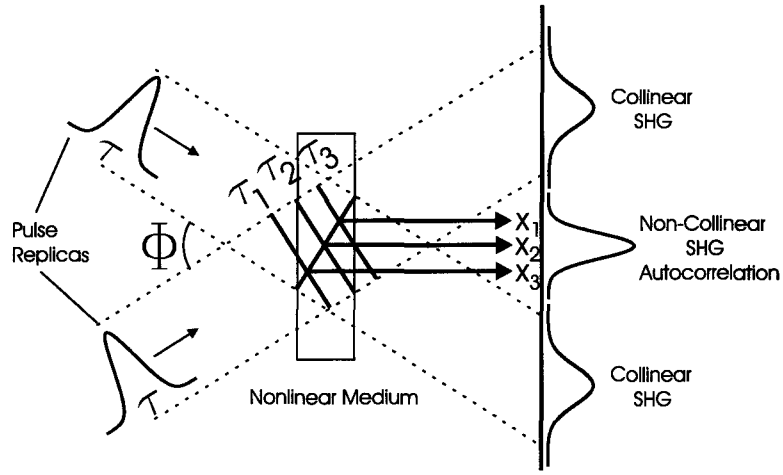

Figure 3.13: Two copies of a pulse are superimposed in a nonlinear crystal. Second harmonic light is generated non-collinearly and collinearly. Non-collinear signal is proportional to autocorrelation.

delay is translated into transverse displacement by superimposing the two non-collinear copies of the beam in a nonlinear crystal (see figure 3.13).

The relationship between the spatial shift measured on the CCD and the delay of the pulse is given by [SGRB87, BGSS91]

$$\Delta\tau = \frac{2\sin(\chi/2)}{c}\Delta x \tag{3.22}$$

where $\Delta\tau$ is time delay, Δx is transverse shift and χ is the angle between the beams external to the nonlinear crystal.

The intensity of the signal will vary in the x-axis (which is coplanar with the two copies of the pulse) and it will be proportional to the intensity autocorrelation. Typically the angle χ between the beams is not measured to determine the conversion between transverse shift and time delay, as this would prove a difficult measurement. For greater accuracy, a known delay is introduced in one arm of the autocorrelator, and the spatial shift is noted. A calibration constant can then be computed. The full-width-at-half-

maximum (FWHM) of the autocorrelation trace can be determined using the calibration constant. Once this value is known, the pulse FWHM can be determined using the standard deconvolution factors (i.e. divide by 1.414 if the pulse is assumed to have a Gaussian temporal profile).

3.6.5 Field Inversion Autocorrelation

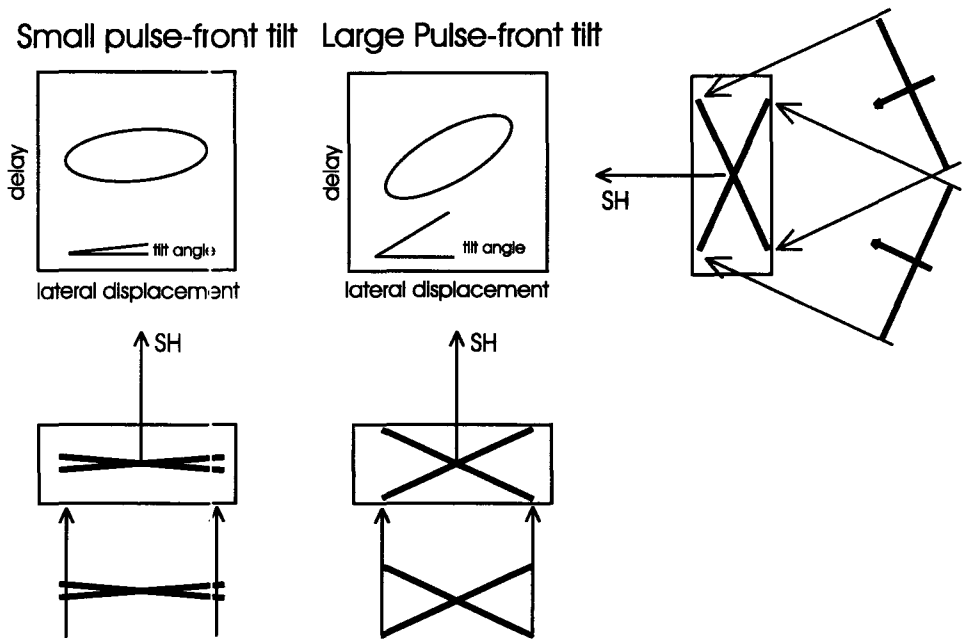

Figure 3.14: CCD readout of tilted pulse-front autocorrelator for pulses with slight tilt and large tilt. Tilt is measured as a shear of the SH image.

Simple autocorrelators do not measure pulse front tilt in laser pulses, unless great care is taken, as is discussed in section 4.2. It is possible to design an autocorrelator that is directly sensitive to pulse front tilt though. If the symmetry between the two arms of the autocorrelator is broken, in principle, spatio-temporal distortions can be detected. Pretzler et al. [PKW00] developed a fringe-resolved (interferometric) autocorrelator that could detect PFT. By inverting one arm of the autocorrelator, and imaging the interference of

the two beams on a CCD, the contrast function as a function of position could be resolved, which allowed a coarse measurement of the pulse front tilt. Sacks et al. [SMD01] suggest another device based on non-collinear single shot autocorrelation. This device measures PFT as a shear in the second harmonic signal, as measured on a CCD camera (see figure 3.14). Unlike the device developed by Pretzler et al [PKW00], this device can simultaneously measure both PFT and pulse duration. Raghuramaiah et al. [RSNG03] subsequently developed a formula for extracting the precise amount of PFT from the shear making this measurement quantitative.

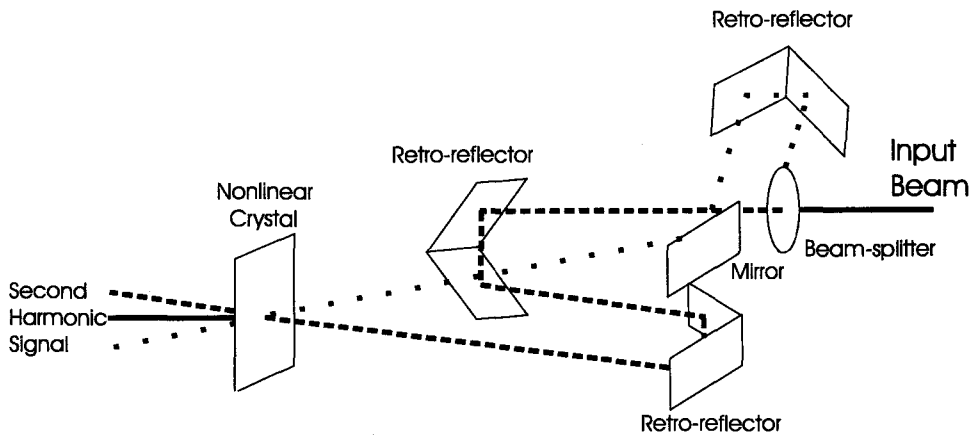

Figure 3.15: Schematic of tilted pulse-front autocorrelator.

The field inversion autocorrelator developed by Sacks et al. [SMD01] works by inverting the field of the pulse in the axis parallel to the optical table in one arm of the autocorrelator. This is accomplished by having the beam reflect from one additional mirror in one arm of the autocorrelator. The two copies are then brought together at a vertical angle in the nonlinear crystal (see figure 3.15). The output of the nonlinear crystal is imaged on a CCD camera. The delay axis of this device will be in the vertical axis of the camera, and the horizontal axis will represent transverse displacement. See figure 3.14.

The duration of the pulse is measured the same way as for a normal single shot autocorrelator, except that the delay axis is vertical instead of horizontal. The pulse-front tilt angle γ can be computed from the CCD tilt angle α using the equation derived in [RSNG03]

$$\gamma = tan^{-1}\left[\left\{1 - \left(\frac{\lambda_0}{n}\right)\left(\frac{dn}{d\lambda}\right)\right\}\tan(\alpha)\sin(\chi/2)\right] \tag{3.23}$$

where χ is the angle between the beams as they enter the nonlinear crystal and n is the refractive index of the nonlinear crystal. This design therefore allows simultaneous measurements of pulse duration and pulse front tilt, but it is still insensitive to the temporal phase of the pulse, and to the particular shape of its temporal envelope. To resolve these features, other techniques are necessary.

3.6.6 Autocorrelation Alignment

Autocorrelators (AC) are difficult to align properly, as they often have many sensitive degrees of freedom that can be adjusted. A misalignment of one of these degrees of freedom will lead to systematic errors.

There are a few steps that can be taken to ensure proper alignment of an AC. Firstly, to ensure that the AC is balanced, the power of the output can be measured with first one then the other arm of the AC blocked. The power in these two cases should be approximately equal, assuming the beam splitter is splitting the pulses equally. In addition, blocking the input of the AC should cause the output signal to go to zero. If these conditions are not satisfied, there may be stray light interfering with the AC. Alternatively, one or the other of the beam copies might have been clipped by either the autocorrelator arms or the beam splitter.

Further checks include ensuring that the AC has a peak signal to background ratio of 8:1 or 3:1 for interferometric or intensity AC respectively.

All autocorrelations should also be symmetric. If they are not, it is possible that the mirrors are not in perfect alignment, or that the photodiode has been saturated. To rectify this problem the power of the input beam should be reduced and the alignment of the mirrors should be checked by moving the translation stage back and forth manually. If the mirrors are in proper alignment, the beams on the output should not change position [DR96].

3.7 FROG and GRENOUILLE

If the photodiode or CCD of a standard second order intensity autocorrelator is replaced with a spectrometer, data can be collected in two independent variables instead of one: wavelength and delay instead of just delay. The two dimensional plot generated in this way is called a spectrogram. It turns out that the additional information is sufficient in principle to reconstruct the electric field of the pulse, both amplitude and phase. This technique was invented by Rick Trebino [TDF+97] and is called second harmonic frequency resolved optical gating (SH-FROG), and the spectrogram is referred to as a FROG trace.

Sophisticated algorithms are responsible for reading the FROG trace and iteratively converging on the correct electric field. In general, this is carried out in a series of steps:

1. Start with the electric field as a function of time $E(t)$ (this will be a guess at the very beginning of the algorithm).

2. Generate the signal as a function of time and delay $E_{sig}(t, \tau)$.

3. Fourier transform it to be a function of delay and frequency $E_{sig}(\omega, \tau)$.

4. Modify the function to be in better agreement with the observed signal, $E'_{sig}(\omega, \tau)$.

5. Inverse Fourier transform the signal; it is now a function of time and delay, $E'_{sig}(t, \tau)$.

6. Generate an electric field as a function of time $E(t)$.

This process is repeated until the function of delay and frequency is a sufficient match for the observed spectrogram [Tre00].

There are many techniques for achieving the fourth step, but the basic algorithm maintains the phase of the signal, and changes the amplitude to correspond to the retrieved FROG signal $I_{FROG}(\omega, \tau)$ [Tre00],

$$E'_{sig}(\omega,\tau) = \frac{E_{sig}(\omega,\tau)}{|E_{sig}(\omega,\tau)|}\sqrt{I_{FROG}(\omega,\tau)} \tag{3.24}$$

The sixth step is carried out by simply integrating the delay parameter. By this means a complete characterization of the electric field in amplitude and phase is reconstructed, with a known uncertainty, in principle.

There are other geometries for FROG, such as polarization gating (PG) third harmonic (TH) and self diffraction (SD) [TDF+97]. The advantage of SH-FROG over other geometries is that it is more sensitive and easier to assemble. Disadvantages include a less intuitive trace, and one remaining ambiguity in pulse characterization. A SH-FROG cannot by itself lift time reversal ambiguity. This is not a large problem for most applications. The ambiguity can be lifted by placing a piece of glass before the input to the FROG. In this case, an internally reflected copy of the pulse will lag the main pulse and the ambiguity will disappear. A systematic study of the noise sensitivity of FROG can be found in [FDTL95].

It is possible to go further. One can achieve full characterization of the electric field, and simultaneously measure the frequency gradient and pulse-front tilt of a laser pulse with a device known by the acronym GRENOUILLE (GRating-Eliminated No-nonsense Observation of Ultrafast Incident Laser Light E-fields). This technique was introduced by O'Shea et al. [OKGT01] in 2001.

The design of the GRENOUILLE is such that its output traces are nearly identical to SH-FROG with most of the advantages and disadvantages of that technique, except that the apparatus is considerably simplified as shown in figure 3.16, which is adapted from Trebino's text [Tre00].

When using SH-FROG, two copies of a beam must be precisely overlapped into a tiny volume within a nonlinear crystal. This volume must be small in the transverse axis to ensure that the produced second harmonic

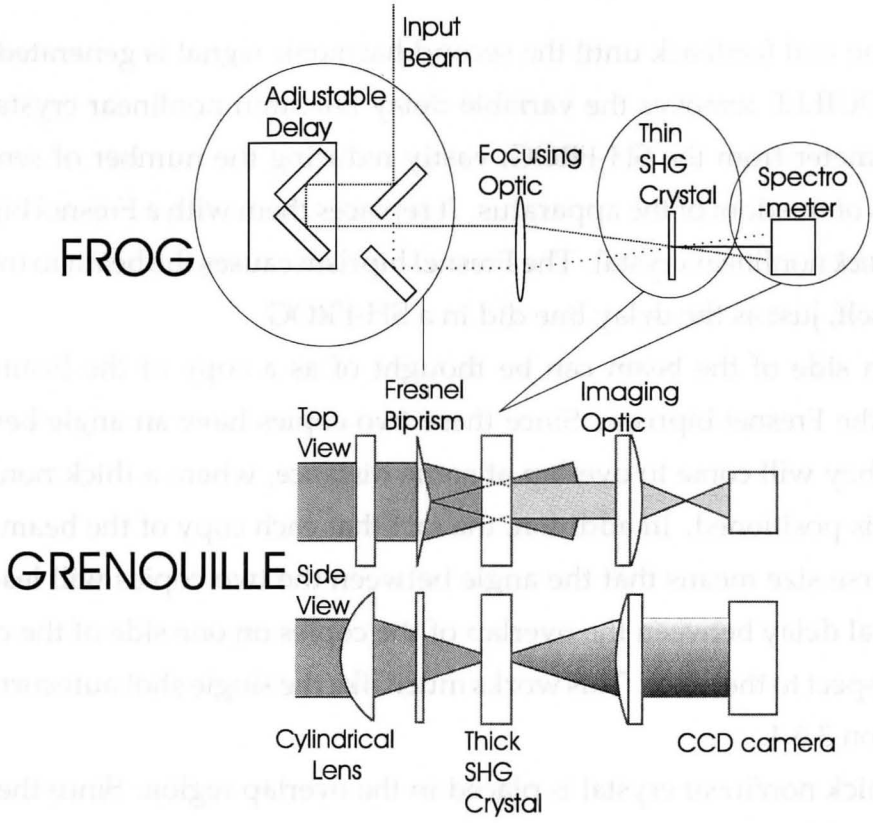

Figure 3.16: Schematic of FROG and GRENOUILLE setups. Much of the FROG apparatus is simplified in GRENOUILLE.

light is an accurate representation of the entire beam (so that the second harmonic light is created from a spatially homogenous source), and the volume must be small longitudinally to allow for the broad bandwidth of femtosecond pulses (see section 2.9.1). In order for second harmonic light to be generated in the crystal, the crystal must also be positioned at the correct angle and the two copies of the pulse must be overlapping in time.

Not only do the pulses need to overlap in space for a given time delay, but this position in space must remain constant as the time delay is varied. Since this time delay is usually generated by translating mirrors through space, those mirrors and the axis of translation must be precisely aligned. There

is also no real feedback until the second harmonic signal is generated. The GRENOUILLE removes the variable delay line, thin nonlinear crystal and spectrometer from the SH-FROG, vastly reducing the number of sensitive degrees of freedom of the apparatus. It replaces them with a Fresnel biprism and a *thick* nonlinear crystal. The Fresnel biprism causes the beam to overlap with itself, just as the delay line did in a SH-FROG.

Each side of the beam can be thought of as a copy of the beam as it leaves the Fresnel biprism. Since these two copies have an angle between them, they will come to overlap at some distance, where a thick nonlinear crystal is positioned. In addition, the fact that each copy of the beam has a transverse size means that the angle between the two copies will lead to a temporal delay between the overlap of the copies on one side of the crystal with respect to the other. This works much like the single shot autocorrelator in section 3.6.4.

A thick nonlinear crystal is placed in the overlap region. Since the thick nonlinear crystal will generate different frequencies of second harmonic light (within the bandwidth allowed) in different directions, it will act as a spectrometer. If the crystal is oriented so that the angle between the different generated frequencies is orthogonal to the angle between the two copies of the beam, the result is that the delays can be resolved in one axis and the spectrum can be resolved in the other axis. Using some cylindrical lenses, the generated light can be projected onto a CCD camera, and the result is an image identical to what would have been generated using a classical scanning SH-FROG. This data is generated using GRENOUILLE in a single-shot. Another advantage of the GRENOUILLE is its sensitivity to frequency gradient [AGZT04] and pulse-front tilt [AKOT03a].

Since the GRENOUILLE does not mix two exact copies of a beam, but rather mixes the right half with the left, it is not symmetric with respect to inversion. This means that if there is a time delay in the peak of the pulse

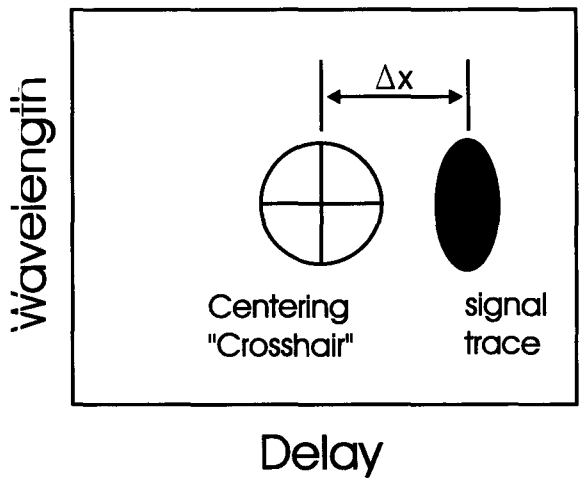

Figure 3.17: Schematic of the effect of frequency gradient as it appears in the signal trace using GRENOUILLE. PFT is related to the signal shift Δx by equation 3.25.

that varies with respect to the transverse position (which is the case for pulse front tilt), there will be a time delay between the two copies of the pulse that are overlapped in the nonlinear crystal. This is measured as a shift of the entire image in the delay axis of the CCD; refer to figure 3.17. The quantity of shift is related to the PFT by

$$PFT = \frac{\Delta x}{cL} \tag{3.25}$$

where L is the distance between the biprism and the nonlinear crystal.

Furthermore, if the pulse is spatially dispersed (so that the left is more blue than the right side of the pulse, for instance), the resulting CCD image will contain shear (the central delay will vary as a function of wavelength). The shear occurs because different transverse sections of the pulse are transformed into different delays by the Fresnel biprism, and the thick nonlinear crystal resolves the frequency components of each delay. So if the peak of the spectrum of the pulse varies with transverse position (as it does with

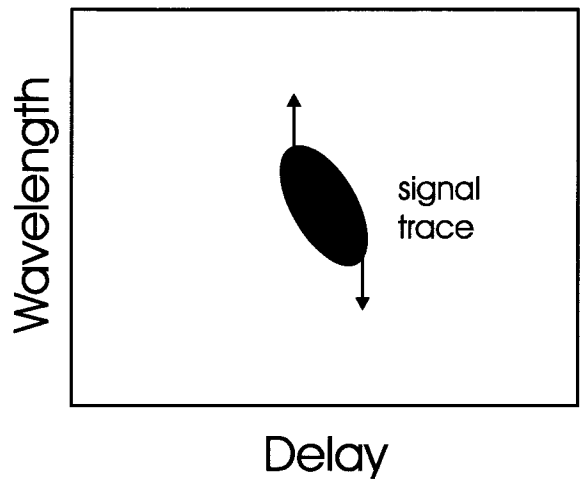

Figure 3.18: Schematic of the effect of frequency gradient as it appears in the signal trace using GRENOUILLE. The degree of frequency gradient is determined by the degree of shear in the trace (how much the central delay varies as a function of wavelength).

spatial dispersion), the position of the peak intensity on the CCD camera for each wavelength component will vary as a linear function of the delay; refer to figure 3.18.

The pulse-front tilt and spatial dispersion can thus be extracted from the retrieved trace. These effects can then be corrected for, and a standard SH-FROG pulse retrieval algorithm can be applied to the trace, resulting in the electric field amplitude and phase.

GRENOUILLE is versatile, but has its limitations. As O'Shea et al. describe in [OAKT04], a given device has only a limited range of frequencies, bandwidths and pulse durations with which it can be used. The GRENOUILLE used in this work was a Swamp Optics model 8-20, designed for use with amplifier or oscillator pulses, at 800 nm with durations from 20 fs - 200 fs. An example of GRENOUILLE output data can be found in figure 3.19.

Gabolde et al. also demonstrate FROG can be combined with digital holography to recover the full electric field $E(x, y, t)$ amplitude and

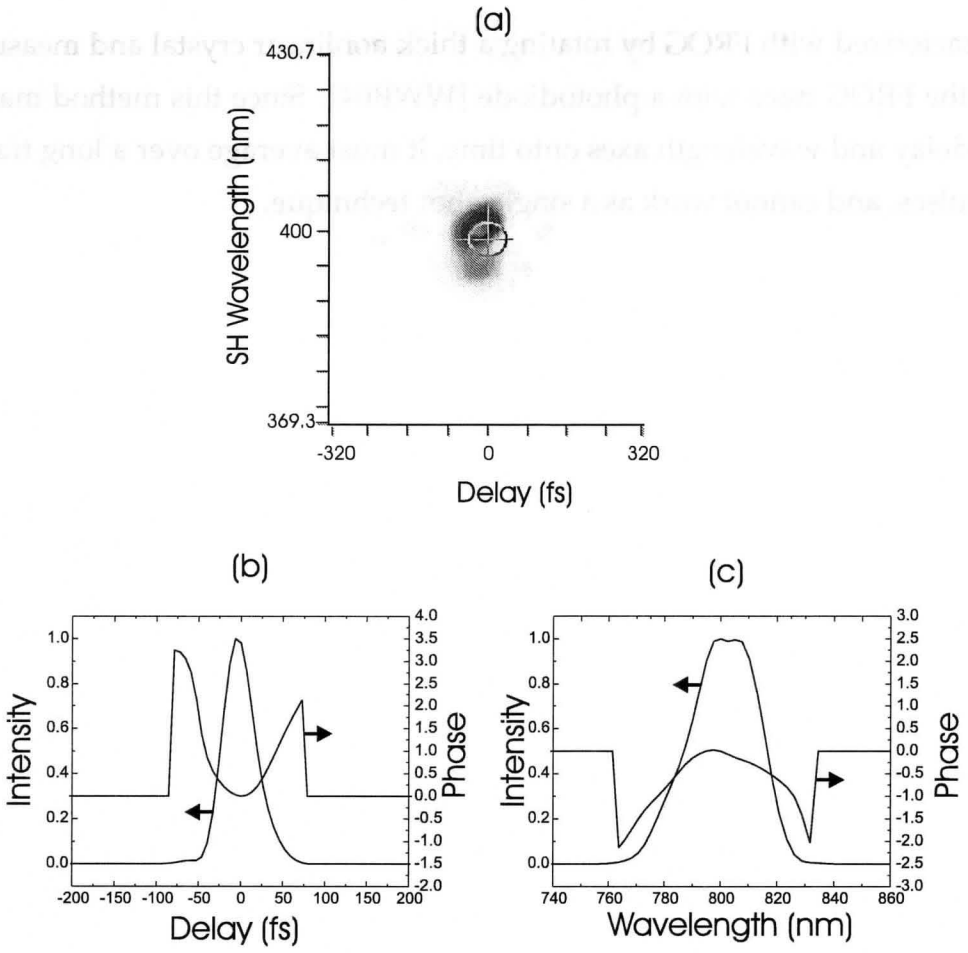

Figure 3.19: Example GRENOUILLE output from Femtosoft Quick-FROG. (a) Measured GRENOUILLE trace. (b) Software retrieved temporal intensity and phase. (c) Software retrieved spectral intensity and phase. Pulse duration is calculated to be 44 fs FWHM, with a bandwidth of 29 nm FWHM.

phase [GT04]. This goes even further than the GRENOUILLE in terms of pulse characterization. The field is recovered with a resolution of 50 μm $\times$ 50 μm $\times$ 4 nm (spatial $\times$ spatial $\times$ spectral). This technique unfortunately must average over a train of pulses although Gabolde et al. suggest a single shot version is possible, with the cost of lower spatial resolution. Wasilewski et al. also demonstrate that very weak pulses can be effectively

characterized with FROG by rotating a thick nonlinear crystal and measuring the FROG trace with a photodiode [WWR04]. Since this method maps the delay and wavelength axes onto time, it must average over a long train of pulses, and cannot work as a single-shot technique.

3.8 Spectral Interferometry and SPIDER

Though some of the methods discussed above are able to measure the amplitude, phase, and even some spatio-temporal distortions of a laser pulse, they are all nonlinear. It is desirable to have access to a technique which responds in a linear fashion to an input signal. This is because such a technique will be much more sensitive. Unfortunately it is not possible to extract information about an unknown pulse from a linear method [LCJ95]. If the interference of two different pulses is measured however, the resulting signal will depend on the phase difference between these two pulses. This suggests a measurement technique known as Spectral Interferometry (SI). In SI, a known pulse is superimposed with an unknown pulse, and the resulting interference pattern contains enough information to reconstruct the amplitude and phase of the unknown pulse. The only requirement placed on the known pulse is that it contain all the frequency components contained in the unknown pulse. The following is a summary of Lepetit, Chériaux and Joffre's discussion of SI, which can be found in [LCJ95].

SI can occur in the both the time and frequency domains, by scanning either the frequency or delay interval. In order to perform SI in the time domain, interference oscillations are very rapid, and a great deal of data must be recorded to resolve them. These limitations can be overcome, and temporal interferometry is promising for infrared pulses [LCJ95].

A simpler solution is frequency domain SI. The pulses are overlapped in a spectrometer, and a CCD captures the whole signal at once. Hence it is possible to use this technique in single-shot mode, analyzing each pulse separately. The signal in the frequency domain is given by

$$S(\omega) = |E_0(\omega)|^2 + |E(\omega)|^2 + 2Re\left[E_0^*(\omega)\, E(\omega)\right] \tag{3.26}$$

where $S(\omega)$ is the power spectrum as a function of angular frequency, and E

and E_0 are the fields due to the reference and unknown pulses respectively, and *Re* means the real part.

The cross term in equation 3.26 is proportional to the cosine of the phase difference between the two functions, so if the phase of the reference is known, the phase of the unknown pulse can in principle be extracted. There are technical challenges with this extraction, as signal to noise becomes small at the extremum of the cosine, and there is an ambiguity of in the retrieved phase between θ and $2\pi - \theta$.

One solution is to multiplex the signal, by using a circularly polarized reference pulse and a circularly polarized unknown pulse, and two spectrometers. This provides signals that vary as sine and cosine function; this technique is named Dual Quadrature SI (DQSI).

A simpler solution experimentally is Fourier transform SI (FTSI). In this technique the reference pulse is precedes the unknown pulse in time by a known delay τ. The reference pulse behaves like a pump and the unknown pulse like a probe. The pump causes an excitation that is felt by the probe, and spectral interference results. The time integrated interference term is then given by

$$S(\omega) = E_0^*(\omega) E(\omega) \exp(\imath\omega\tau) + c.c. \tag{3.27}$$

The inverse Fourier transform of this signal will have two terms, one corresponding to each complex conjugate in equation 3.27.

For a sufficiently large choice of τ, the terms do not overlap. Since the $-\tau$ pulse in the time domain is non causal, it can be filtered out with a Heaviside step function $H(t)$. A Fourier transform of the filtered signal will correspond to the amplitude and phase of the product $E_0^*(\omega) E(\omega)$.

Hence the unknown pulse amplitude and phase is given by

$$E(\omega) = \frac{F\left[H(t)\,F^{-1}S(\omega)\right]\exp(-\imath\omega\tau)}{E_0^*(\omega)} \tag{3.28}$$

The SI setup and data recovery is sketched in figure 3.20.

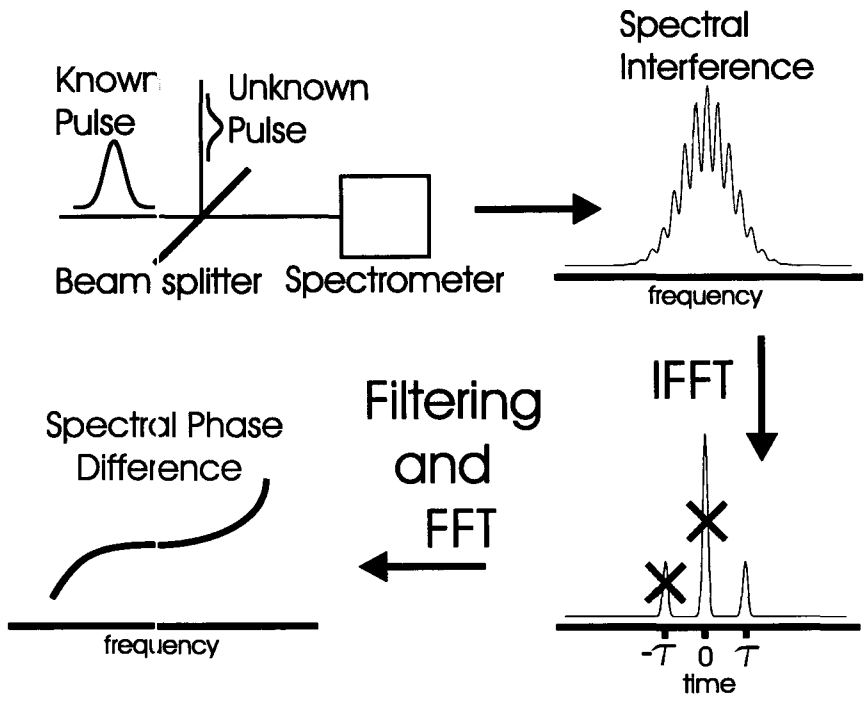

Figure 3.20: Schematic diagram of spectral interferometry. Known and unknown pulses are overlapped, and their spectral interference pattern is inverse Fourier transformed. The result is filtered (zero and negative delay peaks removed), and Fourier transformed, resulting in their phase difference.

SI is ideal for characterizing very weak pulses, when combined with the FROG techniques described above (see section 3.7) to characterize the reference pulse. This combination is called temporal analysis by dispersing a pair of light E fields (TADPOLE). It can be used to measure a train of pulses with an average energy as weak as 42×10^{-21}J [FBS+96].

If no reference pulse is available, one can still make use of Spectral

Interferometry (SI) to fully characterize the amplitude and phase of a pulse, the cost being that the method becomes nonlinear in intensity. The technique is called spectral phase interferometry for direct electric-field reconstruction (SPIDER). The technique is similar to standard Fourier transform SI (FTSI), except that two copies of the *same* pulse are injected into a spectrometer. Since SI is sensitive only to phase differences, the two copies of the unknown pulse are frequency shifted by different (and known) amounts. This is the nonlinear part. After some analysis of the resulting spectrum, the full amplitude and phase of the unknown pulse can be reconstructed. Iaconis and Walmsley go though this in detail in [IW98] and [IW99]; their arguments are summarized here.

The interference of two frequency shifted copies of the pulse $S(\omega)$ is given by

$$S(\omega) = 2\left|E(\omega)\,E(\omega+\Omega)\right|\cos\left[\Phi(\omega+\Omega)-\Phi(\omega)+\omega\tau\right] \tag{3.29}$$

where E is the field of the unknown pulse, ω is the angular frequency, and Ω and τ are the relative frequency and temporal shifts between the two copies of the pulse, and Φ is the spectral phase of the pulse. This interference term contains enough information to recover the phase of the unknown pulse (to within a constant term). Its amplitude is recovered by taking the square root of the power spectrum. If the duration of the pulse to be measured is T_0, then a relative spectral shift of $2\pi/T_0$ is sufficient to reconstruct the phase completely.

A frequency shift between the two copies of the unknown pulse is generated by superimposing the two copies, separated in time by τ, with another, highly temporally dispersed pulse (usually another copy of the unknown pulse itself), inside a nonlinear medium (see figure 3.21). The third pulse must be sufficiently dispersed so that for the duration of each of the two copies of the unknown pulse, it is essentially monochromatic. Since the

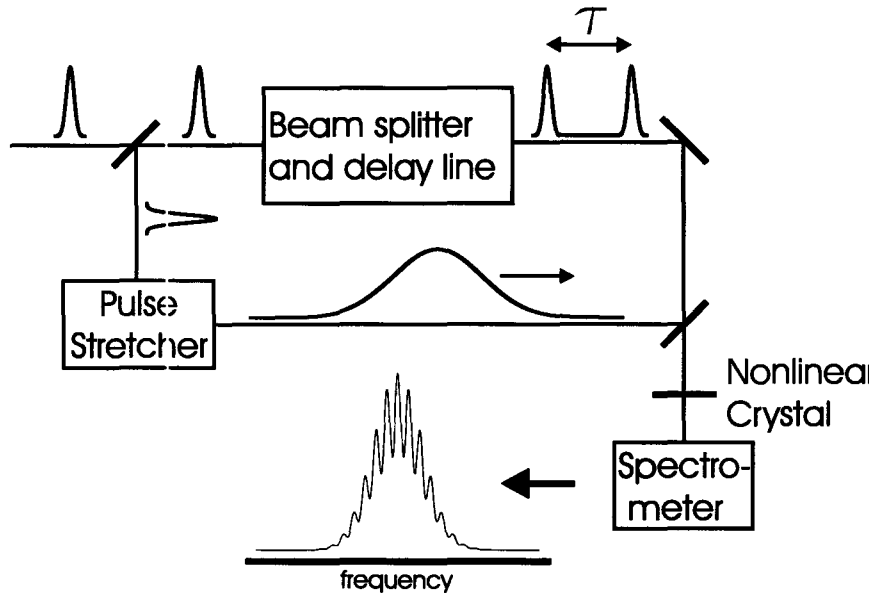

Figure 3.21: Schematic diagram of spectral phase interferometry for direct electric field reconstruction (SPIDER). A beam splitter creates two copies of the unknown pulse. One copy is stretched in a dispersive material or grating based stretcher. The other copy is split again, and a delay τ is introduced between its copies. These three pulses are overlapped in a nonlinear crystal, and the second harmonic signal is observed with a spectrometer. Data analysis is similar to standard FTSI.

first two copies of the pulse are separated in time, and the third pulse has a spectrum that is a function of time, each of the first two copies experiences a different frequency shift inside the nonlinear medium. The amount of dispersion in the third pulse and the delay between the first two pulses must simply be large enough to ensure a sufficient frequency shift between them.

The spectral phase is extracted from the interference term in a method similar to FTSI. The data is inverse Fourier transformed, the positive τ peak is kept and the rest of the signal is discarded. This signal is then Fourier transformed, and the linear phase term $\omega\tau$ is subtracted. The phase of the unknown pulse can then be extracted from the remaining signal, the phase

difference, with a resolution equal to Ω the spectral shear.

The accuracy of all SI methods is affected by the calibration of the spectrometer used. Careful calibration can eliminate systematic error due to the spectrometer and yield high accuracy [Dor99].

It is also possible to extend the SPIDER technique to measure spatio-temporal distortions. By using a two dimensional array CCD detector instead of a one dimensional array, the spectral phase can be resolved as a function of one spatial dimension [DKW02]. This reveals the full complex coupling between frequency and position, and can be used to measure pulse front tilt and spatial dispersion, as well as higher order couplings.

Chapter 4

Femtosecond Laser Pulse Diagnostics

4.1 Measurements With a Spectrally-Resolved Knife-Edge

It is difficult to measure the angular dispersion of a beam directly, especially for small values of angular dispersion in large beams [PKW00, SMD01]. Consider extending the knife-edge and photodiode beam profiler detailed in section 3.5. If a spectrometer is used in place of a photodiode, it should be possible to conduct several knife-edge experiments in parallel, one for each wavelength bin. By collecting these spectrally-resolved knife-edge (SRKE) measurements for a number of different longitudinal positions in the beam, it is possible obtain a direct measurement of the angular dispersion present in the beam.

A number of instruments, such as the GRENOUILLE (see section 3.7) and TFPA (see section 3.6.5) measure pulse-front tilt, which is caused by angular dispersion. A direct measurement of angular dispersion is a useful independent measurement though, since measuring pulse front tilt is not equivalent to measuring angular dispersion. This is because it is possible to create pulse front tilt in the absence of angular dispersion [AGZT04]

(see section 3.2). The method described in this section leads to a direct reconstruction of the angular and spatial dispersion of a beam.

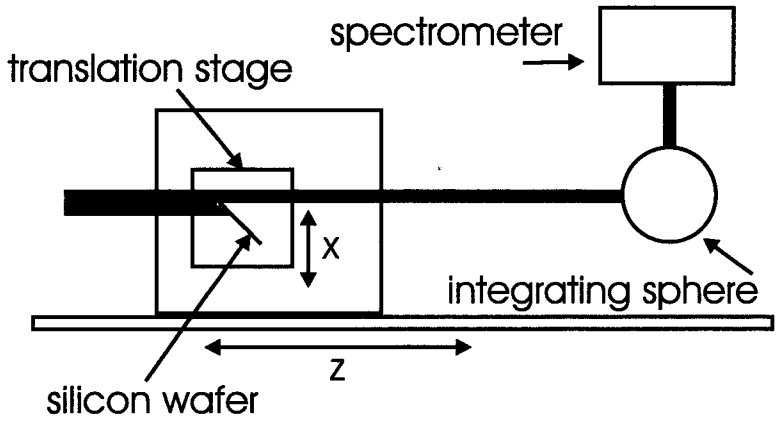

Figure 4.1: The apparatus for direct measurement of angular dispersion.

In order to collect SRKE data, the apparatus sketched in figure 4.1 was constructed. The device works in a similar fashion to a regular knife-edge beam profiler in which a sharp blade is scanned in the transverse direction across the beam (see section 3.5). The difference is that a spectrometer and an integrating sphere are used instead of a photodiode. The spectrometer must have a linear CCD array or some other means to allow the whole spectrum to be imaged simultaneously. This is essential, as a scanning spectrometer would impose a cost in time that would make this measurement impractical. The spectrometer used in this study was an Ocean Optics USB2000. Laser light with angular dispersion has by definition a spectrum that varies with transverse position. In order to ensure that a representative sample of the entire laser spectrum is coupled into the spectrometer, an integrating sphere is employed. Light is coupled into an input aperture of the sphere, where it must bounce off the highly diffusive inner walls of the sphere, before being collected at the output, where it will be approximately spatially uniform.

The "knife" used in the scanning is the cleaved edge of a Si wafer, which

was very smooth and straight. Si is a good absorber of 800 nm light, and can be made very thin. It was used at a 45° angle to the laser axis to accentuate the sharpness of the cleaved edge. It was hoped that this would minimize unwanted diffraction effects. The knife was mounted on a Oriel DC encoder mike actuator, which can take controlled steps as small as 1 μm.

The data that is used to reconstruct the angular dispersion consists of scans at multiple positions along the axis of propagation. The stage with the knife-edge is translated along the axis of propagation manually, but could in principle be automated. For each position along the axis of propagation, the knife is scanned using a computer controlled translation stage. It takes small steps, typically 10 μm at a time. This step size was chosen deliberately to be quite small, to facilitate noise and error analysis. The spectrometer collects a beam spectrum for each of these steps. The result is a very large amount of data: spectral intensity resolved as a function of transverse and longitudinal position. This information can be reduced in such a way as to yield the spatial and angular dispersion β of the beam.

In order to reduce the data, it is first assembled into a large array $I^*(z, x^*, \lambda)$, where I^* is the raw spectral intensity, z is the longitudinal position, x^* is the raw transverse position and λ is wavelength. This data must be filtered before it can be processed. To eliminate alignment error in the x coordinate, the integral

$$\Lambda(x^*, z) = \int I^*(z, x^*, \lambda)\, d\lambda \tag{4.1}$$

is computed. The centroids $x_0^*(z)$ of Λ

$$x_0^*(z) = ErfFit_{x^*}[\Lambda(x^*, z)] \tag{4.2}$$

are then computed. $ErfFit_{x^*}$ represents centroid results from an error function fitting routine (this implicitly assumes a Gaussian beam profile). These

fits are exactly the same as fits required when computing the beam properties in standard knife-edge profiling 3.5. Algorithms for calculating error function, Gaussian and linear fits can be found in numerical methods textbooks (see for example, reference [PTVF02]). The resulting centroids are subtracted from the raw positions yielding the corrected transverse position $x(z,\lambda) = x^*(z,\lambda) - x_0^*(z)$.

Two important related quantities are now computed, the transverse centroids $x_0(z,\lambda)$ and the spectral centroids $\lambda_0(z,x)$. The transverse centroids are calculated first:

$$x_0(z,\lambda) = ErfFit_x\left[I(z,x,\lambda)\right] \tag{4.3}$$

The results of the error fitting on the intensity data are centroids x_0, widths and amplitudes, for each value of z and λ. To reduce the effects of noise on frequency gradient calculations, new intensity data is constructed. The transverse centroids, widths and amplitudes are used to construct a Gaussian function for each z and λ. This results in a new intensity function $I_g(z,x,\lambda)$. Spectral centroids are then calculated from this new data:

$$\lambda_0(z,x) = GausFit_\lambda\left[I_g(z,x,\lambda)\right] \tag{4.4}$$

where $GausFit_\lambda$ represents centroid results from a Gaussian fitting routine with respect to wavelength (which assumes a Gaussian shaped spectrum). The Gaussian fitting routine was much more stable when used to extract spectral centroids from $I_g(z,x,\lambda)$ than directly from $I(z,x,\lambda)$, and resulted in more consistent frequency gradient data.

An example of raw transverse centroid data obtained from a beam having traversed a BK7 prism can be found in figure 4.2. Here is depicted the results of Gaussian fits for three particular wavelength bins. The light was collected between 782-784 nm, between 800-802 nm and between 816-818 nm. The

centre of these wavelength bins is plotted against longitudinal position. There is noise in this data, the source of which is most likely random. This is supported by the fact that the noise is greater for the wavelength bins in the wings of the spectrum where intensity is low than for the bins in the centre where intensity is high. The slopes of these lines correspond to the angle each wavelength bin makes with respect to the average direction of the entire beam.

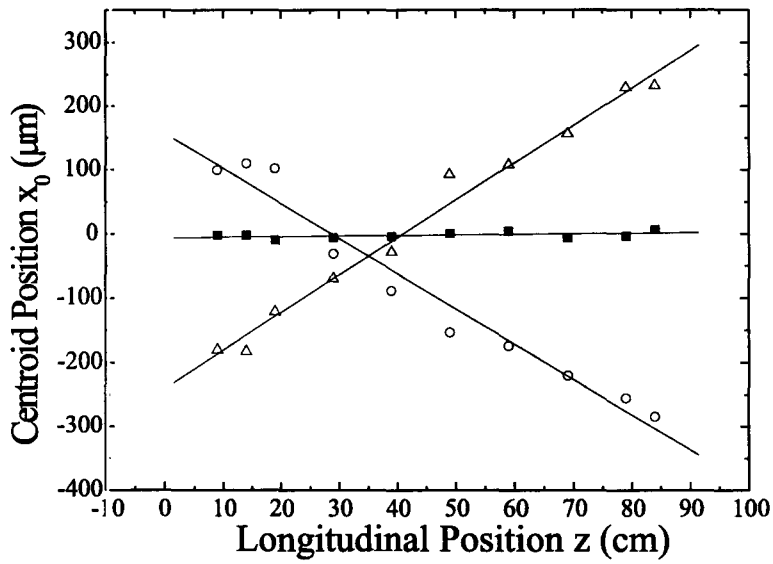

Figure 4.2: Centroid positions versus longitudinal position for laser beam after traversing a 60° BK7 prism (induced PFT = 29 fs/mm). Squares: 800 nm, circles: 782 nm, triangles: 818 nm. At 42 cm the spatial dispersion induced by the prism cancels the spatial dispersion initially present in the beam, leading to nearly zero spatial dispersion.

The remaining analysis is straightforward. The spatial dispersion ζ and frequency gradient ν can then be computed as

$$\zeta(z) = \frac{\partial x_0}{\partial \omega} = \frac{-\lambda^2}{2\pi c}\frac{\partial x_0}{\partial \lambda} = \frac{-\lambda^2}{2\pi c} Lin_\lambda [x_0(z,\lambda)] \tag{4.5}$$

$$v(z) = \frac{\partial \omega_0}{\partial x} = \frac{-2\pi c}{\lambda^2}\frac{\partial \lambda_0}{\partial x} = \frac{-2\pi c}{\lambda^2} Lin_x [\lambda_0 (z, x)] \tag{4.6}$$

where Lin_λ and Lin_x are the slopes of linear fits with respect to λ and x.

Spatial dispersion and frequency gradient are thus evaluated for each value of z sampled. Spatial dispersion is given by [AGZT04]

$$\zeta(z) = \beta z + \zeta(0) \tag{4.7}$$

which implies that angular dispersion β is simply calculated by taking the slope of $\zeta(z)$. To calculate β, another linear regression is performed

$$\beta = Lin_z [\zeta(z)] \tag{4.8}$$

It is also possible to calculate the angle of propagation of each wavelength

$$\theta(\lambda) = Lin_z [x_0 (z, \lambda)] \tag{4.9}$$

This presents a second way to calculate angular dispersion

$$\beta = Lin_\lambda [\theta(\lambda)] \tag{4.10}$$

Equations 4.8 and 4.10 should yield equivalent values for β analytically. With actual discretely sampled data however, the statistics of these two methods will be different. This is because the resolution in each parameter (z, x and λ) is different.

The device described above records enough data to measure spatial dispersion and frequency gradient, and also angular dispersion in two different ways. Since it records both frequency gradient and spatial dispersion, it can be used to verify the relationship between them given by equation 2.59, developed by Gu et al. [GAT04]. Equation 2.59 can be rewritten as

$$a = \frac{b}{b^2 + \kappa^2} \rightarrow \kappa = \sqrt{b/a - b^2} \tag{4.11}$$

where

$$a = \frac{\partial \lambda_0}{\partial x} = \frac{-\lambda^2}{2\pi c}\nu \tag{4.12}$$

$$b = \frac{\partial x_0}{\partial \lambda} = \frac{-2\pi c}{\lambda^2}\zeta \tag{4.13}$$

and

$$\kappa = \frac{\pi c w T_0}{\lambda^2} = \frac{w}{\Delta\lambda} \tag{4.14}$$

for Fourier transform limited Gaussian pulses. Here a and b represent dimensionless versions of frequency gradient and spatial dispersion, respectively. A κ parameter can be calculated for each longitudinal point using equation 4.11, and compared with the value of κ that would be expected based on the measured values of bandwidth and beam width, using equation 4.14.

Direct measurements were made for three configurations of prisms. For maximum angular dispersion, a single equilateral SF10 prism, near the angle of minimum deviation was used resulting in an angular dispersion of ~93 μrad/nm. Less angular dispersion was achieved using a single equilateral BK7 prism with an angular dispersion of ~29 μrad/nm. A small amount of angular dispersion was generated using a combination of two prisms, aligned to *mostly* cancel each other's angular dispersion, the remainder of which was ~6 μrad/nm. The Spitfire output was used for a minimal value of angular dispersion of ~0.8 μrad/nm. Results are found in figures 4.3, 4.4 and summarized in table 4.1. The theoretical values found in table 4.1 were calculated using the mathematics of section 3.2, and measurements of the

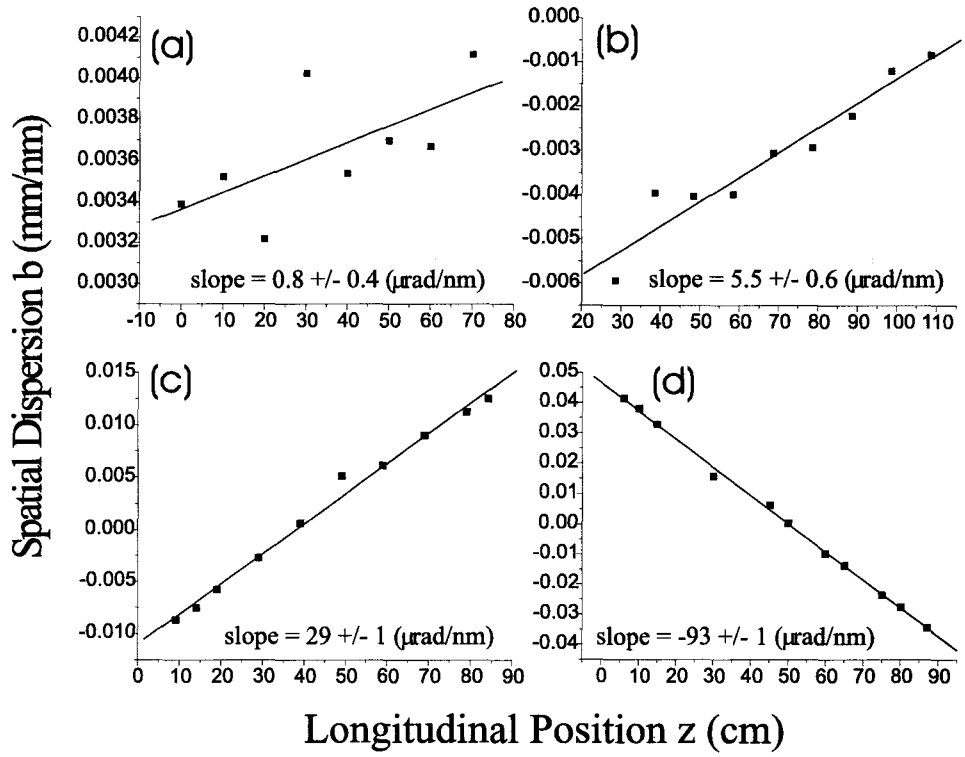

Figure 4.3: Spatial dispersion versus distance from (a) no prism (z has arbitrary origin), (b) 2 opposed SF10 prisms, (c) a single BK7 prism and (d) a single SF10 prism. The value of spatial dispersion at $z = 0$ was not controlled between a-d (the distance between the amplifier and the prism(s) was not fixed). Note also the difference in the vertical scale between the plots.

prism orientations.

The first thing to note is the consistency between the results in figures 4.3 and 4.4. These two figures are plots of the same data, reduced in different ways. The first uses $\frac{dx_0}{d\lambda}(z)$ as an intermediate step, the second uses $\theta(\lambda)$. The fact that they are consistent is a check on the algorithm used to extract the results from the raw data. The data in both plots seems to be well modeled by a straight line, another fact supporting the algorithm. It can be seen that as the amount of angular dispersion is reduced, noise becomes apparent, as one would expect (see for instance the "No Prisms" case, where noise is

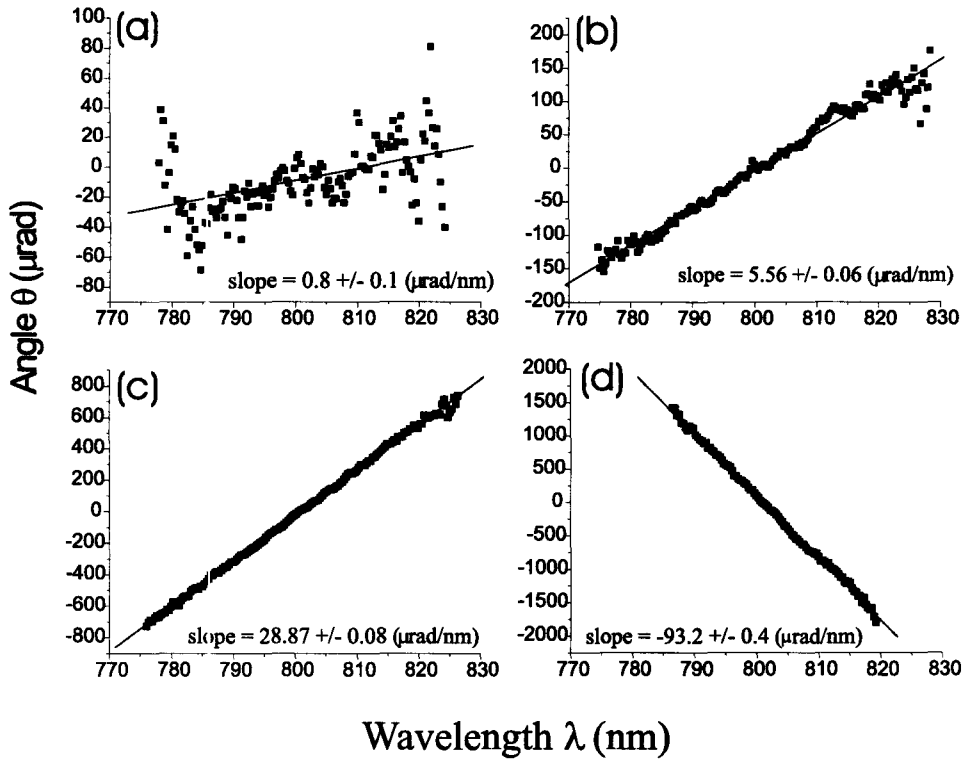

Figure 4.4: Propagation angle versus wavelength for (a) no prism, (b) 2 opposed SF10 prisms, (c) a single BK7 prism and (d) a single SF10 prism. Note the difference in the vertical scale between the plots.

large compared to the slope). Note that in figures 4.3, 4.4 and 4.5 the SF10 prism case has the opposite slope to the other cases. This is simply due to the prism having the opposite orientation to the BK7 prism in this case. In the case of no prism, and two opposite prisms, the residual angular dispersion happened to be the same sign as the BK7 prism case.

The difference between the two figures can be understood as a difference in the method of data reduction. The data in figure 4.3 leaves the linear regression in longitudinal position last, and the data in figure 4.4 leaves the regression in wavelength last. There are a much larger number of wavelength bins than longitudinal position bins. The result is that the uncertainty

Prism Material	Angle of incidence (rad)	n	$dn/d\lambda$ 10^{-5} nm^{-1}	$d\Theta/d\lambda$ calculated $\mu rad/\ nm$	$d\Theta/d\lambda$ measured $\mu rad/nm$
output beam	n/a	n/a	n/a	n/a	0.8 ± 0.1
2 SF10 comb.	1.05, 1.11	1.7113	-5.0	7 ± 4	5.56 ± 0.06
Single BK7	0.89	1.5106	-2.0	30 ± 2	28.87 ± 0.08
Single SF10	1.08	1.7113	-5.0	90 ± 4	93.2 ± 0.4

Table 4.1: Calculated and measured angular dispersion values for three equilateral prism configurations. Approximate laser characteristics: $\lambda = 800$ nm, $\Delta\lambda \sim 25$ nm. The beam radius was ~3 mm.

on the angular dispersion linear fit is significantly less when calculated with equation 4.10. Note that the fit uncertainty is significantly less in figure 4.4 than it is in figure 4.3. It is also worth noting that the fit uncertainty reported using the $\theta(\lambda)$ technique is always less than or equal to 0.4 μrad/nm, and tends toward lower values for smaller values of angular dispersion.

Hypothetically, as the intensity of light reaching the spectrometer is increased, the signal to noise ratio should also increase, improving the statistics of the data, and resulting in a more precise measurement of angular dispersion. In the current study, the position of the integrating sphere and the spectrometer were simply adjusted to maximize the intensity of light reaching the spectrometer. A systematic study of the relationship between light intensity and uncertainty would be useful.

The maximum angular dispersion uncertainty of 0.4 μrad/nm compares favorably with the uncertainty of the device developed by Varjú and coworkers [VKKO02]. Their spectrally-resolved interferometric device measures angular dispersion with an uncertainty of 0.2 μrad/nm (in the range of 0.2 - 40 μrad/nm). This device has the advantage of measuring the angular dispersion at a point, rather than over some finite range, as the SRKE does, and also that it works in real time. While the SRKE must scan in two dimensions, which has required between 30 minutes and 4 hours (depending on

the precision required), it has the advantage over the interferometric device of being very simple to set up and operate. The SRKE diagnostic also gives access to the spatial dispersion and frequency gradient of the beam, as a function of propagation, which may be important for some applications.

Long collection times limit SRKE's effectiveness as a routine diagnostic, as it must be assumed that the laser is producing stable output over this timescale. It also limits the usefulness of this technique for "tweaking" optical components. For a diagnostic to be successful, its feedback cycle must be short. A comprehensive error analysis of this technique could identify the optimal amount of data required for robust measurements, and significantly reduce the amount of time this diagnostic takes to run. If for instance only 50 lateral points and 4 longitudinal points are needed, motion in the lateral and longitudinal dimensions is controlled by faster computerized translation stages, and light is more efficiently coupled into the spectrometer, similar results to those presented here may be achieved in as little as 5 minutes. Also, faster performance may be possible if uncertainty limits are relaxed.

Since several fitting algorithms are used, and only relative differences in data are used to generate the final reports, the device should have very little systematic error. This point is further supported by the good agreement between theoretically predicted dispersion values and measured ones. The only systematic errors that the algorithm is sensitive to are systematic relative errors in increments in the spatial coordinates, and in the spectrometer. The spectrometer has been calibrated with known wavelengths, and should be accurate to less than 1 nm. The systematic relative error in the longitudinal step sizes should also be small. These are limited by an experimenter's ability to manually translate the stage along a rail to marked points on a ruler. Errors in these steps are likely very small compared with their size. Also, errors in increment cannot compound, because all steps on the ruler

have already been marked. Systematic error in the transverse steps should also be small, as the accuracy of the Oriel actuator is much less than the step sizes used. The actuator can reproduce steps to within about 1 μm accuracy. Also, as in the case of longitudinal motion, the actuator is set to step to a position, and not to step for a given distance, reducing the propagation of systematic error.

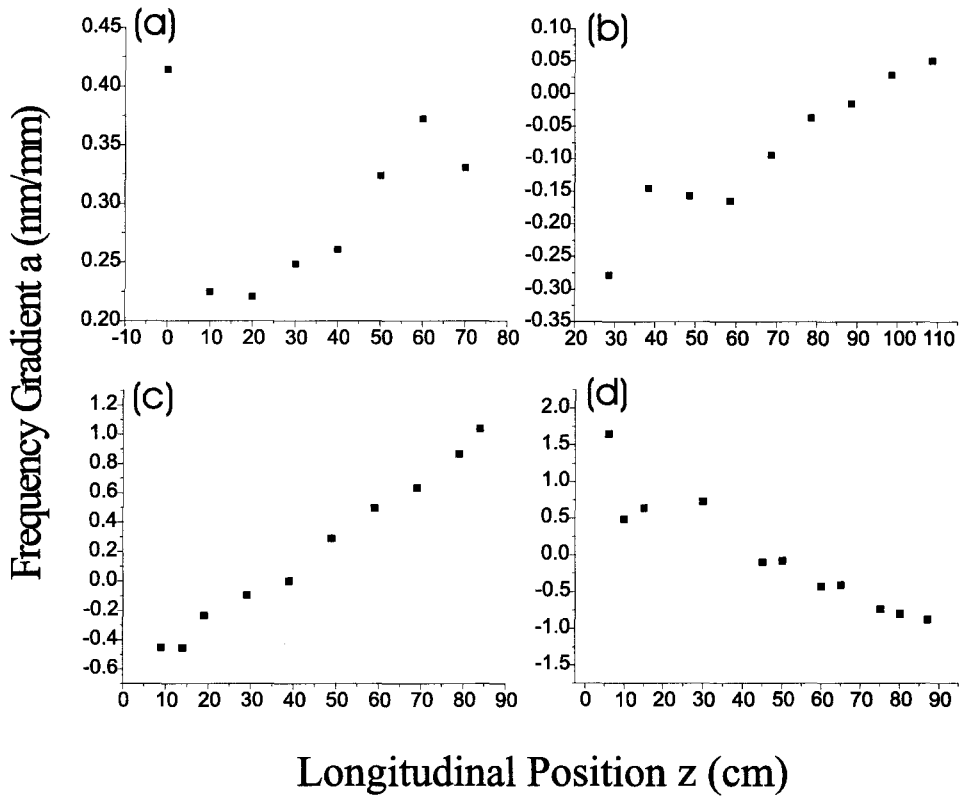

Figure 4.5: Frequency Gradient versus distance from (a) no prism, (b) 2 opposed SF10 prisms, (c) a single BK7 prism and (d) a single SF10 prism. The value of spatial dispersion at $z = 0$ was not controlled between a-d (the distance between the amplifier and the prism(s) was not fixed). Note also the difference in the vertical scale between the plots.

The response function of the spectrometer as a function of wavelength is unknown, but should not impact measurements of angular dispersion.

The calculation of $\theta(\lambda)$ is independent of spectral response of the spectrometer, as its calculation only compares data of equivalent wavelengths. This means that angular dispersion calculations are also independent of spectral response.

The SRKE also measures spatial dispersion and frequency gradient; see figures 4.3 and 4.5. The frequency gradient measurement will depend on the quality of the grating in the spectrometer. The frequency gradient is calculated based on Gaussian fits of the spectrum at various transverse points in the beam. The spectral centroids returned by the Gaussian fits can in principle be in error if there is a non-constant spectral response, although this is not expected to pose a large problem here.

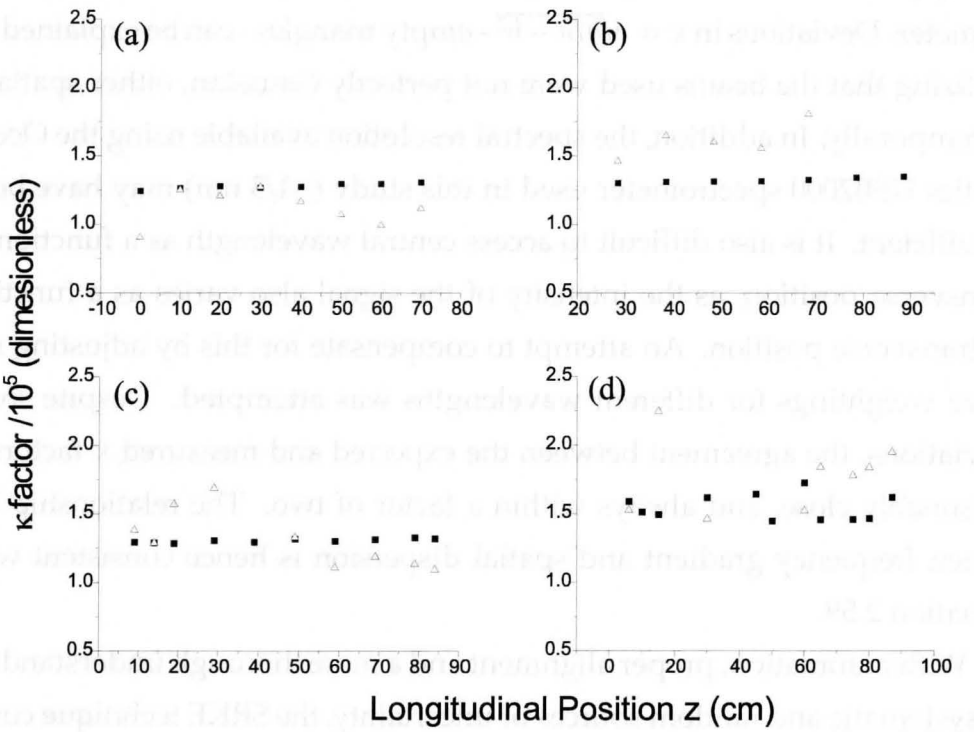

Figure 4.6: Self consistency factor κ factor versus longitudinal position for (a) no prism, (b) 2 opposed SF10 prisms, (c) a single BK7 prism and (d) a single SF10 prism. Shaded squares: $\kappa = w/\Delta\lambda$, open triangles: $\kappa = \sqrt{b/a - b^2}$.

Nonetheless, there is a discrepancy between measured and expected values of the κ factor in equation 4.14. The lateral width and spectral bandwidth of the beam at each value of z were measured, and their ratio ($\kappa = w/\Delta\lambda$) was plotted in figure 4.6, with the value of κ measured from frequency gradient and spatial dispersion ($\kappa = \sqrt{b/a - b^2}$). The κ value corresponding to a 3.5 mm (FWHM) wide beam, with a bandwidth of 25 nm is 1.4×10^5. In principle, each point in each plot in figure 4.6 should be close to 1.4×10^5.

Deviations from this number in the case of the ratio of width and bandwidth ($\kappa = w/\Delta\lambda$ - solid squares) are likely symptoms of random error in fitting procedures. This is possibly due to a low signal reaching the spectrometer. Deviations in $\kappa = \sqrt{b/a - b^2}$ - empty triangles - can be explained by realizing that the beams used were not perfectly Gaussian, either spatially or temporally. In addition, the spectral resolution available using the Ocean Optics USB2000 spectrometer used in this study (~1/3 nm) may have been insufficient. It is also difficult to access central wavelength as a function of transverse position, as the intensity of the signal also varies as a function of transverse position. An attempt to compensate for this by adjusting relative weightings for different wavelengths was attempted. Despite some deviations, the agreement between the expected and measured κ factors is reasonably close, and always within a factor of two. The relationship between frequency gradient and spatial dispersion is hence consistent with equation 2.59.

With automation, proper alignment and a more thorough understanding of systematic and random sources of uncertainty, the SRKE technique could be made reasonably compact, accurate and fast. The main advantage of the SRKE is that it is simple, and its measure of angular dispersion is robust to systematic error. It is thus an ideal independent check on other more sophisticated measures of spatial dispersion and angular dispersion (such

as the GRENOUILLE).

The SRKE defined in this section is a fairly sensitive technique. The measurement taken used pulses of roughly 5 μJ, at a repetition rate of 1 kHz. This corresponds to an average power of about 5 mW. There seems to be a direct trade-off between the speed of acquisition, the uncertainty of the measurement, and its sensitivity. In principle, the technique could work with even less input power, though the uncertainty of the results depends on the input power. Even less power could be used if the integration time on the spectrometer was increased, though this would slow the diagnostic.

The sensitivity could also be improved by removing the integrating sphere, or replacing it with a more efficient version. The removal of the sphere could lead to systematic error, which would have to be investigated. Preliminary investigations do show a systematic shift in the measurements without an integrating sphere (presumably because of the non-spectrally-uniform coupling into the spectrometer), but it is possible this challenge could be overcome.

4.2 Pulse Front Tilt Effects On Autocorrelation

Focused ultrafast laser pulses are useful as they provide the greatest possible electric field intensities and very precise delivery of optical power. Unfortunately, the physics of focused laser pulses is complicated. Clearly, the shape and thus the intensity of the focus will depend on the spatial profile of the input pulse. These effects are in general quite complex, as the paraxial approximation must be abandoned for high numerical aperture lenses. Other effects will also lead to distortions in the focus. The material properties of lenses (see section 3.3), and the temporal shape [HOB94] and polarization [DQL03] of the initial pulse will all influence the spatial and temporal profiles of the pulse in the vicinity of the focus.

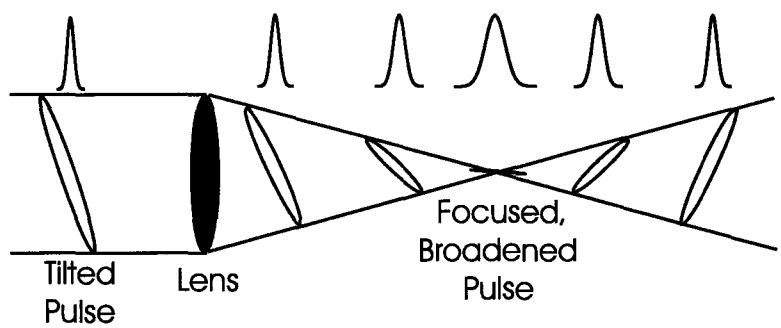

Figure 4.7: A somewhat oversimplified but intuitive depiction of a tilted pulse moving through a focus. Note that the sign of PFT changes after the focus.

This section will deal with the effect spatio-temporal distortions have on the pulse duration near the vicinity of the focus. The focus is an interesting place to study the effects of pulse-front-tilt (PFT) due to angular dispersion [PKW00] as it is in the focus that the effects of PFT on pulse duration can be most easily observed. Outside of the focus, PFT will induce a delay effect, but this delay will be distributed across the pulse.

In the absence of focussing optics, the pulse duration at a specific trans-

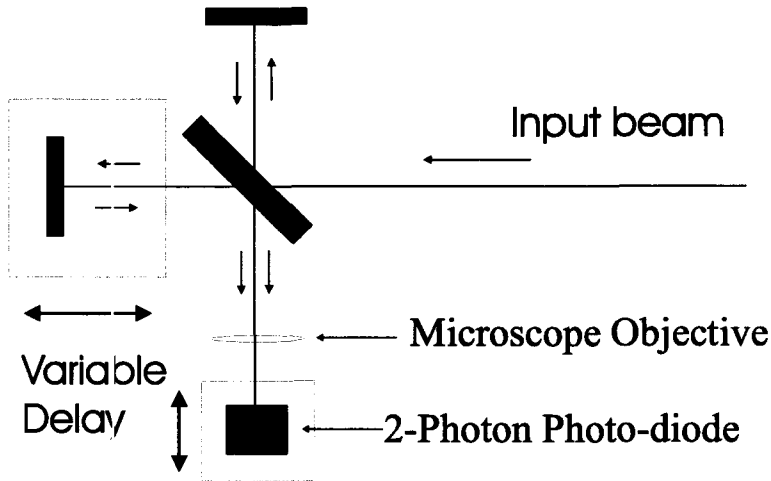

Figure 4.8: Setup for the 2-photon diode interferometric autocorrelator.

verse position will increase due to the negative GDD caused by the spatial dispersion caused by the prism (see section 3.2, equation 3.3 for more details), but this GDD can be compensated at a given point. Spatial dispersion will also reduce the local bandwidth as the beam propagates, but this will happen slowly for large beams (see section 2.10, equation 2.69 for details on this effect).

As the beam is focused, the delay between the transverse edges of the pulse remains the same but the edges are brought closer together. Each local transverse position will gradually be affected by the global delay across the beam. When the focus is reached, the full delay will be experienced by each local transverse position. The ratio ξ of the duration of the pulse in the focus T_0' and the initial duration of the pulse T_0 was developed in section 2.10

$$\xi = \frac{T_0'}{T_0} = \sqrt{1 + \left(\frac{PFTw}{T_0}\right)^2} \tag{4.15}$$

where PFT is pulse front tilt. Thus if autocorrelation is performed on an entire beam, and at several points through a focus, the effect of PFT can be

measured.

In order to verify this relationship, the apparatus sketched in figure 4.8 was assembled. A standard interferometric autocorrelator was modified by placing a 5× microscope objective at the output. A Thorlabs GaP or Hamamatsu GaAsP photodiode was placed near the focus of a 5× Newport microscope objective. Initially the GaAsP diode was used with the SF10 prism. The GaP diode was then used with a single BK7 prism, with no prisms, and with two opposed BK7 prisms. The GaP diode became available after the initial work with the SF10 prism and GaAsP diode. It was used thereafter as it was more conveniently packaged. The GaAsP photodiode was specified to vary in sensitivity by ~17% over the SHG bandwidth of ~12 nm, the GaP photodiode was specified to vary by less than 10% over the same range.

The bandgap of both these photodiodes is sufficiently large so that a single 800 nm photon lacks the energy to excite an electron into the conduction band, and generate a current signal. Two photons can provide sufficient energy however, so both photodiodes respond proportionally to the square of the laser intensity. A photodiode with a quadratic intensity response was chosen over a nonlinear crystal to be certain that phase matching over the bandwidth of the laser pulse would not be a problem (see section 2.9.1).

The power transmitted to the autocorrelator setup was varied using a half-wave-plate and two thin-film polarizers. The photodiode was mounted on a computerized translation stage, which allowed it to be translated longitudinally through the focus of the microscope objective. As the detector was moved through the focus, the spot size at the detector changed, and the power transmitted through the wave-plate-polarizer combination was adjusted to provide sufficient signal without saturating the detector. Angular dispersion was introduced into the output of the Spitfire laser system through dispersing prisms (see figure 4.9). Interferometric auto-

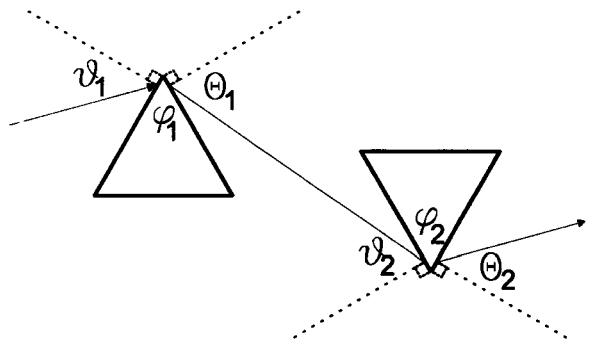

Figure 4.9: Angular dispersion is generated with one or two prisms. Two prisms are shown here, though the geometry for one is the same. In the case of two identical prisms ($\varphi_1 = \varphi_2$), $\vartheta_1 \neq \Theta_2$ leads to angular dispersion.

correlation traces were then collected, similar to those performed by Juodkazis et al. [JOK+04]. The compressor within the amplifier was adjusted to optimize for minimum pulse duration at the autocorrelator, correcting linear GDD caused by the prism. Traces were collected as a function of position with respect to the focus for four different prism configurations.

In situations where a large amount of angular dispersion was introduced, the effects were obvious: a large amount of "chirp", and a broadening of the temporal profile occurred as can be seen in figure 4.10. The intrinsic pulse duration here is ~60 fs, which would be observed in an autocorrelation without a focus. It is increased to ~175 fs in the focus, because of the presence of 58 fs/mm PFT.

Pulse durations were extracted from the interferometric traces by averaging the autocorrelation signal over one oscillation, to extract the DC term in the interferometric autocorrelation (see equation 3.19 in section 3.6.1). The FWHM of the DC term is calculated by fitting to a Gaussian function. This process is sketched in figure 4.11. A deconvolution factor of $\sqrt{2} \sim 1.4$ was then applied to extract the pulse intensity duration FWHM. This deconvolution factor corresponds to the assumption that the pulse has a Gaussian

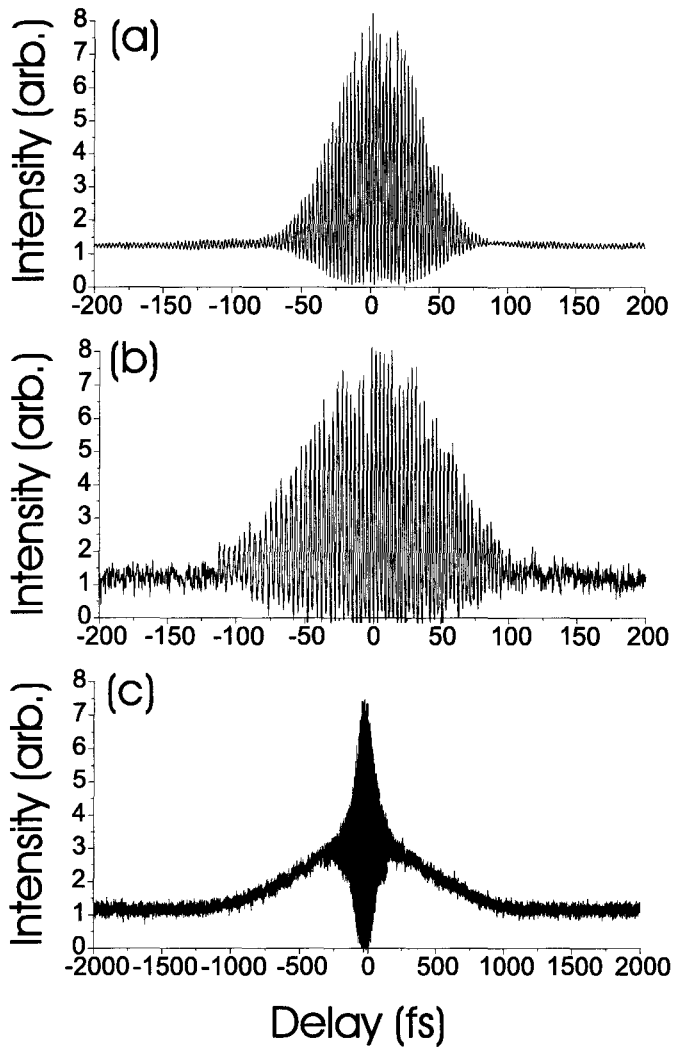

Figure 4.10: Autocorrelation traces of pulses without focusing or angular dispersion (a), with angular dispersion but without focusing (b) and with angular dispersion and focusing (c). A microscope objective is used to focus the autocorrelation output beam onto a 2-photon photodiode. The beam in the lower two cases contains ~210 fs/mm PFT, generated by traversing a single SF10 prism, near its angle of minimum deviation. Note the different scales on the horizonal axes. The small increase in duration in the second case is likely due to a combination of uncompensated material dispersion in the prism, and spatial dispersion GDD induced by the prism.

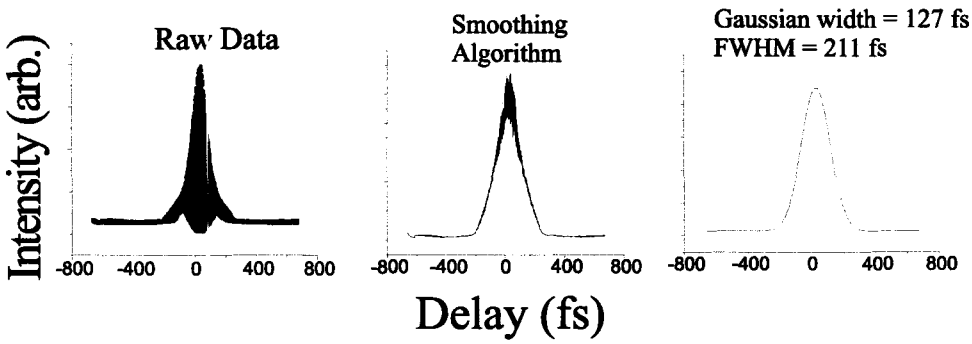

Figure 4.11: Example of procedure used to extract pulse durations from interferometric autocorrelations. Raw data is averaged over one optical cycle to extract slowly varying intensity autocorrelation signal. A Gaussian fit is then performed on the smoothed data. The data in this case was taken with BK7 prism, in the focus of the 5× microscope objective.

temporal profile.

Figure 4.12 depicts a number of AC traces centred at the focus of the 5× objective (f = 2.54 cm) for the case of angular dispersion generated with the BK7 prism. It can be seen that as the focus is approached, the pulse duration increases, in a way that appears the same as the effect produced by pure temporal dispersion (i.e. indistinguishable from the effect sketched in figure 3.9). Away from the focus, the dispersion effect is diminished, and the pulse duration approaches its nominal value.

The experimental results for four different prism configuration are summarized in figure 4.13. Pulse duration as measured using the procedure outlined in figure 4.11 is plotted against position in μm from the focus of the microscope objective. These plots behave qualitatively the way one would expect based on the analysis of Pretzler et al. [PKW00]. The duration is maximized at the focus, and diminishes for the larger spot sizes away from the focus. Quantitatively, the increased pulse duration effect in the focus is reasonably well modeled by equation 4.15. The maximum pulse duration increase is considered, and $\xi = T_0'/T_0$ is calculated for each configuration.

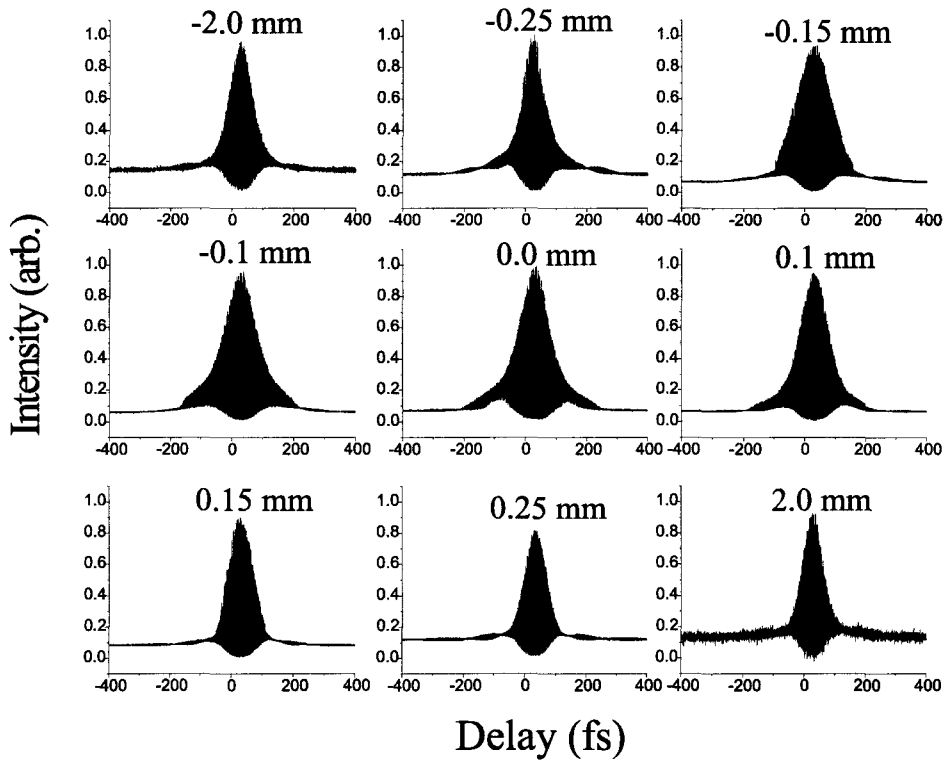

Figure 4.12: Example of 2-photon autocorrelation traces. Taken with a BK7 prism at several distances from the focal point of the microscope objective.

Prism Setup	Base Duration	Max Duration	Measured PFT (fs/mm)	Predicted ξ	Measured ξ
none	51	58	5	1.1	1.1
2 BK7	66	82	22	1.5	1.2
1 BK7	64	175	58	3.6	2.7
1 SF10	87*	760	210**	8.9	8.7

Table 4.2: Measured and predicted ξ for various configurations of prisms. * Intrinsic duration is measured with standard autocorrelation without focussing, not with GRENOUILLE. ** *PFT* is calculated, not measured with GRENOUILLE.

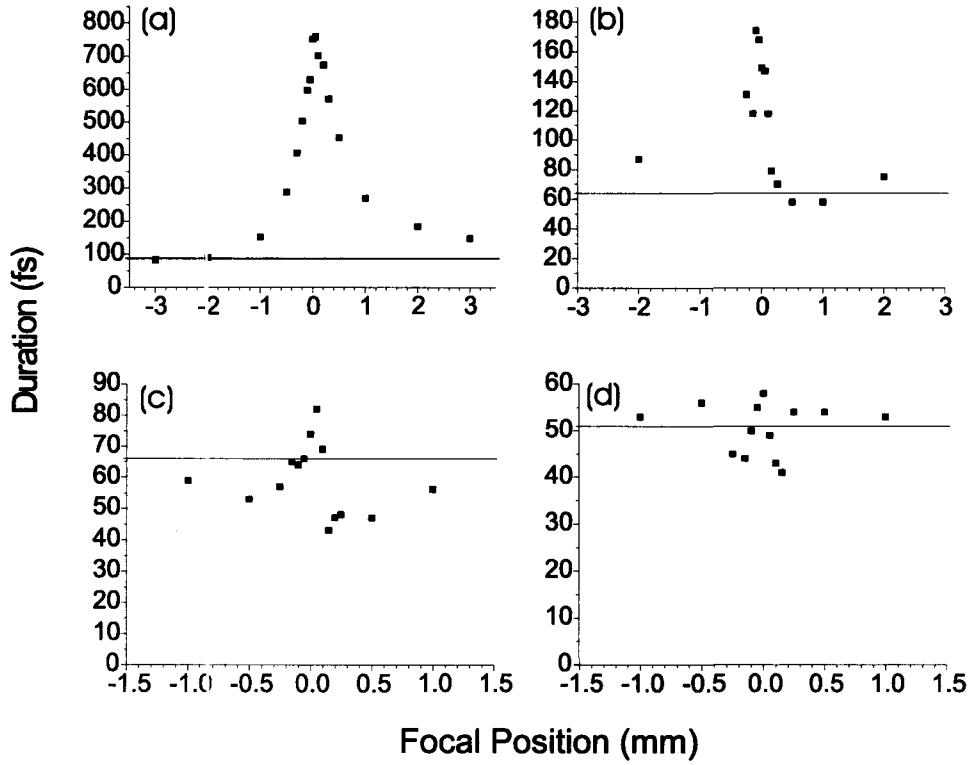

Figure 4.13: Results of 2-photon diode interferometric autocorrelator experiment. Pulse duration as a function of distance from focus for (a) 210 fs/mm, (b) 58 fs/mm, (c) 22 fs/mm and (d) 5 fs/mm. Solid line indicates measurement of the pulse duration using GRENOUILLE in all cases except in the case of the SF10 prism, where standard autocorrelation (without a focus at the autocorrelator output) was used. PFT was measured with GRENOUILLE, except in the case of SF10, where it was calculated. The "dip" below baseline duration is ~5 - 10 fs in b-d.

This is compared to the effect that would be predicted from equation 4.15, using values of *PFT* measured with a GRENOUILLE, or calculated from theory. The input beam was measured to have an intensity $1/e^2$ radius w_0 of 3.0 mm. When focused with the 5× objective, this corresponds to a spot size of ~2.1 μm and a Rayleigh range of ~17 μm. In reality many factors can cause the spot size to be larger than the nominal value of ~2.1 μm, such as a beam $M^2 \neq 1$, or lens aberrations. A spot size of 5-6 μm [CBH+05a]

is often achieved in practice, when using the 5× microscope objective. The increased pulse duration effects are summarized in table 4.2.

In order to be more quantitative about the results of this experiment, a theoretical model must be developed. In order to make progress in this direction, the model developed by Kostenbauder [Kos90] was employed. This model uses ray-pulse matrices similar to the standard ABCD ray matrices to trace rays through an optical system. It goes beyond the standard treatment by considering the time delay and frequency of rays, as well as their position and direction. A ray is traced through the system using the matrix equation

$$\begin{pmatrix} x \\ \theta \\ t \\ f \end{pmatrix}_{out} = \begin{pmatrix} \frac{\partial x_{out}}{\partial x_{in}} & \frac{\partial x_{out}}{\partial \theta_{in}} & \frac{\partial x_{out}}{\partial t_{in}} & \frac{\partial x_{out}}{\partial f_{in}} \\ \frac{\partial \theta_{out}}{\partial x_{in}} & \frac{\partial \theta_{out}}{\partial \theta_{in}} & \frac{\partial \theta_{out}}{\partial t_{in}} & \frac{\partial \theta_{out}}{\partial f_{in}} \\ \frac{\partial t_{out}}{\partial x_{in}} & \frac{\partial t_{out}}{\partial \theta_{in}} & \frac{\partial t_{out}}{\partial t_{in}} & \frac{\partial t_{out}}{\partial f_{in}} \\ \frac{\partial f_{out}}{\partial x_{in}} & \frac{\partial f_{out}}{\partial \theta_{in}} & \frac{\partial f_{out}}{\partial t_{in}} & \frac{\partial f_{out}}{\partial f_{in}} \end{pmatrix} \begin{pmatrix} x \\ \theta \\ t \\ f \end{pmatrix}_{in} \tag{4.16}$$

where x, θ, t and f are the position, direction, delay and frequency shift of a ray with respect to a reference ray.

Several elements in the matrix of equation 4.16 simplify to either zero or one for time invariant linear systems, leading to a simpler matrix equation

$$\begin{pmatrix} x \\ \theta \\ t \\ f \end{pmatrix}_{out} = \begin{pmatrix} A & B & 0 & E \\ C & D & 0 & F \\ G & H & 1 & I \\ 0 & 0 & 0 & 1 \end{pmatrix} \begin{pmatrix} x \\ \theta \\ t \\ f \end{pmatrix}_{in} \tag{4.17}$$

Using equation 4.17 rays can be traced through an arbitrary linear, time-invariant optical system. As with standard ABCD matrices, the formalism can be extended to Gaussian beams. In the case of the Kostenbauder matrices, a generalized Gaussian function is constructed

$$U(x,t) = \exp\left[-\frac{i\pi}{\lambda_0}\begin{pmatrix} x_{in} \\ -t_{in} \end{pmatrix}^T Q_{in}^{-1}\begin{pmatrix} x_{in} \\ t_{in} \end{pmatrix}\right] \tag{4.18}$$

where Q is the matrix analogue of q in the standard ABCD approach. An output Q is determined from an input Q from the relation

$$Q_{out} = \left[\begin{pmatrix} A & 0 \\ G & 1 \end{pmatrix} Q_{in} + \begin{pmatrix} B & E/\lambda_0 \\ H & I/\lambda_0 \end{pmatrix}\right] \cdot \left[\begin{pmatrix} C & 0 \\ 0 & 0 \end{pmatrix} Q_{in} + \begin{pmatrix} D & F/\lambda_0 \\ 0 & 1 \end{pmatrix}\right]^{-1} \tag{4.19}$$

The above formalism covers laser pulses with Gaussian spatial and temporal profiles, and is valid within the paraxial approximation. It includes the effects of dispersion, and of first order spatio-temporal distortions, including pulse front tilt. It was used to model the effect of an optical system consisting of a prism followed by a lens (with free space after each). PFT is generated in the prism. When no PFT is desired, the prism is removed from the optical matrix. The theory assumes the lens is ideal, acting only to focus the pulse (no lens dispersion or distortions).

The duration over which the amplitude of the pulse has fallen by 1/e as a function of distance from the lens (located at z=0) is denoted $T(z)$ for pulses without PFT, and $T'(z)$ for pulses with PFT. These durations are meant to be interpreted as *local*. This is the duration that a very small detector, placed so it can only observe a small transverse slice of the beam, will measure.

Similarly $w(z)$ and $w'(z)$ represent 1/e amplitude widths. The focus of the beam occurs at $z = f$. Unless otherwise noted, a material dispersion ($dn/d\lambda$) of 20 $(mm)^{-1}$ is assumed for the prism. This value corresponds to the material dispersion of BK7 glass. The separation between the prism and the lens d is equal to zero unless otherwise noted. The beam is assumed to traverse the prism at the angle of minimum deviation (input angle = output angle), and the prism is assumed to be Brewster cut (minimal reflection

losses). These simplify the analysis considerably. The beam is assumed to propagate near the tip of the prism, so that the effect of material dispersion on the duration of the pulse is negligible. The waist of the beam is assumed to be at the prism input (or lens input, if prism is absent).

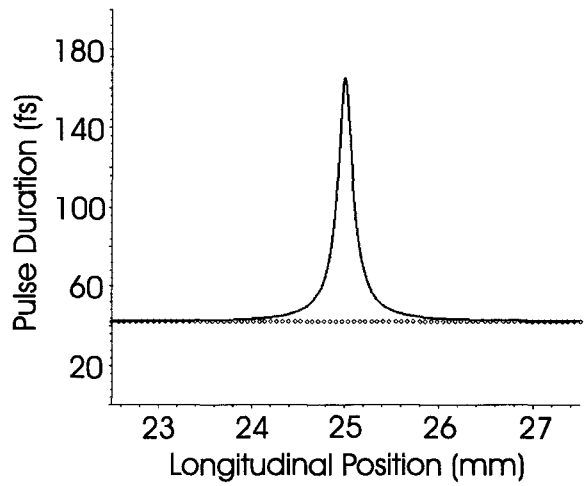

Figure 4.14: The theoretical local pulse duration as a function of distance from a $f = 25$ mm lens. The solid line refers to a pulse with 53.3 fs/mm PFT, the dotted line refers to a pulse without PFT.

Figure 4.14 depicts the effect of pulse front tilt due to angular dispersion induced by a BK7 prism on the duration of a focused laser pulse. The pulse duration increase in the focus is equal to the effect predicted by equation 4.15. Figure 4.15 depicts the spatial width (radius at which the amplitude decreases by a factor of 1/e) of the pulse in the transverse axis of the pulse containing the PFT. The width in the other axis will remain unaffected. The magnitude of the pulse duration increase here is the same as predicted by [PKW00]. Both the width and the duration are increased by the same factor ξ. This point is further underscored by figure 4.16. Figure 4.16 measures the effect on pulse duration and beam width, by computing the ratio of pulse duration ($T'(z)/T(z)$) and beam width ($w'(z)/w(z)$) for a tilted pulse

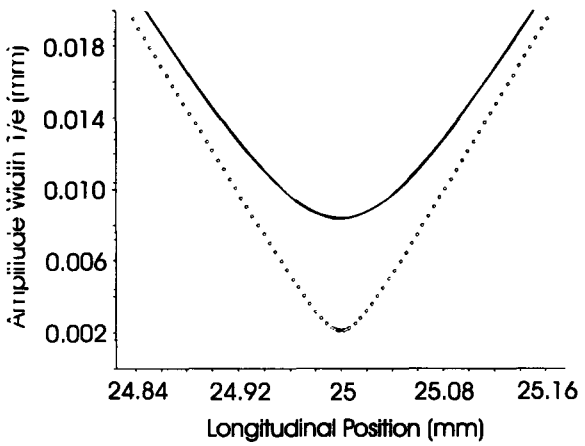

Figure 4.15: The theoretical beam width as a function of distance from a $f = 25$ mm lens. The solid line refers to a pulse with 53.3 fs/mm PFT, the dotted line refers to a pulse without PFT.

with the duration and width of an identical pulse without PFT. At the focus, the two effects are equal. While the beam width in the focus was not confirmed in this work experimentally, it is encouraging that the Kostenbauder model agrees with the behaviour predicted by Pretzler et al. [PKW00].

Figure 4.17 depicts the magnitude of the normalized pulse duration increase effect $(T'(z)-T(z))/(T'(f)-T(g))$ and the magnitude of the normalized focussing effect $(w'(z) - w(z))/(w'(f) - w(f))$ in order to get a sense of the longitudinal range of the duration increase effect. It seems that the pulse duration diminishes to $1/\sqrt{2}$ of its maximum value over approximately the same length as the width increases by $\sqrt{2}$ of its minimal value. This indicates that the duration increase is dependent upon the beam being focused. Indeed, it is found that the behaviour depicted in figure 4.17 is independent of focal length, provided there is a focus. The results of the Kostenbauder matrix formalism indicate that the range over which the pulse duration is increased in the focus is consistent with the range over which the beam width is decreased. The theoretically generated longitudinal range of pulse

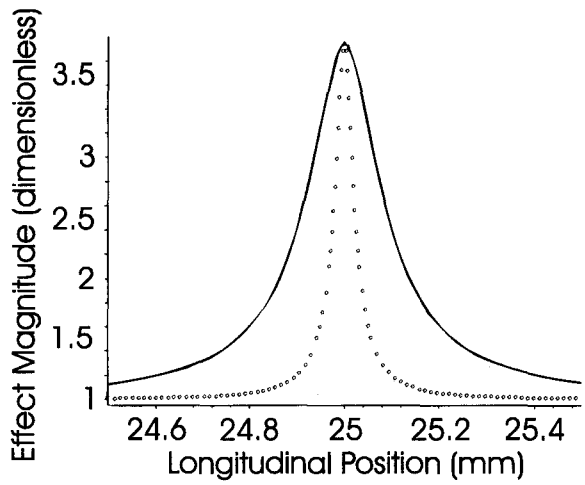

Figure 4.16: The tendency for pulse durations and beam widths to increase in the focus when 53.3 fs/mm PFT is present. The theoretical model results $T'(z)/T(z)$ (solid line) and $w'(z)/w(z)$ (dotted line) as a function of distance from a $f = 25$ mm lens. Notice that the magnitude of these effects is equivalent in the focus, verifying the work of Pretzler et al. [PKW00]

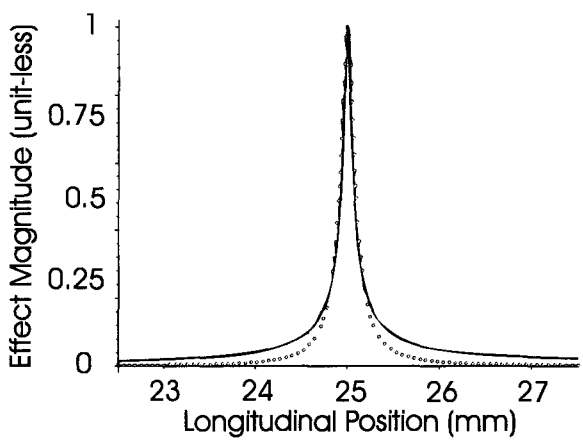

Figure 4.17: The degree to which the local pulse duration of a tilted pulse increases in the focus is consistent with the degree to which beam radius decreases. The theoretical model results $(w'(z) - w(z))/(w'(f) - w(f))$ (solid line) and $(T'(z) - T(z))/(T'(f) - T(f))$ (dotted line) as a function of distance from a $f = 25$ mm lens. Note that these effects have a very similar range.

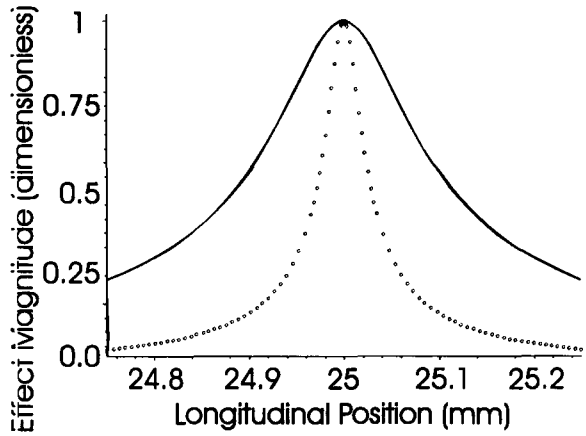

Figure 4.18: The range over which the beam is focused changes in the presence of PFT. The theoretical model results for a pulse with PFT = 53.3 fs/nm ($w'(f)/w'(z)$, solid line) and an untilted pulse ($w(f)/w(z)$, dotted line) as a function of distance from a f = 25 mm lens.

duration increase was found to be 70 μm. This is significantly larger than the calculated Rayleigh range of the un-tilted beam, which was ~20 μm, as depicted in figure 4.18.

It is difficult to precisely measure the range of the effects depicted in figure 4.13, but they appear somewhat larger than predicted by theory. The range over which the pulse duration is increased in the focus was found experimentally to be ~100 - 200 μm (~200 μm for the case in which the SF10 prism was used, ~100 μm for the case in which the BK7 prism was used), which is slightly larger than the Rayleigh range of 100 μm expected from a realistic spot size of ~5 μm [CBH05b], and also larger than the 70 μm predicted by theory. The theoretical value assumes a perfectly Gaussian shaped spatial profile however, and no optical aberrations. This is not the case experimentally, but it is difficult to incorporate these effects into the Kostenbauder formalism.

The above is roughly consistent with the work of Pretzler et al. [PKW00], whose longitudinal range of pulse duration increase was on the order of

100 μm. A spot size calculated based on their reported 2 cm Gaussian beam diameter, and 30 cm focusing optic result in a calculated spot size of ~4 μm, corresponding to a Rayleigh range (for the untilted pulse) of ~60 μm.

Spatial dispersion will also tend to increase the pulse duration. The GDD due to spatial dispersion will result in an increase in the pulse duration given by Osvay et al. [OKH+04] as

$$T = T_0 \sqrt{1 + \left[\frac{8 \ln 2}{\pi} \frac{L\lambda^3}{c^2} \frac{1}{T_0^2} \left(\frac{dn}{d\lambda} \right)^2 \right]} \tag{4.20}$$

where L is the distance traveled from the prism tip. This equation can also be found by inserting equation 3.3 into equation 2.41. This type of pulse duration increase will occur independent of any focusing, and will affect all parts of the beam equally.

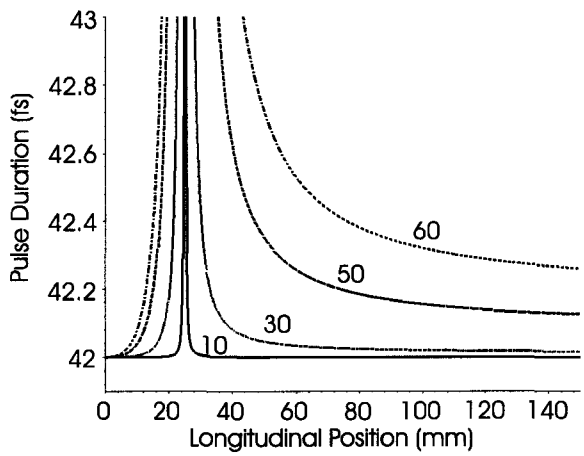

Figure 4.19: The theoretical pulse duration for several values of prism material dispersion ($\frac{dn}{d\lambda}$ = solid: 10, dot: 30, dash: 50, dot-dash: 60 mm^{-1}) as a function of distance from a $f = 25$ mm lens. The initial pulse duration is 42 fs in all cases. As the material dispersion of the prism is increased, a greater amount of spatial dispersion is generated over the length span of this figure, resulting in pulses broadened by GDD induced by spatial dispersion.

Figure 4.19 depicts the effect that spatial dispersion has on the duration

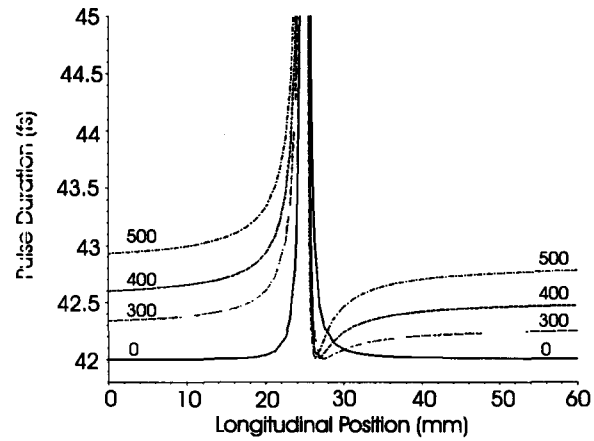

Figure 4.20: The theoretical pulse duration for several values of prism-lens separation (d = solid: 0, dot: 300, dash: 400, dot-dash: 500 mm) as a function of distance from a f = 25 mm lens. The PFT induced by the prism is 53.3 fs/mm, and the initial pulse duration is 42 fs.

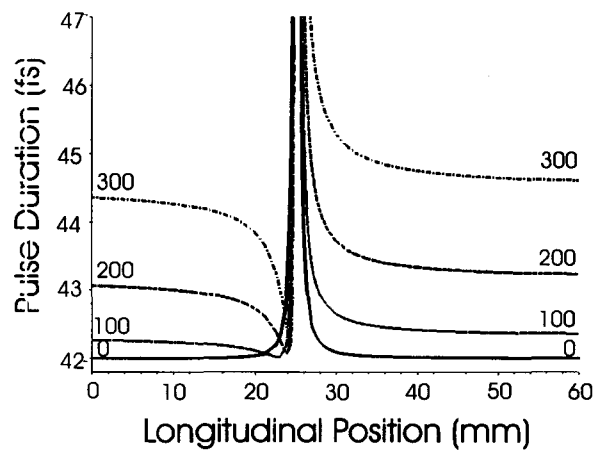

Figure 4.21: The theoretical pulse duration for several values of material dispersion in a slab placed before the prism-lens system (Φ_2 = solid: 0, dot: 100, dash: 200, dot-dash: 300 fs^2) as a function of distance from a f = 25 mm lens. The PFT induced by the prism is 53.3 fs/mm, and the initial pulse duration is 42 fs.

of the pulse. Note that the duration does not return to the initial value of 42 fs. This effect is always present, and its magnitude will depend upon the

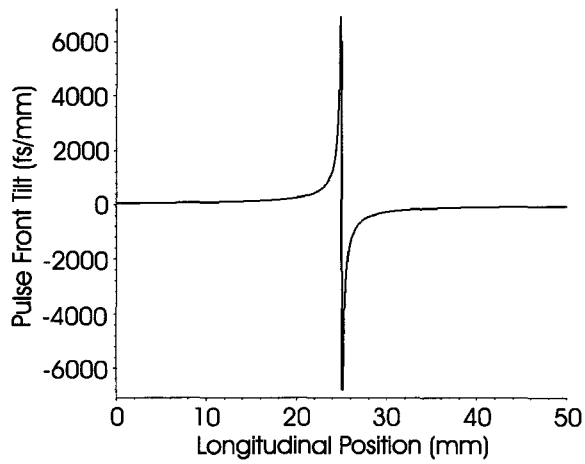

Figure 4.22: The theoretical model of 53.3 fs/mm pulse front tilt in the focus of a f = 25 mm lens.

amount of GDD picked up as a result of the spatial dispersion induced by the prism.

Another interesting and related effect is observed if there is enough spatial dispersion before the lens to induce a noticeable pulse duration increase. (The model used here generates this spatial dispersion by separating the lens and the prism). This effect is depicted in figure 4.20. In this case, at long distances, the spatial dispersion still causes the pulse duration to be increased above the initial value, but there is an now also an intermediate regime where the pulse duration "dips" temporarily to its initial value. If a dispersive slab is placed before the prism lens system, and the separation between the prism and the lens is returned to zero, the "dip" in pulse duration can be caused to move before the focus, as in figure 4.21. To the best of our knowledge, this is the first time such effects have been observed or discussed.

A possible explanation of the effects is as follows. The prism induces pulse front tilt and angular dispersion in the beam. Angular dispersion in turn generates spatial dispersion as the beam propagates through space. In

the absence of the initial slab introducing material dispersion, the spatial dispersion causes an increase in the pulse duration due to GDD. The sign of this GDD is negative. The pulse front tilt has no local effect on the duration of the pulse, in the absence of a focus. When the pulse reaches the lens, its phase front is modified. As it is focused by the lens, the pulse front tilt is increased, and as it reaches the focus the sign of the PFT is reversed. This effect is sketched in figure 4.22 where PFT is given by the elements of Q^{-1} as $\left(Q_{out}^{-1}\right)_{12} / \left(Q_{out}^{-1}\right)_{22}$ [AGZT04] (see also figure 4.7). Immediately after the focus the magnitude of PFT is large, but the sign is opposite to what it was originally, but the sign of the GDD due to spatial dispersion remains the same. If it is assumed that the increase in local pulse duration due to PFT near the focus is due to a kind of GDD, immediately after the focus, the sign of the GDD will change, as the sign of the PFT changes. As the magnitude of the PFT diminishes, it reaches a point where its GDD is equal to the magnitude of the spatial dispersion GDD. At this point the dispersion caused by each effect is equal and opposite, so they cancel, and the duration of the pulse returns to it initial value (42 fs in the above examples). In the case of an initial dispersive slab, the sign of the GDD is initially positive, leading to a cancelation of GDD before the focus. As the PFT induced pulse duration increase diminishes, the pulse achieves a duration dominated by the spatial dispersion effect. If these effects can be demonstrated experimentally, they will show that the increase of pulse duration in the focus due to PFT is equivalent to GDD.

In the context of these effects some further observations can be made about figure 4.13. In all but the SF10 prism case, the duration drops below the base value, as determined with the GRENOUILLE. In the SF10 prism case, the pulse duration does not drop below its base level, as determined with interferometric autocorrelation without a focus. It is possible that the dip effect is due to the spatial dispersion effects mentioned above. This

is not certain however, as it is difficult to determine the noise level in the measured durations. In addition, since two different techniques are used here to determine pulse durations, a systematic measurement difference cannot be ruled out.

A small difference between the z position of maximum intensity (the focus) and the z position of maximum pulse duration was observed (see figure 4.13), but is not necessarily significant. Pretzler et al. [PKW00] however predicted that for imperfect lenses the maximum pulse duration increase could be shifted from the focus. This is supported by the Kostenbauder model constructed above, where position of the maximum pulse duration increase can be shifted in some extreme cases.

The noise in the data could be due to the uncertainty inherent in the assigning of pulse durations to interferometric autocorrelations. Also, it is possible that the necessity of adjusting the power as the detector is moved through the focus has contributed to this error. A systematic intensity effect (such as an imperfect quadratic response in the photodiode) would explain the fact that near the focus in all but the SF10 prism case the pulse duration around the focus appears to be reduced below its base level before approaching it again further from the focus. It would be interesting to isolate this effect in future studies.

In the cases where a single SF10 prism was used and where a single BK7 prism was used the pulse duration increase results are unambiguous, though the magnitude of the effects are somewhat uncertain (see figure 4.13). In the case where two opposed BK7 prisms were used, and where no prisms were used, the results are difficult to interpret. There does seem to be a pulse duration increase in these cases, but even a small uncertainty would be enough to dominate this effect. If the data is assumed to represent actual effects, and not to be dominated by uncertainty, it also appears that the "dip like" effect discussed above is present and large compared to the magnitude

of the duration increase at the focus.

In effect, the autocorrelator as presented here gives a good semi-quantitative indicator of the presence of large pulse front tilt. In order to be confident that a pulse duration increase has resulted, a minimum of ~20 fs/mm PFT is required (corresponding to the two BK7 prisms case). This threshold will be influenced by any systematic offset between durations as measured on the GRENOUILLE and the autocorrelator. Values of pulse front tilt larger than ~20 fs/mm can be measured with an accuracy on the order of 20%, by measuring ξ, and solving for PFT in equation 4.15. If the effect causing the pulse duration to dip below the base value near the focus could be isolated, the accuracy could likely be improved.

Other than Pretzler et al. [PKW00], little work has been published on the effects of focussing a pulse with PFT. Horváth et al. [HOB94] model the effect of PFT on pulse duration in the focus. Their formula agrees with Pretzler et al. [PKW00] and Osvay et al. [OKH+04]. Unfortunately, they perform calculations only for very large values of PFT, and their calculations of pulse duration increase seem based on the aperture of the lens rather than on the actual effect of PFT [HOB94]. Osvay et al. [OKH+04] recognize the two important effects contributing to pulse duration increase: PFT (in a focus) and spatial dispersion. Their formulae are the same, but they do not provide sufficient experimental detail to compare their experimental data with the current study.

There is also a comment on [OKH+04] page 215 that underscores the need for more consistent terminology when talking about spatio-temporal distortions, and their effects. Osvay et al. [OKH+04] seem to imply that Pretzler et al. [PKW00] have misinterpreted the cause of pulse duration increase due to PFT. They claim that the duration increase effect "is to be calculated from the bandwidth" [OKH+04]. Immediately preceding their comment, they give an expression for the pulse duration increase in a focus

due to PFT that mirrors the result of Pretzler et al. [PKW00], which they call "stretch". For this reason it can be assumed that they mean the pulse duration increase effect due to their "chirping effect", or to the standard GDD induced by a prism, "is to be calculated from the bandwidth", and not the effect of PFT. What Osvay et al. [OKH+04] seem to be objecting to is the terminology of Pretzler et al. [PKW00], not their result. The terminology presented by Pretzler et al. and the method used to derive their result suggest an effect similar to the Osvay et al. [OKH+04] "chirping effect", though the result is for PFT induced pulse duration increase.

While it does not appear as quantitative as the spectrally resolved knife edge (SRKE), GRENOUILLE or TFPA techniques, the technique of observing the pulse duration increase in a 2-photon autocorrelator is a useful first check of focused pulse behaviour. Our limited understanding of the behaviour of femtosecond pulses in the vicinity of a focus means that this technique is not yet ideally suited to measuring purely spatio-temporal effects. What it does measure is the combined effect of many aberrations on the pulse duration in the focus, which is often just the information desired. This makes it a good compliment to the other more quantitative techniques for measuring pulse duration and spatio-temporal distortions out of the focus.

Focally resolved interferometric autocorrelation does not appear to be a very sensitive technique and it is difficult to resolve the degree of pulse duration increase for small values of PFT, but it is a straightforward modification on a standard autocorrelator, requiring only an additional photodiode and a lens. The interferometric autocorrelator also has the advantage of looking for an actual effect in the focus: distortions having little effect on the autocorrelation traces are unlikely to have an effect on any actual experiment in the focus. Since this technique deals with focused pulses, its sensitivity to pulse energy is very good, despite relying on a 2-photon process. This study used pulses with energies on the order of 10 nJ in the focus, with larger values

away from the focus. The smaller the spot size generated by the focusing lens, the more sensitive the technique will be to pulse energy. To extract a PFT number from the increased pulse duration result, the input spot size w must be known.

The behaviour of femtosecond laser pulses as they are focused is a frontier in our understanding of ultrafast optics. The models discussed here are not yet complete. Non-Gaussian beams, tight foci, and higher order effects are not considered. A more general, electromagnetic approach (perhaps building on the work of Fuchs et al. [FZT05]) is likely needed to deal with these issues in the necessary detail.

More work would also likely improve the performance of this technique. More effort spent aligning the device and characterizing the response of the photodiode may reduce the uncertainty of the measurement. Placing the angularly dispersive element after the interferometer instead of before would also allow the distance between the prism and lens to be varied more easily. This would allow tests of the effects demonstrated in figures 4.19 and 4.20. Additionally, cross correlation could be performed, with one beam containing PFT and one without.

A very interesting extension of this device would be FROG in the focus of very tightly focused pulses. This would likely provide a more detailed view of what is happening to the electric field envelope as it passes through the focus. It would also be interesting to observe the width of the pulse directly by conducting ablation experiments at different distances from a tightly focused, tilted pulse.

4.3 Tilted Front Pulse Autocorrelator

Autocorrelation techniques designed to measure pulse front tilt (PFT) include the "interferometric field autocorrelation" designed by Pretzler and coworkers [PKW00], and the modified Shack-Hartman sensor collinear autocorrelator designed by Grunwald et al. [GNG+03]. Perhaps most promising is the technique developed by Sacks et al. [SMD01] and Raghuramaiah et al. [RSNG03], of tilted pulse-front single-shot autocorrelation (TPFSSAC). This device is outlined in section 3.6.5.

The discussion in this section is based on measurements taken with a commercially built device from Light Conversion, Lithuania, called the tilted front pulse autocorrelator (TFPA). The device can be customized for different wavelengths and pulse durations, but the model used here is specified in the range of 750-1000 nm with a resolution of 200 fs/mm (as measured on a camera, or image plane). The limit on the allowed wavelengths is defined by the nonlinear crystal used, and the limit on the resolution is due to the geometry of the device. A pulse energy of 5 μJ was sufficient to generate a second harmonic signal that could be analyzed with the aid of a digital camera, 50 μJ was sufficient to generate a signal clearly visible to the eye.

When using any single shot autocorrelator, a profile that is proportional to the autocorrelation function is retrieved. In order to extract the true autocorrelation function, a calibration constant must be applied to the delay-axis. Once the autocorrelation function has been determined, to get an idea of the underlying pulse duration, a deconvolution factor must be applied. This is the ratio between the FWHM duration of a pulse of some known functional form, and the FWHM delay of its autocorrelation function. To summarize, the pulse temporal intensity FWHM T_0 is given by

$$T_0 = CK\delta_0 \tag{4.21}$$

where δ_0 is the FWHM of the observed spatial function, K is the deconvolution factor, C is the calibration constant given by

$$C = \frac{\Delta t}{\Delta x} = \frac{2\sin(\chi/2)}{c} \tag{4.22}$$

where χ is the angle between the beams external to the crystal. The calibration constant is determined by measuring the change in the position of the spatial profile as the delay between the pulses is varied. The deconvolution factor for the two most commonly assumed functions are $1/\sqrt{2} \sim 0.707$ for Gaussian and 0.645 for $sech^2$ pulses. It should be noted that in their original paper, Salin et al. [SGRB87] misquoted these constants, though they were corrected in Brun et al. [BGSS91]. These constants are also misquoted in the user manual for the TFPA, so care should be taken when applying a deconvolution factor that the correct one is chosen.

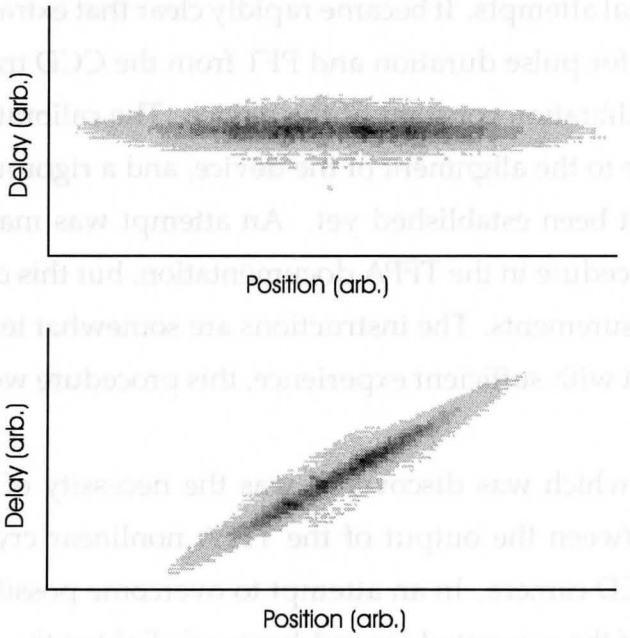

Figure 4.23: An example of raw data captured on a CCD at the output of the TFPA. Top: PFT = 3 fs/mm. Bottom: PTF = 90 fs/mm.

The TFPA device was tested against the GRENOUILLE using various combinations of prisms to induce PFT. After passing through the prisms, the light was directed into the TFPA through two steering mirrors, and the output from the device was recorded with a CCD camera. Pulse front tilt, when present in the beam, was immediately apparent in the retrieved CCD image as a tilt in the pulse signal. Raw data corresponding to direct laser amplifier output and to the same beam beam having traversed a 60° BK7 prism are displayed in figure 4.23. Simply by watching the output of the CCD camera, the dispersion compensation section of the amplifier can be optimized to minimize pulse durations. In addition, the tilting of the pulse image gives a quick qualitative feedback which facilitates minimizing PFT in the beam.

More quantitative measurements have proved quite challenging on this device, in our initial attempts. It became rapidly clear that extracting precise numerical values for pulse duration and PFT from the CCD trace was very sensitive to the calibration constant of the device. The calibration constant is in turn sensitive to the alignment of the device, and a rigorous alignment procedure has not been established yet. An attempt was made to follow the alignment procedure in the TFPA documentation, but this did not result in consistent measurements. The instructions are somewhat terse however, and it is likely that with sufficient experience, this procedure would become more clear.

One problem which was discovered was the necessity of providing a finite distance between the output of the TFPA nonlinear crystal and the position of the CCD camera. In an attempt to overcome possible problems with divergence of the generated second-harmonic light at the output of the device, a lens was inserted between the camera and the nonlinear crystal to image the generated non-collinear light onto the camera 1-to-1 (output optics are not discussed in the documentation).

The TFPA has a total of 6 degrees of freedom that must be properly aligned, as well as any imaging optics that are used at the output. It has 4 degrees of freedom from the input mirrors, one for the nonlinear crystal orientation angle, and one for the delay between the pulse copies. This is in addition to the overlap angle made between the two copies of the beam in the nonlinear crystal, which will determine the spatial resolution of the device.

In an attempt to systematize the process of aligning and calibrating the TFPA, the following alignment and calibration procedure was developed:

1. Align with first input mirror through input aperture.

2. Align with second mirror to superimpose two copies of the beam on nonlinear crystal (observe the beam spots with an IR light viewer).

3. Align with horizontal mirror adjustments on both input mirrors to cause collinear and non-collinear spots to form a straight, vertical line on the CCD.

4. Balance the intensity of the collinear spots by adjusting the angle of the nonlinear crystal.

5. Vary second input mirror vertical adjustment until the non-collinear output intensity is maximized.

6. Insert a 1:1 imaging lens between the nonlinear crystal and the CCD camera.

7. Calibrate the device by scanning the delay, and measuring the shift on the camera. Calculate the calibration constant with a linear regression.

8. Insert a narrow slit near the imaging lens to reject the collinear light (this will reduce the background on the camera).

9. Record image on camera, and reduce the data.

The duration and pulse front tilt of the laser pulse were extracted from the CCD image using a custom-made C++ program. The program worked by taking vertical slices of the CCD image, and fitting Gaussian functions

to each. This resulted in vertical width and maximum intensity position as a function of horizontal position. The slope of maximum intensity in the vertical position as a function of horizontal position was used to calculate PFT using equation 3.23. Pulse duration was computed based on the average Gaussian spatial width. Accurate values for both of these quantities depend on an accurately determined calibration constant.

Configuration	TFPA Duration (fs)	GRENOUILLE Duration (fs)	TFPA PFT (fs/mm)	GRENOUILLE PFT (fs/mm)
no prisms	62	53	2.0	3.3
1 BK7 prism	46	57	90	91
2 BK7 prisms	59	46	10.5	17

Table 4.3: Pulse front tilt (PFT) and pulse duration measured on TFPA and GRENOUILLE for different prism configurations.

Calibration constants were calculated by shifting the delay between the two pulse copies and observing the vertical shift of the CCD image. Calibration constants that led to measurements consistent with other measurement techniques were difficult to achieve. It is possible this is due to an imperfect alignment procedure, or to systematic errors in determining the vertical centre position of the CCD image, especially for highly tilted pulses. When alignment and calibration resulted in measurements that were consistent with measuremnts taken using the GRENOUILLE, they agreed to within $\sim 5\%$. Systematic changes of the CCD image shape as delay is adjusted also can not be ruled out. Table 4.3 summarizes several measurements taken with the TFPA and the GRENOUILLE, for different prism configurations. The error quoted on the TFPA measurement is the uncertainty in the determination of a slope in a linear regression in the case of the PFT value, and the standard deviation of duration measurements in the case of the pulse duration value, each combined with the uncertainty in the calibration con-

stant. In both cases the dominant source of uncertainty was the calibration constant. It is difficult to say what the ideal precision of this technique will be, as a final alignment/calibration procedure has not yet been established.

Even if the TFPA is precisely aligned and accurately calibrated, its measurements of the pulse duration can not be considered accurate, as this method is derived from autocorrelation. The choice of deconvolution factor is arbitrary, and without access to techniques that are sensitive to the intensity distribution (such as SPIDER or FROG), impossible to verify. Its measurement of FT should in principle be fairly robust, however.

4.4 GRENOUILLE

The design of the GRENOUILLE pulse measurement apparatus was described in section 3.7. Because each GRENOUILLE uses a particular geometry, and a particular nonlinear crystal, it will be usable only within a certain range of frequencies, and within a certain range of pulse durations. Thinner crystals have less dispersion, but provide lower spectral resolution. The opposite is true for thicker crystals. This means a compromise must be made, which limits the range of pulse durations for which the device will work [OAKT04]. As a pulse gets shorter in duration, its bandwidth also increases, and vice-versa. Since the GRENOUILLE trace is imaged on a CCD camera, the camera selection will further limit the range of allowed bandwidths and durations. If a pulse has too large a duration or bandwidth, it will be truncated by the edge of the camera in its two axes, respectively. If it has too small a duration or bandwidth, the camera will not be able to resolve the features of the trace with sufficient accuracy. The orientation of the nonlinear crystal can be adjusted, allowing for a range of central wavelengths to be used on the same device. The device used in this work was a Swamp Optics GRENOUILLE 8-20. It is specified to work in the pulse duration range of 18-180 fs, with a maximum bandwidth of 100 nm. It can support central wavelengths between 700-1100 nm. Pulse energies of about 1 μJ at repetition rates of 1 kHz are typically used in order to use the full dynamic range of the CCD camera, but lower pulse energies can be used. An image formed from a pulse of 100 nJ, (the specified sensitivity of the GRENOUILLE) would likely be quite faint, but still visible.

Several problems were encountered initially when attempting to use the GRENOUILLE to make measurement of femtosecond laser pulses. These problems were compounded by lack of access to other techniques that could measure pulses with the detail of the GRENOUILLE. This made it difficult

to verify functioning of the GRENOUILLE. This was part of the motivation behind the other diagnostic techniques in this section.

It turned out there were problems with the GRENOUILLE hardware, the commercial software, and some of the theory underlying the device (the definition of "spatial chirp"). Since the GRENOUILLE is a closed box, with only one adjustment for the input wavelength, it is difficult to determine if the device hardware is working properly. It was determined that mechanical problems (loose and misaligned internal components) meant that the device which was first acquired needed to be returned for servicing.

Closed-box, or "no-tweak" diagnostics can be useful, for when they are properly set up, they tend to remain that way. They do not normally need regular realignment, as devices that require alignment usually do. This significantly reduces the amount of time a device takes to set-up and use. It also provides a measurement that is to a degree independent of the experimenter, if the device is assembled, aligned and calibrated elsewhere. Problems with closed-box solutions arise when something goes wrong, at which point it is often difficult to diagnose (or even become aware of) errors in the measurements the device provides.

Two commercial software packages were purchased for the real-time analysis of GRENOUILLE output: Mesa-Photonics Video-FROG and Femtosoft Quick-FROG. Though not always in precise agreement, once the hardware issues were resolved, these two programs were roughly consistent in the retrieval of electric field amplitude and phase. Several figures throughout this thesis present the output of the GRENOUILLE electric field reconstruction algorithm. Figure 3.19 in section 3.7 depicts the output from the ~50 fs amplifier system, and figure 4.24 depicts the output from the ~120 fs amplifier system, for example. The reconstructed data from a pulse with temporal dispersion is depicted in figure 4.25. Where problems occur is in the characterization of spatio-temporal distortions.

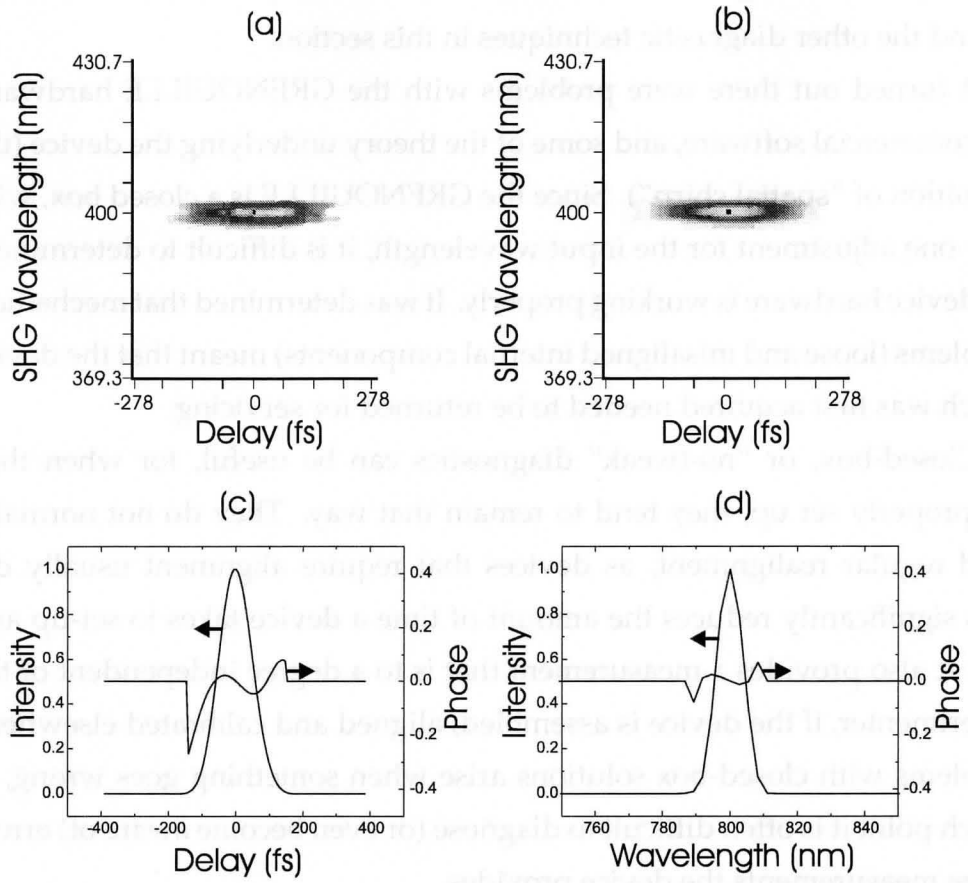

Figure 4.24: An example of GRENOUILLE output 120 fs amplifier. (a) Measured GRENOUILLE trace. (b) Software retrieved GRENOUILLE trace. (c) Software retrieved temporal intensity and phase. (d) Software retrieved spectral intensity and phase. The pulse duration is calculated to be 120 fs, bandwidth 10 nm FWHM.

The PFT values claimed by each of these programs initially were in disagreement by several orders of magnitude, though it was possible to qualitatively estimate PFT by observing a delay shift in the measured GRENOUILLE trace. Through conversations with Dr's Trebino and Akturk [Tre05, Akt05], it was realized that in the case of Quick-FROG, a 10:1 imaging optic internal to the GRENOUILLE had not been accounted for in the software. By

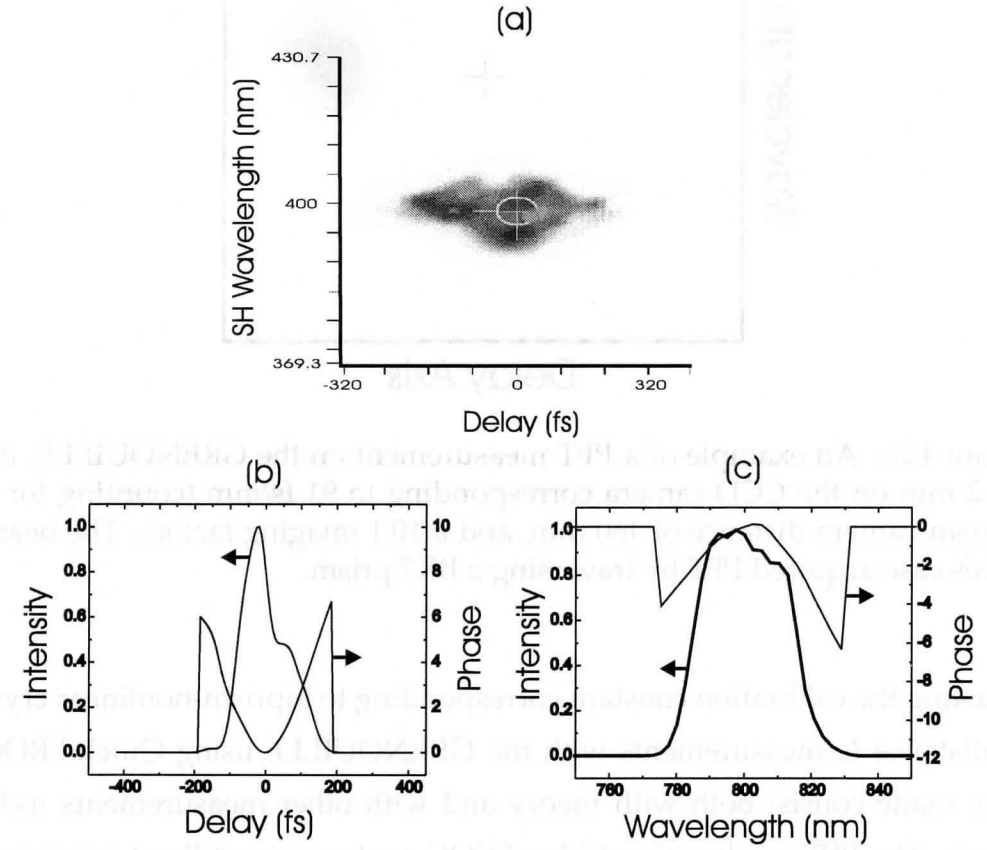

Figure 4.25: An example of a GRENOUILLE trace exhibiting temporal dispersion. (a) Measured GRENOUILLE trace. (b) Software retrieved temporal intensity and phase. (c) Software retrieved spectral intensity and phase. A pulse was increased from 50 fs to 210 fs in glass. Note the large quadratic phase shift.

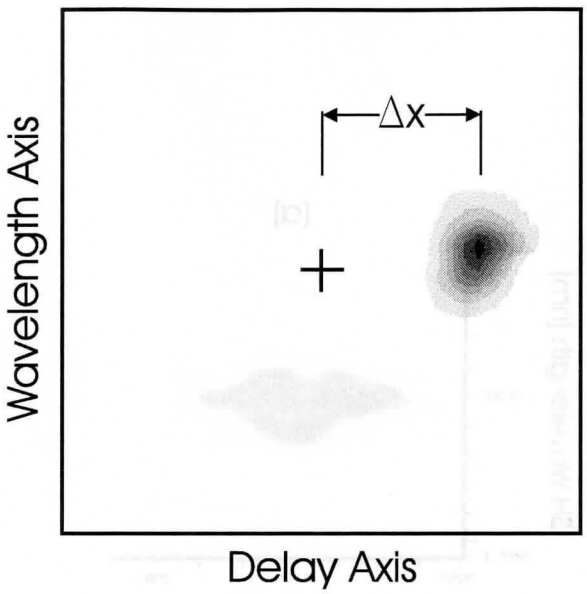

Figure 4.26: An example of a PFT measurement on the GRENOUILLE. Δx = 1.2 mm on the CCD camera corresponding to 91 fs/mm (counting for a biprism-camera distance of 460 mm, and a 10:1 imaging factor). The beam in this case acquired PFT by traversing a BK7 prism.

adjusting the calibration constant corresponding to biprism-nonlinear crystal distance L, measurements with the GRENOUILLE using Quick-FROG were made consist both with theory and with other measurements techniques. The PFT results using Video-FROG are however still not consistent with Quick-FROG, theory, or measurement, even within a constant factor. An example of a GRENOUILLE trace exhibiting PFT can be found in figure 4.26. In addition to using the commercial software, a custom program was written in C++ to measure the quantity of PFT present in a pulse, based on its GRENOUILLE trace. This program simply takes a wavelength integral of the trace, and returns the trace offset from centre Δx. The equation

$$PFT = \frac{\Delta x}{cL} \tag{4.23}$$

where L is the separation between the Fresnel biprism and the nonlinear crystal is used to extract pulse front tilt from the shift on the camera [AKOT03a]. The C++ program does not work in real-time, so it was simply used to verify the results of Quick-FROG, which it does to within a few percent.

The last measurement available using the GRENOUILLE is frequency gradient. A brief review of units may be helpful here. Since we are dealing with ultrafast laser pulses, fs are the appropriate time scale. Unfocused 800 nm beams from table-top Ti:Sapphire CPA lasers will usually have radii that are conveniently measured in mm, so that will be the length scale, to be denoted x. Pulse front tilt can be defined in two ways. One is to define PFT as the angle the peak intensity front makes with respect to the phase front of the pulse γ, which is typically measured in mrad. The other is to define PFT as the delay of the intensity front as a function of a transverse coordinate PFT; this is usually given in fs/mm. These two quantities are related by equation $PFT = \gamma/c$ ($c = 3 \times 10^{-4}$ fs/mm). Spatial dispersion is the rate of change of the transverse position of maximal spectral intensity for a given frequency component with respect to frequency ($\partial x_0/\partial\omega$), given in units of fs·mm. A related quantity used in section 4.1, $\partial x_0/\partial\lambda$, is dimensionless. Analogously, frequency gradient is the rate of change of the frequency of maximum spectral intensity for a given transverse position with respect to lateral position ($\partial\omega_0/\partial x$), given in units of $(\text{fs·mm})^{-1}$. A related quantity used in section 4.1, $\partial\lambda_0/\partial x$, is also dimensionless. As noted above, frequency gradient and spatial dispersion are not simple reciprocals.

This means that frequency gradient is not simply related to angular dispersion, and is thus not as intuitive. Due to confusion about spatio-temporal distortions before the definition of frequency gradient [GAT04, AGZT04], Quick-FROG and Video-FROG both gave the wrong units for the GRENOUILLE measurement of frequency gradient. The units should be $(\text{fs·mm})^{-1}$. If these units are assumed for the numerical value given

by Video-FROG, the measurement is consistent with SRKE (see table 4.4). Quick-FROG has disabled this measurement.

An examples of pulses exhibiting frequency gradient can be found in figure 4.27. A program could be written to further verify the frequency gradient measurement. This program would evaluate the shift in the delay of the maximum GRENOUILLE trace as a function of wavelength, as outlined in [AKOT03b].

Due to the confusion around the measurement of spatial chirp, it is recommended that direct methods like that outlined in section 4.1 be used. In addition, Dr. Trebino supported the position that a SRKE type experiment was the most accurate way to measure spatial dispersion [Tre05]. Frequency gradient measurement with our GRENOUILLE were only explored in a preliminary sense. More work needs to be done to concretely establish the sensitivity and reliability of this measurement.

Prism Setup	SRKE ζ fs·mm	SRKE ν $(\text{fs·mm})^{-1}$	SRKE $\zeta/[\zeta^2 + (\Delta x/\Delta\omega)^2]$ $(\text{fs·mm})^{-1}$	GRENOUILLE ν $(\text{fs·mm})^{-1}$
No Prisms	-1.2	-9.4×10^{-4}	-6.9×10^{-4}	-2.8×10^{-4}
2 SF10	2.0	8.2×10^{-4}	1.1×10^{-3}	1.2×10^{-3}
1 BK7	3.0	1.3×10^{-3}	1.7×10^{-3}	-1.7×10^{-3}
1 SF10	-14	-4.9×10^{-3}	-7.1×10^{-3}	N/A

Table 4.4: Comparison of measurements of ν on the GRENOUILLE and the SRKE. Uncertainty in the relative longitudinal positions of these measurements complicates the direct comparison of their respective measurements of ν. This complication is not expected to have greater than a ~10% effect. The sign of ζ and ν depend on the experimental geometry, which was not the same in each case. A value of 42 fs·mm was used for $\Delta x/\Delta\omega$. The PFT in the SF10 prism case brought the GRENOUILLE trace off-screen, so the ν reading was unreliable.

Problems with measurements taken using the GRENOUILLE are mostly related to data reduction and software. The GRENOUILLE device itself is

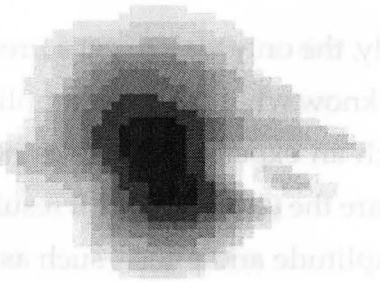

Figure 4.27: An example of a GRENOUILLE trace exhibiting frequency gradient. The trace was taken 65 cm from a BK7 prism. Frequency gradient manifests as a "shear" in the trace, and is calculated to be 6×10^{-4} (fs·mm)$^{-1}$.

very quick and easy to set up and use. Provided the user is familiar with the concepts underlining the device and the phenomena it measures, the interpretation of its results are very straightforward. The GRENOUILLE trace itself is a powerful qualitative diagnostic, allowing optimization of pulse duration, and minimization of spatio-temporal distortions. It works in real time which is an advantage when optimizing optical systems.

Problems with the software will no doubt be resolved as time passes. GRENOUILLE is still a new technique, especially with respect to its sensitivity to spatio-temporal distortions. Both Video-FROG and Quick-FROG have an occasional tendency to converge on a amplitude and phase solution that is quite wrong (off by a factor of or 5 in pulse duration or bandwidth for example), as compared to the measured GRENOUILLE trace they are reducing. Errors in bandwidth can be checked easily with a spectrometer, but errors in duration require other methods, discussed in chapter 3. This problem can usually be corrected by restarting the algorithm or by briefly blocking the laser. For this reason it is important to have a general idea of the beam characteristics expected, perhaps as measured using another technique. When the software converges on the correct solution, it seems to yield sensible results, and both software packages are usually in close

agreement. Unfortunately, the only way to get a precise idea of the accuracy of the measurement is to know what the pulse amplitude and phase actually are, information to which an experimenter does not have access. A good check would be to compare the GRENOUILLE results with another method sensitive to the pulse amplitude and phase, such as SPIDER.

4.5 Diagnostics Conclusion and Discussion

Comparison of different diagnostic techniques are limited to a degree by many factors, most of which can be brought under control with effort. Firstly, the phenomenon being measured (the laser pulse) in principle can get quite complicated, especially in a focus (see for example the work of Fuchs et al. [FZT05]). In addition, there are other factors that can conspire to make diagnostics difficult. Different techniques use different methods to construct an average over a series of pulses in the train, and are thus affected by any non-uniformity between pulses in different ways. Laser properties can fluctuate pulse-to-pulse and over the course of hours or over days as conditions vary and the laser systems are adjusted. In addition, since the temporal and spectral behaviour of ultrafast pulses are sensitive to the optics in their path, care must be taken to ensure near path equivalence if multiple simultaneous beams are to be compared. Difficulty in controlling these factors in the time available limited the extent to which diagnostics presented in this thesis could be compared directly. Truly rigorous head-to-head comparisons would require many parallel beams, with each diagnostic running simultaneously, for beams with a range of bandwidths, durations and temporal, spatial and angular dispersion values. Alternately, experiments comparing two diagnostics at a time, with one acting as a standard can be performed. This was the approach chosen here, but there was not enough time for more than a few initial comparisons.

SRKE measurements have the main advantage of being very accurate, and providing significant detail about the pulse propagation. The number and position of scans can be chosen to suit an application of interest. It is probably the ideal technique for precisely measuring space-frequency couplings. Disadvantages of the technique include the fact that it performs an average over many pulses, so if a pulse train is at all unstable, the results

might be misleading. This method does not measure pulse duration, or any other purely temporal characteristics, so it is best used in parallel with other diagnostics. Focused beams are also problematic for this technique since as beam diameter becomes small, diffraction effects may also become an issue.

When information is required about pulses in the focus, the technique of 2-photon diode autocorrelator, with a resolved focal region becomes useful. It is also the technique most sensitive to small pulse energies considered here. An average power of less than 10 μW (corresponding to pulse energy of 10 nJ in the focus) was used successfully in the focus in section 4.2. Depending upon the lens selection and pulse duration, more or less energy can be used. One must always be careful not to use too much energy when focusing tightly though, to avoid damaging optics and sensors. Long before damage is an issue, the saturation intensity is encountered. Care must be taken to stay well below this intensity, because if the detector saturates during an autocorrelation, there will be systematic problems with the autocorrelation (it will appear too long in duration, for instance). This will usually also mean that the interferometric autocorrelation will no longer have a signal to background ratio of 8:1, so it can be spotted and avoided.

The interferometric autocorrelation technique of section 4.2 has the advantage of being cheap and simple to set up, as it is a simple extension of standard autocorrelation. It has the further advantage of diagnosing the beam in an actual focus, which will be very important to some applications. In particular, high repetition rate, low energy sources (such as femtosecond diode lasers) could benefit from the application of this technique.

The autocorrelation method used does not measure the actual temporal intensity distribution of the pulse, but rather its autocorrelation, so this is not an ideal method for precise pulse duration measurements. This problem could potentially be overcome by spectrally resolving the second harmonic light generated in a nonlinear crystal in the focus, and performing FROG

analysis to reconstruct the pulse amplitude and phase [TDF+97]. This might also make the measurement of the dispersive effect in the focus more precise, leading to better measurement of PFT. As it stands however, the technique is useful, even as a first check of a laser source.

The Light Conversion TFPA is a good qualitative diagnostic for minimizing pulse front tilt and pulse duration, but it has not be found straightforward to use, to date. Its sensitivity is no greater than the Swamp Optics GRENOUILLE (the nonlinear crystal used is thinner and the input beam is not focused) and it provides less information about the pulse. Quantitative analysis has also proved challenging on this device, so it is difficult to say how accurately it can measure pulse duration and PFT. Even given a perfect measurement of the autocorrelation function however, the actual pulse profile is still ambiguous. The TFPA has the advantage of not requiring electronics to use (though a CCD camera is needed for quantitative analysis). Commercially, it is also about half the price of a GRENOUILLE.

The Swamp Optics GRENOUILLE was probably the most all-purpose diagnostic used in this study, once most of the initial technical problems were overcome. As the TFPA, it provides real-time data, but no calibration is required, and the alignment is much simpler. Software also makes it possible to diagnose the pulses in real-time, including amplitude and phase information, as well as spatio-temporal distortion measurements. In most cases, the GRENOUILLE results are taken as the benchmark for measuring the pulse duration, which is often the most relevant pulse characteristic. Over-all the Swamp Optics GRENOUILLE is probably a more cost-effective and versatile device. This is especially true when augmented by techniques such as SRKE for accurate spatial and angular dispersion measurement and autocorrelation (or FROG) in a focus for applications involving focused laser pulses. Very little work has been done on the effects of spatio-temporal distortions on focused pulses. The theoretical work seems to be converging

upon a complete description of the effects of spatio-temporal distortions (see for instance [AKOT03a], [AKOT03b] or [AGZT04]), but this description has not yet been established.

The work in this thesis characterizing the performance of the GRENOUILLE, and especially the TFPA is preliminary in nature. More work is needed to establish concretely the sensitivity of measurements on these devices and their robustness.

It appears that there are at least three sources of pulse duration increase. First there is the "chirping effect" described by Osvay et al. [OKH+04]. This seems to be nothing more than a result of the GDD induced by angular dispersion that is used in pulse stretchers and compressors, either with prisms or gratings. Four prisms are needed to induce GDD without other distortions, but even one will produce GDD.

Akturk et al. [AGZT04] mention the second source of pulse duration increase. The effective duration after a beam has been dispersed spatially is increased with respect to its initial duration, resulting from a reduction of the local bandwidth of the pulse at a specific transverse point. This effect is generally small.

The third source of pulse duration increase is due to PFT in a focus. Pretzler et al. [PKW00], Osvay et al. [OKH+04] and Horváth et al. [HOB94] all seem to agree on the form of this duration increase, as does analysis based on the ray pulse matrices of Kostenbauder [Kos90]. Where the literature is in disagreement is in the interpretation of these effects and in their terminology. Understanding of the pulse duration increases and their terminology is important as there are several independent but closely related effects at work, which are easily confused. This is what has perhaps led to the difficulty in comparisons between several reports, such as those of Horváth et al. [HOB94] and Osvay et al. [OKH+04], which were missing key measurements that made it impossible to compare their results to those of

Pretzler et al. [PKW00] and to the results of this study.

Two of these effects were reported theoretically by Martinez [Mar86] several years before. He treated the effects due to local bandwidth reduction, and the GDD induced by prisms for Gaussian beams. His u factor models the effect of the local pulse duration increase given by Akturk et al. [AGZT04]. When u is set to zero, the GDD formula for prisms of Osvay et al [OKH$^+$04] are recovered. Martinez even modeled pulse front tilt, and how it would evolve, but did not seem to realize it would have an effect beyond the normal GDD effect.

Future studies of the effects of spatio-temporal distortion could prove interesting. For instance, to experimentally test the prediction of Pretzler et al. [PKW00] that the spatial width increase ratio in the focus is equal to the temporal increase ratio, femtosecond pulse ablation could be employed. Previous unpublished work by Dr. Borowiec indicated ellipticity in the focus for beams subject to PFT caused by prisms; more work in this area could prove interesting. By observing the shape of the craters formed by these focused pulses as a function of the distance between the lens and the sample, a physical picture of the behaviour of the pulse in the focus could be formed. The theoretical work of Pretzler et al. [PKW00] with respect to aberrations could also be explored experimentally.

Chapter 5

Femtosecond Laser Pulse Compression

5.1 Introduction

A common method for extra-cavity pulse compression is to subject a Fourier transform limited pulse to a region of temporal phase modulation through some nonlinear effect to increase the spectral content of the pulse, and then adjust the spectral phase of the resulting pulse with some kind of dispersive element. In the past, the necessary phase modulation and dispersion were induced through optical fibers. The drawback to this scheme is that only low energy pulses (on the order of nJ) could be used without damaging the fibers. More recently, hollow multi-mode fibers filled with atomic [NSS96] and molecular [ZK02] gasses have been employed to generate the necessary temporal phase modulation. These have the advantage of a higher "damage" threshold, which can better accommodate commercially available amplifier systems. This is especially true of noble gasses, for which the "damage" is ionization, which is self regenerating.

The phase modulation (due to a time dependent index of refraction) that leads to spectral broadening is often not sufficient alone to produce a shorter pulse. It must be accompanied by dispersion compensation [DR96]. Basic

elements capable of adjusting the dispersion of the pulse to second order include gratings, prisms, and dispersive (or "chirped") mirrors. Gratings produce large amounts of angular dispersion, and hence large amounts of phase shift when used in pairs. Prisms are less dispersive, but also more efficient at transmitting light. Dispersive mirrors are very efficient at reflecting light, but their effect on the phase of the pulse is not adjustable, and they are fabricated for a specific central frequency.

Starting with 140 fs pulses, and using a hollow fused silica waveguide filled with noble gasses for the phase modulation stage, and a pair of quartz prisms for dispersion control Nisoli et al. [NSS96] report obtaining a pulse duration of 18 fs with argon, and 10 fs with krypton. Nisoli et al. later achieved sub 5 fs pulses by combining dispersive mirrors with prisms for dispersion control [NSS+97]. Mohebbi et al. [MF03] reported a compression from 120 fs to 20 fs using a combination of a noble gas-filled-hollow capillary and a dispersive prisms setup. They were able to increase the transmission of the capillary stage from 80% to above 94% by coating the interior with silver. It is also possible to improve compression results by cascading more than one capillary-prism compression system. Thøgersen et al. were able to compress high energy 140 fs pulse to 10 fs with this technique [TBH00].

Sophisticated schemes for compensating the phase of the frequency broadened pulses have also been used. Each of the above methods for correcting second order phase will also have an effect on the third order phase of the pulse. By combining two or more of these basic methods, the phase of the pulse can be corrected to third order [NSS+97]. More precise control can be obtained through the use of adaptive optics, which include spatial light modulators (SLM) and deformable mirrors. When combined with self-referencing diagnostics such as GRENOUILLE or SPIDER, these adaptive optics can be adjusted automatically by creating a computer controlled feedback loop.

Using a feedback system with SLM, Xu et al. [XNM+00] demonstrated programmable dispersion control and generated 6-fs pulses. Using a similar SLM technique, Schenkel et al. [SBK+03] generated the shortest GW peak power pulses to date (3.8 fs).

Other mechanisms can also be used to generate the phase modulation required to compress laser pulses. Much work has been done recently on molecular phase modulation (MPM). The idea is to use coherent vibrational or rotational excitations to create a time varying index of refraction. These vibration or rotation states are induced using a pump laser pulse. A probe laser pulse then acquires a phase modulation. The advantage of this technique is that it allows more control over the phase modulation, as the time separation between the two pulses can be tuned. This technique, though more limited in the maximum power it can support, leads to pulses which are much less difficult to dispersion compensate. Using molecular phase modulation, Spanner et al. [SI03] demonstrated theoretically that 1.2 fs pulses at at 800 nm should be possible, and [ZK02] experimentally compressed 27 fs pulses to 4 fs in a hollow capillary filled with H_2 or SF_6 gasses.

An interesting alternative to the gas filled hollow fiber for inducing phase modulation in pulses with large pulse energies is SPM in bulk materials. With appropriate spatial filtering, Mével et al. [MTSC02] demonstrated that spectral broadening through SPM could be achieved in glass. The glass is placed just before a laser focal spot, where SPM occurs in the bulk. A pinhole placed near the focus of the beam acted as a spatial filter to ensure spatially uniform spectral broadening. They used this method, along with dispersive mirrors and SiO_2 prisms, to compress a 42 fs input pulse at 800 nm to 14 fs with a transmission efficiency of 50%. They argue the advantage of this technique is that it can be scaled up to arbitrary pulse energies.

Recent progress in ultrashort laser pulse diagnostics have made it possible to easily measure the output of extra-cavity pulse compression tech-

niques. To date, few reports include diagnostics more advanced than autocorrelation, such as FROG [TDF+97] or SPIDER [IW98].

The following experiment demonstrates the ability of the GRENOUILLE to characterize pulses that have been undergone SPM in a hollow argon filled capillary, and compressed with a pair of Brewster cut BK7 prisms.

5.2 Experimental Setup

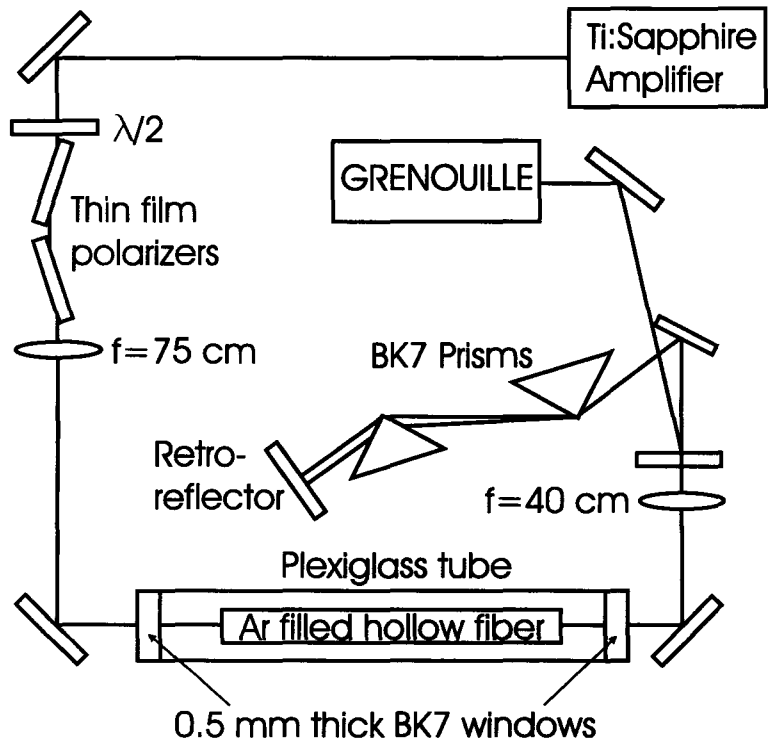

Figure 5.1: The pulse compression setup. All mirrors are either gold, silver, or ultrafast broadband dielectric.

The pulse compression setup is sketched in figure 5.1. It is based on work performed by Thogersen et al. [TBH00], and makes use of their plexiglass capillary housing. All mirrors were either high quality silver from Femto-

lasers, gold from Newport, or ultrafast dielectric from Newport. For control of the pulse energy, the output of the Spectra-Physics Spitfire amplifier system was passed through a Thorlabs zero order $\lambda/2$ waveplate to vary the polarization of the beam. It was then passed through two Newport ultrafast thin film polarizers, which rejected vertically polarized light, attenuating the beam. Its average power was measured using an Ophir photodiode detector. The pulse energy was varied by adjusting the orientation of the waveplate.

The beam is directed through a 75 cm lens, and coupled into the 50 cm long hollow capillary (inner diameter 250 μm), such that the waist of the beam is located at the capillary entrance. This is done at low pulse energy, to avoid damaging the input to the capillary. The capillary is housed in a plexiglass tube, with BK7 windows at the input and output. The housing is mounted on manual micrometer stages, that allow for fine adjustment of the transverse position of the input and output of the capillary. When the transmission through the capillary has been maximized, the pulse energy is increased, and argon gas is pumped into the plexiglass housing. Spectra are measured using a Ocean Optics USB2000 spectrometer.

After propagating through the capillary, the laser beam is re-collimated with a 40 cm lens. It is then directed through two 69° isosceles ultrafast prisms, from Newport. The pulse is then reflected off a retro-reflector, and retraces its path through both prisms.

A mirror is placed in the path of the beam after it has traversed the prisms, and directs it into a GRENOUILLE for measurement. An Ophir beam profiler is used to take profiles of the beam as it travels through the system. Pulse front tilt and spatial dispersion are monitored using the GRENOUILLE, and minimized by adjusting the orientation of the prisms. The distance between the prisms is varied to optimize the dispersion of the pulse, as monitored on the GRENOUILLE.

5.3 Hollow Capillary Section

The optimal coupling of the laser beam between a Gaussian mode in free space and a guided mode in a hollow fiber is achieved when the axis of propagation is collinear with the waveguide axis, and when the laser beam waist is located at the entrance to the fiber. The only remaining parameter that affects the coupling efficiency for a given fiber is the ratio of the beam radius at the waist w_0 with the radius of the waveguide a. The parameter w_0 is to be read here as the $1/e$ radius of the amplitude of the electric field, or as the $1/e^2$ radius of the intensity. If w_0 is too large, not all of the light will make it into the capillary. If w_0 is too small, the divergence angle will be large. Since the transmission of the guided mode depends on grazing angle reflection, large divergence angles will have a negative impact on transmission. Crenn suggests a value of $w_0/a = 0.59$ as optimal [Cre93].

In this study a 50 cm long, 125 μm inner radius fused-silica capillary was used. For optimal coupling, the input beam waist should have $w_0 = 73$ μm. The output of the Spitfire was measured to have an intensity $1/e^2$ radius of $w = 2.8$ mm. Using equation 2.18 with a 750 mm focal length lens, the value of the radius at the focus is calculated to be 68 μm, which is very close to the ideal value of 73 μm. The radius of the beam at the focus was also measured using a scanning knife-edge. Results are plotted in figure 5.2. The intensity $1/e^2$ radius in the focus was measured to be 64 μm.

The capillary used in the experiment was selected from a number of similar capillaries by measuring the transmission efficiency and output mode profiles of each. The capillary used had a good output mode profile and a transmission of 79% at low input power (0.76 mW). When the capillary was placed in the housing the transmission dropped to 51%, but the output mode remained quite good, though slightly elliptical (see figure 5.3). The additional losses are likely due to reflection losses at the windows, which

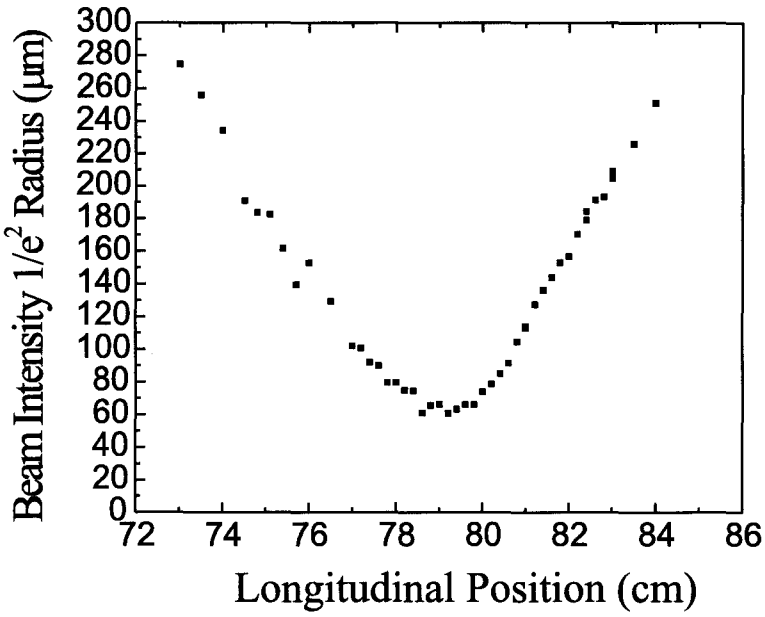

Figure 5.2: The laser beam intensity $1/e^2$ radius for the Spitfire output focused through a 75 cm lens. Initial radius was 2.8 mm. The focal spot was measured to be 64 μm.

were not anti-reflection coated.

Laser power and transmission were varied to achieve a broad output spectrum. Figure 5.4 shows the output spectrum at 35 psi (2.3 bar) argon pressure and 150 mW input laser power. The spectrum achieved is not as symmetric, and not as broad as those reported by [Ole99], [NSS96] or [MF03]. This is possibly due to deviations from Gaussian shape and flat phase of the input pulse spectrum (see figure 5.5), or possibly due to uncompensated third order dispersion in the amplifier. Evidence of uncompensated third-order dispersion can be seen in figure 5.5. This beam is of rather poorer quality than is usually available using the amplifier system (nearly Gaussian shaped output has often been achieved, see figure 3.19 for example). This could have been due to either a misalignment of the laser oscillator or amplifier, or to some uncompensated dispersion effect in the optics used.

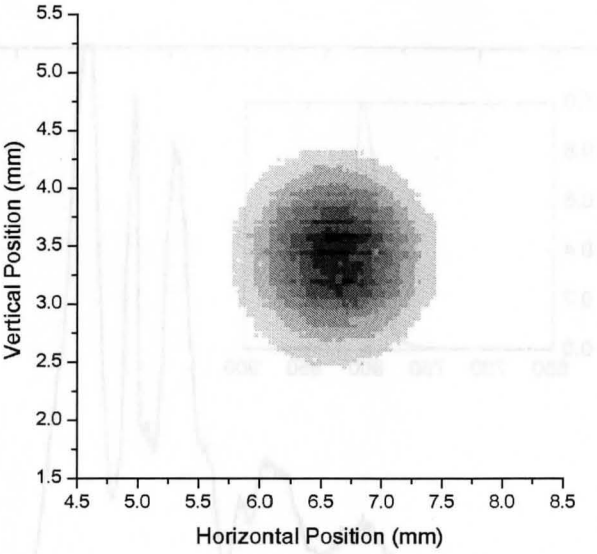

Figure 5.3: The beam profile after the capillary stage.

Since the SPM occurring in the capillary is a nonlinear process, it will tend to exaggerate any structure in the input pulse.

Property	Value	Reference
Ar n	1.002817	[PF64]
Ar $n_2 p^{-1}$	9.8×10^{-24} m^{2}W^{-1} bar^{-1}	[NSS96]
Ar $\beta_2 p^{-1}$	15 fs^{2}m^{-1} bar^{-1}	[NSS96]
Capillary β_2	8.54 fs^{2}m^{-1}	[NSS96]
Capillary α	4 m^{-1}	[NSS96]

Table 5.1: Properties relevant for calculation of capillary characteristic lengths, where p is argon pressure in bar and E is pulse energy in μJ.

Argon gas parameters and the capillary characteristics appear in table 5.1. Derived quantities appear in table 5.2. The actual capillary length of 50 cm is significantly shorter than the ideal length of $\sqrt{L_D L_{NL}} = 1.8$ m (L_D and L_{NL} are the characteristic dispersive and nonlinear lengths, defined in section 2.7). This is due to the unavailability of longer capillaries.

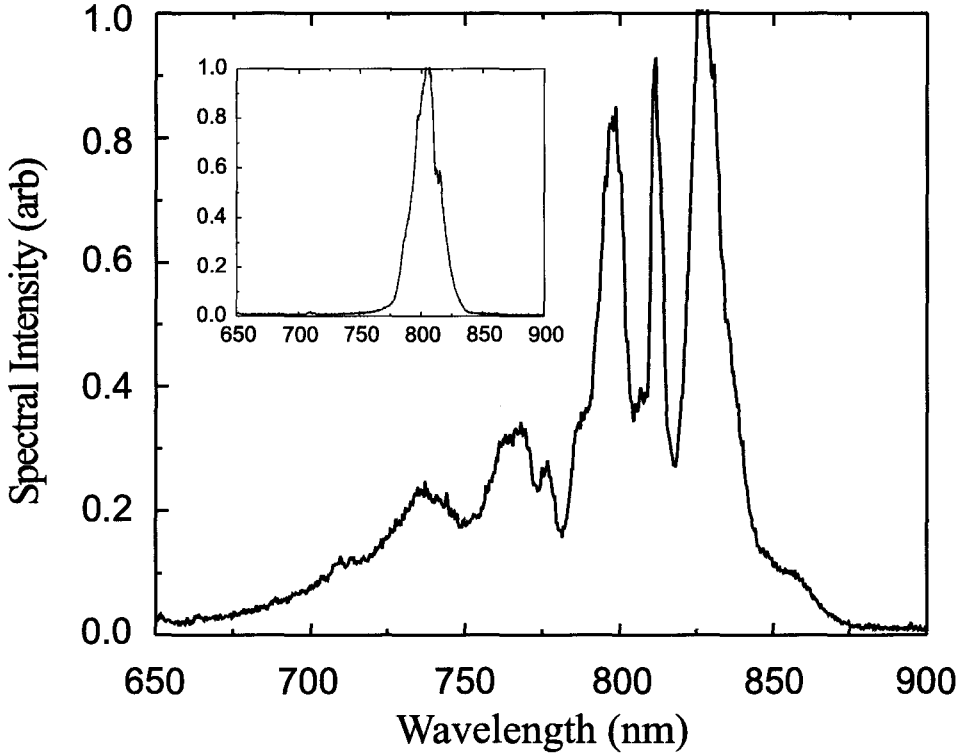

Figure 5.4: Spectral broadening in the capillary due to SPM. The large figure is the pulse spectrum at the exit of the hollow capillary, the inset figure is the pulse spectrum at the entrance of the hollow capillary.

Capillary Characteristic	Value	Value at 150μJ and 2.3 bar
Loss length	$\sim$ 4 (m)	$\sim$ 4 (m)
Dispersive length	1800/(8.5 + 15p) (m)	41.5 (m)
Nonlinear Length	$27.1p^{-1}E^{-1}$ (m)	0.078 (m)
Steepening Factor	0.062	0.062
Raman Factor	$\sim$ 0.02	$\sim$ 0.02

Table 5.2: Capillary characteristic lengths, and nonlinear factors, where p is Argon pressure in bar, and E is pulse energy in μJ.

The experimental power level of 150 mW corresponds to a peak power of 3 GW, which is below the threshold for self-focussing of $\sim 10^{10}$ W given

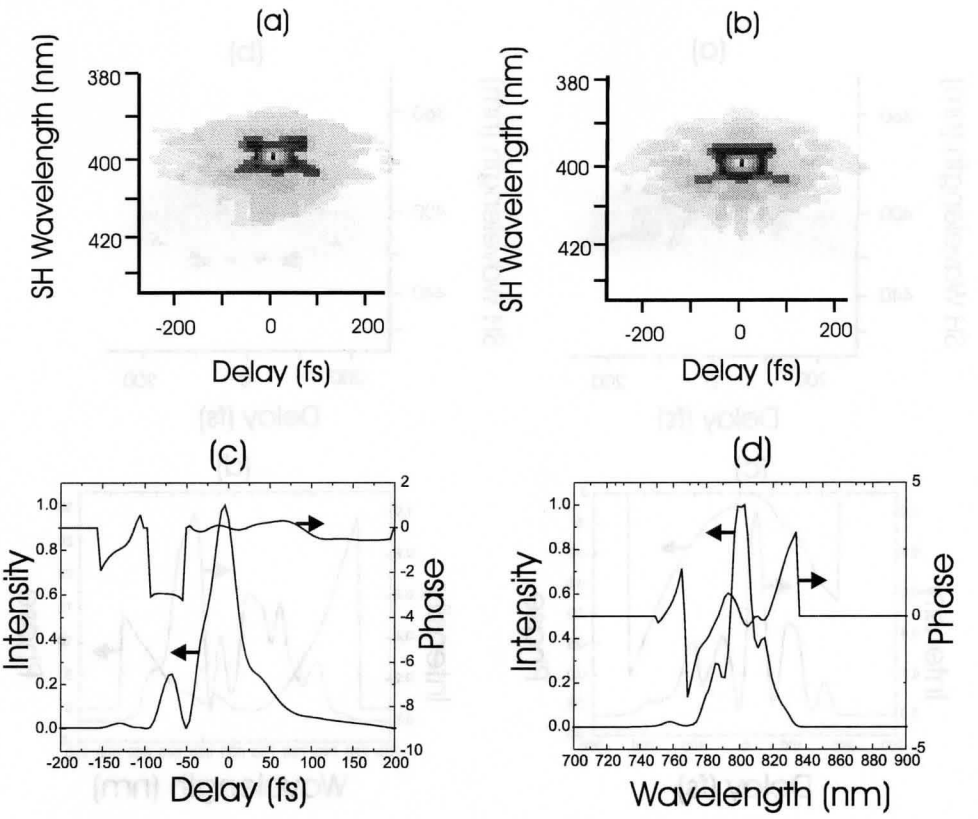

Figure 5.5: GRENOUILLE results for the laser pulse injected into the capillary. (a) Measured GRENOUILLE trace. (b) Software retrieved GRENOUILLE trace. (c) Software retrieved temporal intensity and phase. (d) Software retrieved spectral intensity and phase. Notice the side pulse in the temporal plot, and the phase of the spectral plot. Both of these are symptoms of third order dispersion.

by Luther et al. [LMNW94]. At the capillary input the intensity is 4.1×10^{13} W/cm^2, which is at the effective threshold for multi-photon ionization in Argon, given by $\sim 4 \times 10^{13}$ W/cm^2 [PLC88]. At values so near the effective threshold, the rate of ion production will be quite small. The results obtained using Quick-FROG (from Femtosoft Technologies) for the output of the capillary is depicted in figure 5.6. Note that the bandwidth has increased significantly, but the pulse duration is still quite long, and that

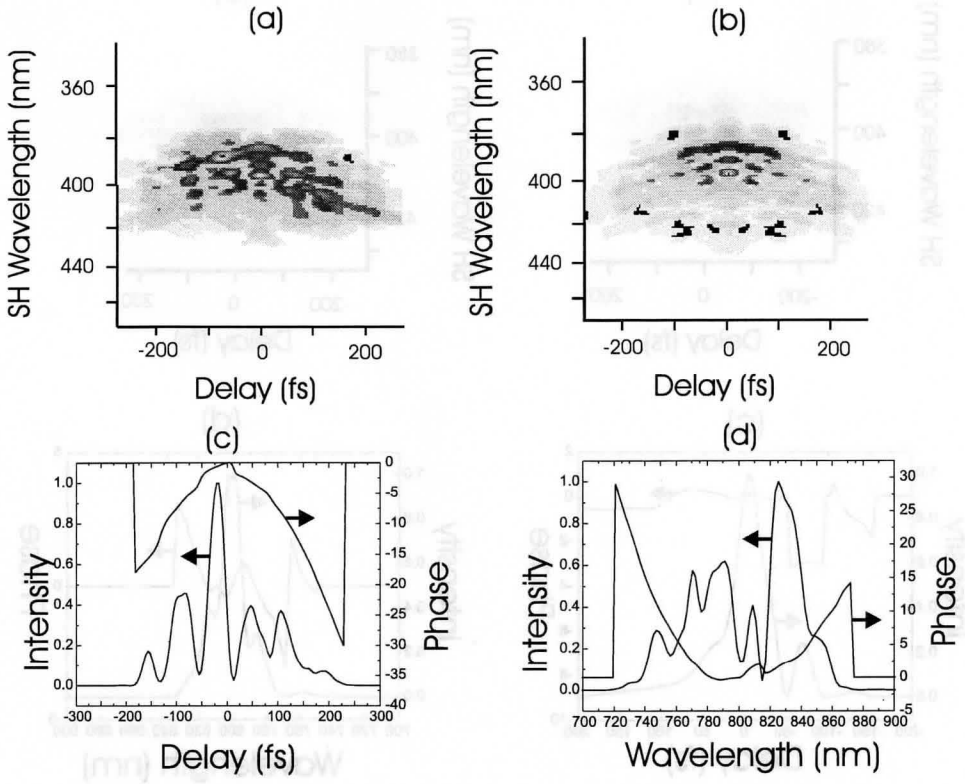

Figure 5.6: GRENOUILLE results for pulse after undergoing SPM in hollow capillary. (a) Measured GRENOUILLE trace. (b) Software retrieved GRENOUILLE trace. (c) Software retrieved temporal intensity and phase. (d) Software retrieved spectral intensity and phase. The bandwidth was measured to be ~80 nm, the duration was measured to be ~120 fs, and the PFT was measured to be 7 fs/mm. Duration and bandwidth FWHM are not well defined, as the structure of the pulse at this stage is complex.

considerable structure has been generated.

A power spectrum generated theoretically using the mathematics defined in section 3.4 can be found in figure 5.7. It assumes that the pulse injected into the capillary had an energy of 150 μJ, was Gaussian shaped temporally, was 50 fs long and Fourier transform limited. The parameters that were used in the capillary model are calculated from tables 5.1 and 5.2. This pulse was propagated through 50 cm. It is not quite as broad as the

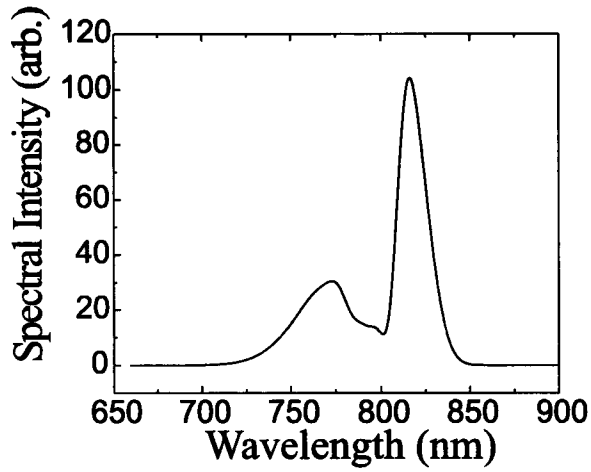

Figure 5.7: A simulated power spectrum after transmission through the capillary, with characteristics given in tables 5.1 and 5.2.

experimentally observed spectrum, and lacks some of the structure, but it is qualitatively similar. The asymmetry of the experimental spectrum for instance is reproduced. This effect can be explained by the self-steepening factor (which led to asymmetrical temporal distributions that were steepened on their leading edge, and asymmetrical spectra), calculated to be 0.62, a moderate amount. The Raman delay factor (related to the response time of the nonlinear medium, which in this case is very small) is taken to be very small, so it has a negligible impact. Raman delay and self steepening are defined in section 2.7. The imperfect match between the experimental and theoretical spectra can be explained in part by the fact that the input pulse is not perfectly Gaussian in frequency, time or space. Since the processes in the capillary are nonlinear, they will be sensitive to any small deviations from Gaussian shape, and the result will be a more structured spectrum, as observed.

Since the simulation is very sensitive to input parameters that are not very accurately known, the simulation depicted in figure 5.7 should be in-

terpreted only qualitatively. Spectra resembling those found in the literature can be also produced, by decreasing or ignoring the self-steepening factor, and by changing the characteristic lengths (such as L_D and $L_N L$), or input beam shape.

This model could in principle be used to help identify the reasons more successful compression was not achieved here and why the pulse spectrum was asymmetric and less broad than spectra reported elsewhere (in [MF03], for example). For this to be the case however, input parameters such as self-steepening factor, initial pulse shape and characteristic capillary lengths would have to be more accurately determined, and deviations from these values more fully explored.

5.4 Prism Pair Section

To compensate the spectral phase shift induced in the capillary section, a pair of Brewster cut (69°) prisms were used, folded into a four prism geometry by a rooftop retro-reflector. Their separation l was varied to correct the phase of the pulses to second order. The negative GDD induced by the prism pair is given by [DR96]

$$GDD = -8l\frac{\lambda_0^3}{2\pi c^2}\left(\frac{dn}{d\lambda}\right)^2 \tag{5.1}$$

This equation lists double the dispersion of Diels and Rudolph equation 2.71 because their equation is given for two prism passes only; equation 5.1 covers four prism passes. This negative GDD must compensate for the GDD of all of the optical components in the system, and the GDD induced by SPM in the capillary. The ideal separation between the prisms to produce the minimum pulse duration was found to be 884 mm. This corresponds to a negative GDD of -2600 fs^2. The GDD of the passive optical elements is on

the order of 700 fs^2 (roughly 15 mm of BK7 glass, with a GDD of 45 fs^2/mm). This includes the lenses, windows, capillary, argon and prisms (4 mm each for the lenses, ~1 mm for each prism pass, 1 mm for the windows). The SPM effect accounts for the remaining GDD.

While performing the experiment, dispersion control in the prism section was found by minimizing the duration of the pulse as measured on the GRENOUILLE. Two independent control parameters allowed this. The separation distance between the apexes of the two prisms adjusted the amount of negative GDD. The magnitude of prism material the beam passed through adjusted the magnitude of positive GDD. This is controlled by translating the prisms in the transverse direction with respect to the beam propagation direction inside the prism. By manipulating these two parameters, coarse control (prism separation) and fine control (amount of glass) over dispersion can be exerted. The amount of glass is a fine control because the prism is mounted on a translation stage with μm accuracy. If increasing the amount of glass the beam propagated through increased the pulse duration, there was already too much positive dispersion and hence the prism separation needed to be increased. Likewise, if the duration of the pulse decreased with increasing material, the prism separation needed to decrease. After a few iterations of this procedure, the optimal path length with minimal glass path was found.

A concern when using prisms as dispersion control for intense laser pulses is unwanted nonlinear effects (see section 2.9.2). The beam at the output of the capillary, after being recollimated, has a 1 mm ($1/e^2$ intensity) radius and a power of 75 mW. Its peak intensity is 6.0×10^{10} W/cm^2. When inserted into the B integral to

$$B = \frac{2\pi}{\lambda} \int n_2 I dz \sim \frac{2\pi}{\lambda} n_2 I L \tag{5.2}$$

with a path length of ~6 mm, and a nonlinear index of 3.2×10^{-16} cm^2/W, the B integral estimate nonlinear phase shift is equal to 1.6. This assumes a pulse duration of 120 fs for the first prism pass, 70 fs for the next two prism passes, and a final duration of 20 fs for the last prism pass, as the pulse is compressed. This nonlinear phase shift in the prisms were probably an issue in this experiment. Since the prisms were optimized to remove second order spectral phase shift to minimize the pulse duration however, the residual effect of the nonlinear phase shift in the prisms was likely small. In the future a larger beam size at the output of the capillary, which can be achieved with a longer focal length lens, can be used to reduce this number. For significantly shorter or more energetic pulses the prisms would either need to be replaced with dispersive mirrors, or the beam size would have to be much greater to avoid unwanted nonlinear effects in the glass.

The nonlinear effects through the capillary windows was considered in section 2.9.3. The B integral in this case was ~0.3, and not a source of concern.

5.5 Results

The total transmitted power at the location of the GRENOUILLE was 53 mW, or a net transmission of 33%. The mode profile was good, though somewhat elliptical (see figure 5.8). The retrieved pulse duration of the saved GRENOUILLE trace was 19 fs, though significant energy remained in the wings. Residual energy in the wings was likely due to the fact that the quality of the laser pulses being produced by the amplifier at the time of the experiment were lower quality than usual (see figure 5.5).

It should be noted that there was very little residual pulse front tilt or spatial dispersion. The output of the Quick-FROG program for the compressed pulses is depicted in figure 5.9. The results for slightly detuned pulses, with too little GDD are shown in figure 5.10. It can be seen that these FROG traces

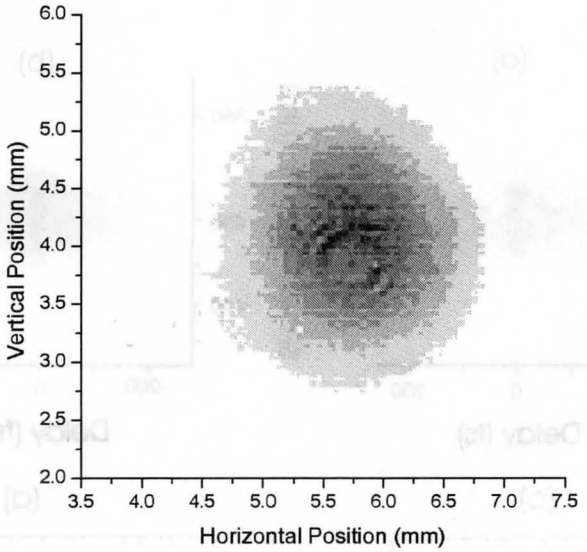

Figure 5.8: The beam profile after compressor stage.

can be formed approximately from figure 5.6 by compressing it in the delay axis, through the application of GDD. As the prism separation is varied, the trace expands or compresses in the delay axis, as expected. When it has reached its minimum duration, it cannot be compressed further.

There are many ways to improve the compression scheme, depending upon what type of pulse is needed. In order to increase the bandwidth of the pulse, a longer capillary can be used. The ideal length for the pulse characteristics for instance was 1.8 m. If a capillary with a larger inner diameter is used, higher energy pulses can be used as the net intensity is decreased (however, the self focussing threshold will still limit maximum power). "Chirped" or dispersive mirrors can be used instead of prisms to increase the throughput of the dispersion control stage, or in addition to prisms to offer higher order dispersion control. Adaptive optics can produce shorter pulses [LFVC02], as well as spatially shaped pulses [ER98]. To achieve the shortest pulses, the capillary-dispersion control scheme can be cascaded, each section producing progressively shorter pulses. All of these

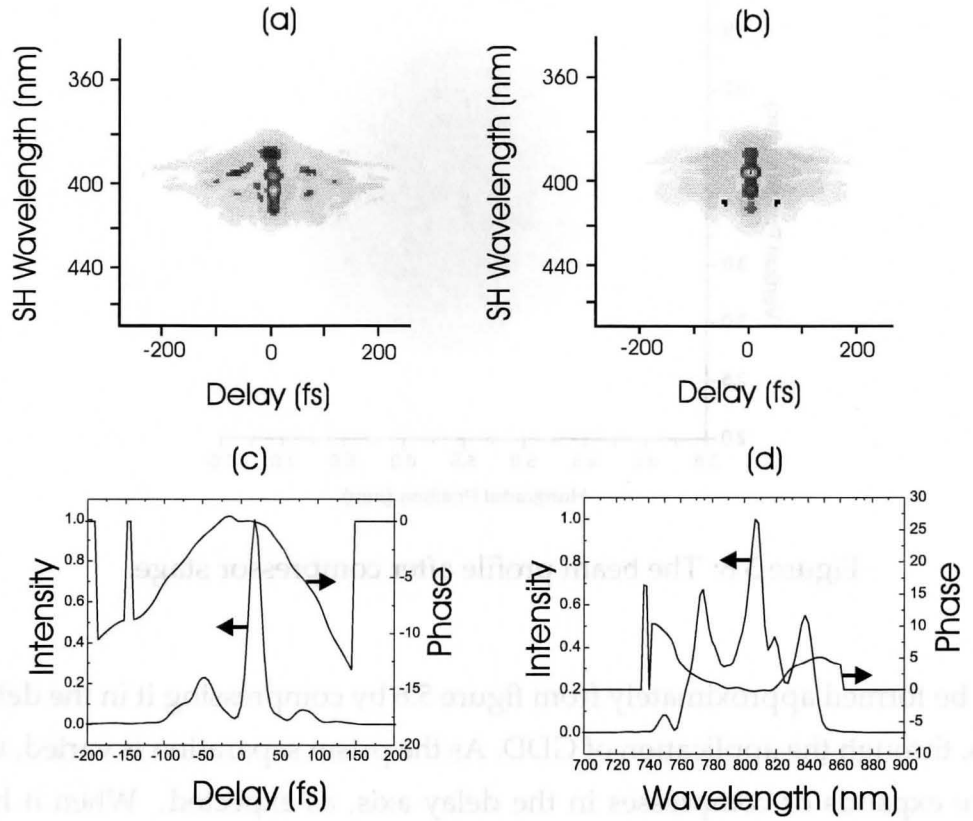

Figure 5.9: GRENOUILLE results for a compressed pulse. (a) Measured GRENOUILLE trace. (b) Software retrieved GRENOUILLE trace. (c) Software retrieved temporal intensity and phase. (d) Software retrieved spectral intensity and phase. The software yields a FWHM duration 19 fs pulse, though there is significant energy in the wings.

techniques have been demonstrated to improve the performance of compression. Ultrafast optical parametric amplification is another promising technique for generating broadband tunable ultrafast laser pulses [SSK98]. A frontier in ultrafast pulse compression is the compression of high power pulses at infrared frequencies, for which dispersion compensation can be challenging, and diagnostics are not as well developed (few semiconductors have appropriate band-gaps above 2 μm, for instance, so even detection

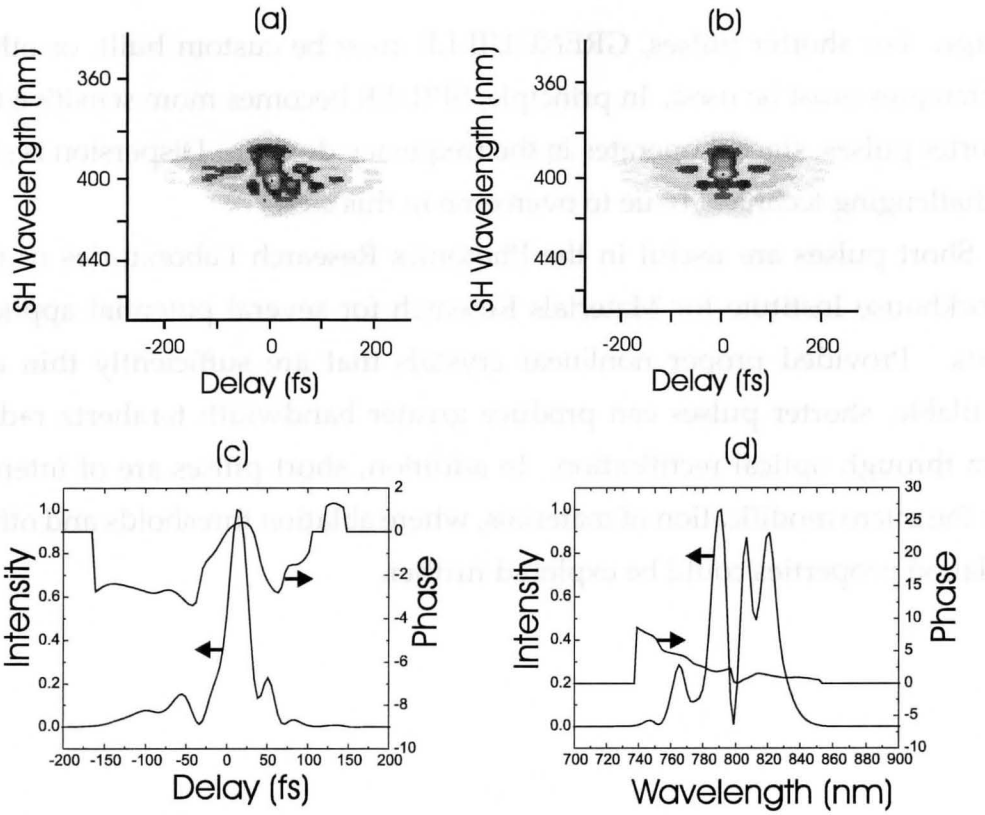

Figure 5.10: GRENOUILLE results for compressed pulse detuned from the optimal setting by decreasing material GDD in prisms. (a) Measured GRENOUILLE trace. (b) Software retrieved GRENOUILLE trace. (c) Software retrieved temporal intensity and phase. (d) Software retrieved spectral intensity and phase.

here is difficult).

To reliably measure and diagnose pulses significantly shorter than 20 fs, the model of GRENOUILLE used in this work would no longer be sufficient. It is specified to be reliable between 20 and 200 fs pulse duration. This limitation is due to the dispersion and thickness of the nonlinear crystal used to generate the second harmonic signal. GRENOUILLE are available commercially through Swamp Optics that are accurate in the 10 to 100 fs

range. For shorter pulses, GRENOUILLE must be custom built, or other techniques must be used. In principle, SPIDER becomes more sensitive for shorter pulses, since it operates in the frequency domain. Dispersion is still a challenging technical issue to overcome in this case.

Short pulses are useful in the Photonics Research Laboratories of the Brockhouse Institute for Materials Research for several potential applications. Provided proper nonlinear crystals that are sufficiently thin are available, shorter pulses can produce greater bandwidth terahertz radiation through optical rectification. In addition, short pulses are of interest for the micro modification of materials, where ablation thresholds and other ablation properties could be explored further.

Chapter 6

Conclusions and Future Work

Over the last two years, much work has been done in furthering our understanding at the Photonics Research Laboratories of spatio-temporal distortions. Two standard diagnostic techniques have been improved and extended in functionality, and a solid basis of understanding of commercially available techniques has been developed. It has been shown that spectrally-resolved knife-edge (SRKE) is a robust and sensitive technique for the measurement of angular dispersion, and spatial dispersion. Since angular dispersion is related to pulse front tilt, this device also provides an indirect measurement of that quantity. The limitation of this device is that it provides no temporal resolution. The interferometric autocorrelation studies, on the other hand, demonstrate a technique that is useful for determining the effect of pulse front tilt and other aberrations on focused laser pulses. In the absence of other distortions, it can in principle be used as a coarse measurement of PFT. With care in optics selection and apparatus design and alignment, as well as careful understanding or avoidance of aberration issues, it is likely that the focus resolved interferometric autocorrelator would be a very useful device for measuring pulse front tilt, and for determining the effective pulse duration in the focus.

Neither of these techniques are sensitive to the amplitude and phase of the laser pulses, as GRENOUILLE is. The data analysis of these techniques

is however more straightforward. The GRENOUILLE provides real time amplitude and phase data, though software complications to date limit confidence in their precise shape. Software problems also lead to incorrect readings of PFT and "spatial chirp" though these problems can be solved. Overall, GRENOUILLE seems to be a robust and versatile technique, though the software commercially available at present leaves much to be desired.

The TFPA can in principle measure the temporal autocorrelation function and the PFT of a pulse, in real time. Some difficulties have been encountered in achieving this in practise, however. Supporting documentation is of rather poor quality, and a rigorous systematic alignment and calibration prescription was not established in the time available. If these problems could be overcome, the TFPA could prove a useful complement to or substitute for the GRENOUILLE, as a standard laboratory diagnostic.

The logical next step to improve the SRKE would be to systematically test the sensitivity and signal to noise response of the device for different laser powers. It would also be helpful to investigate alternatives to the integrating sphere, as this stage in the apparatus leads to much signal loss. A systematic study of the impact of collected data density in the longitudinal and transverse axes on the accuracy with which angular and spatial dispersion can be determined would also prove useful. These studies would all aim to make data acquisition more rapid and efficient.

The interferometric autocorrelator with several traces taken through the focus would be improved by setting the dispersive elements after the interferometer in order to have more control over the prism-lens separation. Other photodiode devices based on different materials could also be tried, as well as experimenting with different focal lengths, and lens types. More work and a greater control over experimental parameters should lead to a better fit with theoretical predictions. It would also be interesting to experimentally isolate the effect of PFT on the spatial broadening of the pulse in

the focus.

Quality diagnostics are one of the cornerstones of sophisticated ultrafast physics experiments. With a solid foundation in this area many experiments in atomic and molecular physics present themselves, as shorter more specialized pulses become available. Field free molecular alignment [RHLF04, RHG+05], molecular reaction path control [CMW05], and temporally resolved molecular dynamics [SSJM03, CBH+05a] have all recently been accomplished. High harmonic generation pushes the limit of short pulse generation by creating pulses hundreds of attoseconds long (1 as = 10^{-18}s) [DK05].

Laser sources are undergoing rapid development as well. Noncolinear optical parametric amplification can generate tunable ultrafast pulses, but requires high quality inputs [KB02]. High intensity near single cycle terahertz pulses have also been recently achieved [RSW+03]; high intensities at this region of the spectrum have been largely unexplored and will likely lead to exciting discoveries.

Bibliography

[Agr89] G. Agrawal, *Nonlinear fiber optics*, Academic Press, Inc., 1989.

[AGZT04] S. Akturk, X. Gu, E. Zeek, and R. Trebino, *Pulse-front tilt caused by spatial and temporal chirp*, Opt. Express **12** (2004), 4399.

[AKOT03a] S. Akturk, M. Kimmel, P. O'Shea, and R. Trebino, *Measuring pulse-front tilt in ultrashort pulses using GRENOUILLE*, Opt. Express **11** (2003), 491.

[AKOT03b] ———, *Measuring spatial chirp in ultrashort pulses using single-shot frequency-resolved-optical-gating*, Opt. Express **11** (2003), 68.

[Akt05] S. Akturk, 2005, private communication.

[Arm67] J. Armstrong, *Measurement of picosecond laser pulse widths*, Appl. Phys. Lett. **10** (1967), 16.

[BGSS91] A. Brun, P. Georges, G. Le Saux, and F. Salin, *Single-shot characterization of ultrashort light pulses*, J. Phys. D **24** (1991), 1225.

[Bor89] Z. Bor, *Distortion of femtosecond laser pulses in lenses*, Opt. Lett. **14** (1989), 119.

[BRS+93] Z. Bor, B. Rácz, G. Szabó, M. Hilbert, and H. Hazim, *Femtosecond pulse front tilt caused by angular dispersion*, Opt. Eng. **32** (1993), 2501.

[BSCK92] T. Brabec, C. Spielmann, P. Curley, and F. Krausz, *Kerr lens mode locking*, Opt. Lett. **17** (1992), 1292.

[CBH+05a] M. Cowan, B. Bruner, N. Huse, J. Dwyer, B. Chugh, E. Nibbering, T. Elsaesser, and R. Miller, *Ultrafast memory loss and energy redistribution in the hydrogen bond networks of liquid H_2O*, Nature **434** (2005), 199.

[CBH05b] T. Crawford, A. Borowiec, and H. Haugen, *Femtosecond laser micromachining of grooves in silicon with 800 nm pulses*, Appl. Phys. A **80** (2005), 1717.

[CMW05] D. Cardoza, M.Baertschy, and T. Weinacht, *Understanding learning control of molecular fragmentation*, Chem. Phys. Lett. **411** (2005), 311.

[Cre93] J. Crenn, *Optical propagation of the HE_{11} mode and Gaussian beams in hollow circular waveguides*, Int. J. Infrared Millimeter Waves **14** (1993), 1947.

[CRSR86] P. Corkum, C. Rolland, and T. Srinivasan-Rao, *Supercontinuum generation in gases*, Phys. Rev. Lett. **57** (1986), 2268.

[DK05] M. Drescher and F. Krausz, *Attosecond physics: facing the wave-particle duality*, J. Phys. B **38** (2005), S727.

[DKW02] C. Dorrer, E. Kosik, and I. Walmsley, *Spatio-temporal characterization of the electric field of ultrashort optical pulses using two-dimensional shearing interferometry*, Appl. Phys. B **74** (2002), S209.

[Dor99] C. Dorrer, *Influence of the calibration of the detector on spectral interferometry*, J. Opt. Soc. Am. B **16** (1999), 1160.

[DQL03] R. Dorn, S. Quabis, and G. Leuchs, *Sharper focus for a radially polarized light beam*, Phys. Rev. Lett. **91** (2003), 233901–1.

[DR96] J. Diels and W. Rudolph, *Ultrashort laser pulse phenomena*, Academic Press, Inc., 1996.

[ER98] A. Efimov and D. Reitze, *Programmable dispersion compensation and pulse shaping in a 26-fs chirped-pulse amplifier*, Opt. Lett. **23** (1998), 1612.

[FBS+96] D. Fittinghoff, J. Bowie, J. Sweetser, R. Jennings, M. Krumbügel, K. DeLong, R. Trebino, and I. Walmsley, *Measurement of the intensity and phase of ultraweak, ultrashort laser pulses*, Opt. Lett. **21** (1996), 884.

[FDTL95] D. Fittinghoff, K. DeLong, R. Trebino, and C. Ladera, *Noise sensitivity in frequency-resolved optical-gating measurements of ultrashort pulses*, J. Opt. Soc. Am. B **12** (1995), 1955.

[FMG84] R. Fork, O. Martinez, and J. Gordon, *Negative dispersion using pairs of prisms*, Opt. Lett. **9** (1984), 150.

[FZT05] U. Fuch, U. Zeitner, and A. Tünnermann, *Ultra-short propagation in complex optical systems*, Opt. Express **13** (2005), 3852.

[GAT04] X. Gu, S. Akturk, and R. Trebino, *Spatial chirp in ultrafast optics*, Opt. Commun. **242** (2004), 599.

[GNG+03] R. Grunwald, U. Neumann, U. Griebner, K. Reimann, G. Steinmeyer, and V. Kebbel, *Ultrashort-pulse wave-front autocorrelation*, Opt. Lett. **28** (2003), 2399.

[GT04] P. Gabolde and R. Trebino, *Self-referenced measurement of the complete electric field of ultrashort pulses*, Opt. Express **12** (2004), 4423.

[Hec90] E. Hecht, *Optics*, Addison-Wesley Publishing Co., 1990.

[HOB94] Z. Horváth, K. Osvay, and Z. Bor, *Dispersed femtosecond pulses in the vicinity of focus*, Opt. Commun. **111** (1994), 478.

[IW98] C. Iaconis and I. Walmsley, *Spectral phase interferometry for direct electric-field reconstruction of ultrashort optical pulses*, Opt. Lett. **23** (1998), 792.

[IW99] ———, *Self-referencing spectral interferometry for measuring ultrafast optical pulses*, J. Quantum Electron. **35** (1999), 501.

[Jac75] J. Jackson, *Classical electrodynamics*, John Wiley & Sons, Inc., 1975.

[JOK+04] S. Juodkazis, H. Okuno, N. Kujime, S. Matsuo, and H. Misawa, *Hole drilling in stainless steel and silicon by femtosecond pulses at low pressure*, Appl. Phys. A **79** (2004), 1555.

[JR99] J. Jasapara and W. Rudolph, *Characterization of sub 10-fs pulse focusing with high-numerical-aperture microscope objectives*, Opt. Lett. **24** (1999), 777.

[JW57] F. Jenkins and H. White, *Fundamentals of optics*, McGraw-Hill Book Company, Inc., 1957.

[KB02] T. Kobayashi and A. Baltuska, *Sub-5 fs pulse generation from a noncollinear optical parametric amplifier*, Meas. Sci. Technol. **13** (2002), 1671.

[KOK+05] A. Kovács, K. Osvay, G. Kurdi, M. Görbe, J. Klebniczki, and Z. Bor, *Dispersion control of a pulse stretcher-compressor system with two-dimensional spectral interferometry*, Appl. Phys. B **80** (2005), 165.

[Kos90] A.G. Kostenbauder, *Ray-pulse matrices: A rational treatment for dispersive optical systems*, J. Quantum Electron. **26** (1990), 1148.

[LCJ95] L. Lepetit, G. Chériaux, and M. Joffre, *Linear techniques of phase measurement by femtosecond spectral interferometry for applications in spectroscopy*, J. Opt. Soc A. B **12** (1995), 2467.

[LFVC02] F. Légaré, J. Fraser, D. Villeneuve, and P. Corkum, *Adaptive compression of intense 250-nm-bandwidth laser pulses*, Appl. Phys. B **74** (2002), S279.

[LLP85] H. Lehmeier, W. Leupacher, and A. Penzkofer, *Nonresonant third order hyperpolarizability of rare gases and N_2 determined by third harmonic generation*, Opt. Commun. **56** (1985), 67.

[LMNW94] G. Luther, J. Moloney, A. Newell, and E. Wright, *Self-focusing threshold in normally dispersive media*, Opt. Lett. **19** (1994), 862.

[Mar86] O. Martinez, *Pulse distortions in tilted pulse schemes for ultrashort pulses*, Opt. Commun. **59** (1986), 229.

[ME88] P. Milonni and J. Eberly, *Lasers*, John Wiley & Sons, Inc., 1988.

[MF03] M. Mohebbi and R. Fedosejevs, *High-efficiency optical compression of Ti:sapphire laser pulses at 800 nm using a silver-coated hollow fiber*, Appl. Phys. B **76** (2003), 345.

[MSB+88] P. Maine, D. Strickland, P. Bado, M. Pessot, and G. G. Mourou, *Generation of ultrahigh peak power pulses by chirped pulse amplification*, J. Quantum Electron. **24** (1988), 398.

[MTSC02] E. Mével, O. Tcherbakoff, F. Salin, and E. Constant, *Extracavity compression technique for high-energy femtosecond pulses*, J. Opt. Soc. Am. B **20** (2002), 105.

[NSS96] M. Nisoli, S. De Silvestri, and O. Svelto, *Generation of high energy 10 fs pulses by a new pulse compression technique*, Appl. Phys. Lett. **68** (1996), 2793.

[NSS+97] M. Nisoli, S. Stagira, S. Silvestri, O. Svelto, S. Sartania, Z. Cheng, M. Lenzner, C. Spielmann, and F. Krausz, *A novel-high energy pulse compression system: generation of multigigawatt sub-5-fs pulses*, Appl. Phys. B **65** (1997), 189.

[OAKT04] P. O'Shea, A. Akturk, M. Kimmel, and R. Trebino, *Practical issues in ultra-short-pulse measurements with 'GRENOUILLE'*, Appl. Phys. B **79** (2004), 683.

[OH93] M. Oberthaler and R. Höpfel, *Spectral narrowing of ultrashort laser pulses by self-phase modulation in optical fibers*, Appl. Phys. Lett. **63** (1993), 1017.

[OKGT01] P. O'Shea, M. Kimmel, X. Gu, and R. Trebino, *Highly simplified device for ultrashort-pulse measurement*, Opt. Lett. **26** (2001), 932.

[OKH+04] K. Osvay, A. Kovács, Z. Heinner, G. Kurdi, J. Klebniczki, and M. Csarári, *Angular dispersion and temporal change of femtosecond pulses from misaligned pulse compressors*, J. Sel. Top. Quantum Electron. **10** (2004), 213.

[OKK+05] K. Osvay, A. Kovács, G. Kurdi, Z. Heiner, M. Divall, J. Klebniczki, and I. Ferincz, *Measurement of non-compensated angular dispersion and the subsequent temporal lengthening of femtosecond pulses in a CPA laser*, Opt. Commun. **248** (2005), 201.

[Ole99] J. Olesen, *Generation of sub 20 femtosecond laser pulses and coulomb explosion studies of D_2*, Master's thesis, University of Aarhus, 1999.

[PF64] E. Peck and D. Fisher, *Dispersion of argon*, J. Opt. Soc. Am. **54** (1964), 1362.

[PFH+04] T. Planchon, S. Ferré, G. Hamoniaux, G. Chériaux, and J. Chambaret, *Experimental evidence of 25-fs laser pulse distortion in singlet beam expanders*, Opt. Lett. **29** (2004), 2300.

[PKW00] G. Pretzler, A. Kasper, and K. Witte, *Angular chirp and tilted pulses in CPA lasers*, Appl. Phys. B **70** (2000), 1.

[PLC88] M. Perry, O. Landen, and E. Campbell, *Multiphoton ionization of the noble gasses by an intense* 10^{14}*-W/cm*^{2} *dye laser*, Phys. Rev. A **37** (1988), 747.

[PTVF02] W. Press, S. Teukolsky, W. Vetterling, and B. Flannery, *Numerical recipes in C++*, Cambridge University Press, 2002.

[RHG+05] M. Renard, E. Hertz, S. Guerin, H. Jauslin, B. Lavorel, and O. Faucher, *Control of field-free molecular alignment by phase-shaped laser pulses*, Phys. Rev. A **72** (2005), 025401–1.

[RHLF04] M. Renard, E. Hertz, B. Lavorel, and O. Faucher, *Controlling ground-state rotational dynamics of molecules by shaped femtosecond laser pulses*, Phys. Rev. A **69** (2004), 043401–1.

[RSNG03] M. Raghuramaiah, A. Sharma, P. Naik, and P. Gupta, *Simultaneous measurement of pulse-front tilt and pulse duration of a femtosecond laser beam*, Opt. Commun. **223** (2003), 163.

[RSW+03] K. Reimann, R. Smith, A. Weiner, T. Elsaesser, and M Woerner, *Direct field-resolved detection of terahertz transients with amplitudes of megavolts per centimeter*, Opt. Lett. **28** (2003), 471.

[SBK+03] B. Schenkel, J. Biegert, U. Keller, C. Vozzi, M. Nisoli, G. Sansone, S. Stagira, S. De Silvestri, and O. Svelto, *Generation of 3.8-fs pulses from adaptive compression of a cascaded hollow fiber supercontinuum*, Opt. Lett. **28** (2003), 1987.

[Sel83] S. Self, *Focusing of spherical Gaussian beams*, Appl. Opt. **22** (1983), 658.

[SGRB87] F. Salin, P. Georges, G. Roger, and A. Brun, *Single-shot measurement of a 52-fs pulse*, Appl. Opt. **26** (1987), 4528.

[SI03] M. Spanner and M. Ivanov, *Optimal generation of single-dispersion precompensated 1-fs pulses by molecular phase modulation*, Opt. Lett. **28** (2003), 576.

[SMD01] Z. Sacks, G. Mourou, and R. Danielius, *Adjusting pulse-front tilt and pulse duration by use of a single-shot autocorrelator*, Opt. Lett. **26** (2001), 462.

[SSJM03] E. Skovsen, H. Staplfeldt, S. Juhl, and K. Mølmer, *Quantum state tomography of dissociating molecules*, Phys. Rev. Lett. **91** (2003), 090406–1.

[SSK98] A. Shirakawa, I. Sakane, and T. Kobayashi, *Pulse-front-matched optical parametric amplification for sub-10-fs pulse generation tunable in the visible and near infrared*, Opt. Lett. **23** (1998), 1292.

[ST91] B. Saleh and M. Teich, *Fundamentals of photonics*, John Wiley & Sons, Inc., 1991.

[Sun98] H. Sun, *Thin lens equation for a real laser beam with weak lens aperture truncation*, Opt. Eng. **37** (1998), 2906.

[TBH00] J. Thøgersen, A. Borowiec, and H. Haugen, *10-fs pulses from two-stage capillary-prism compressor*, Conference on Lasers and Electro-Optics, 2000.

[TDF+97] R. Trebino, K. DeLong, D. Fittinghoff, J. Sweetser, M. Krumbügel, and B. Richman, *Measuring ultrafast laser pulses in the time-frequency domain using frequency-resolved optical gating*, Rev. Sci. Instrum. **68** (1997), 3277.

[Tre00] R. Trebino, *Frequency resolved optical gating*, Kluwer Academic Pulishers, 2000.

[Tre05] Rick Trebino, 2005, private communication.

[VKKO02] K. Varjú, A. Kovács, G. Kurdi, and K. Osvay, *High-precision measurement of angular dispersion in a CPA laser*, Appl. Phys. B **74** (2002), S259.

[VKOK02] K. Varjú, P. Kovács, K. Osvay, and G. Kurdi, *Angular dispersion of femtosecond pulses in a Gaussian beam*, Opt. Lett. **27** (2002), 2034.

[WWD01] I. Walmsley, L. Waxer, and C. Dorrer, *The role of dispersion in ultrafast optics*, Rev. Sci. Instr. **72** (2001), 1.

[WWR04] W. Wasilewski, P. Wasylczyk, and C. Radzewicz, *Femtosecond laser pulses measured with a photodiode - FROG revisited*, Appl. Phys. B **78** (2004), 589.

[XNM+00] L. Xu, N. Nakagawa, R. Morita, H. Shigekawa, and M. Yamashita, *Programmable chirp compensation for 6-fs pulse generation with prism-pair-formed pulse shaper*, J. Quantum Electron. **36** (2000), 893.

[ZK02] N. Zhavoronkov and G. Korn, *Generation of single intense short optical pulses by ultrafast molecular phase modulation*, Phys. Rev. Lett. **88** (2002), 203901–1.

[ZPM+96] J. Zhou, J. Peatross, M. Murnane, H. Kapteyn, and I. Christov, *Enhanced high-harmonic generation using 25 fs laser pulses*, Phys. Rev. Lett. **76** (1996), 752.